UNIVERSITY OF CALIFORNIA SAN DIEGO

Vortex motion and stability with density variation, buoyancy and surface tension

A dissertation submitted in partial satisfaction of the

requirements for the degree

Doctor of Philosophy

in

Engineering Sciences (Applied Mechanics)

by

Ching Chang

Committee in charge:

Professor Stefan G. Llewellyn Smith, Chair
Professor Patrick H. Diamond
Professor Eugene R. Pawlak
Professor David Saintillan
Professor Qiang Zhu

2020

The dissertation of Ching Chang is approved, and it is acceptable in quality and form for publication on microfilm and electronically:

_____

_____

_____

_____

_____

Chair

University of California San Diego

2020

DEDICATION

To my parents,

who give their unconditional support to my education.

EPIGRAPH

A computation is a temptation that should be resisted as long as possible.

— Boyd (2001)

TABLE OF CONTENTS

LIST OF FIGURES

LIST OF TABLES

ACKNOWLEDGEMENTS

This is an incredible journey that could not be accomplished without the help from many people. The one I would like to thank first and foremost is my advisor, Professor Stefan Llewellyn Smith. Without his advice and guidance during these years, I could not finish my PhD research and this dissertation. He has taught me a lot about fluid dynamics and applied mathematics, and I am very honored to have this chance to work with him. What I have learned from him is not just the understanding of the subjects but also a rigorous attitude toward science. I would also like to thank the members of my committee: Professor Diamond, Professor Pawlak, Professor Saintillan, and Professor Zhu, for their insightful discussions and comments on this dissertation work.

I would like to thank all the friends I have met here. I have shared a lot of joy and tears with all these friends. The time I have spent with them is one of the best time in my life. A special thank goes to my wife, Min-Ju, who is always giving me her support and love. I am truly blessed to have she be by my side to face any future challenge.

Finally, I would like to thank my family in Taiwan: my parents and my sister. Without their understanding and sacrifice, I could not be carefree and came here to pursue my degree.

Chapter 2, in full, has been published in the Journal of Fluid Mechanics, "The motion of a buoyant vortex filament" by C. Chang and S. G. Llewellyn Smith, 2018, **857**, R1 (Cambridge University Press). The dissertation author was the primary investigator and author of this material.

Chapter 3, in full, has been published in the Journal of Fluid Mechanics, "Axisymmetric contour dynamics for buoyant vortex rings" by C. Chang and S. G. Llewellyn Smith, 2020, **887**, A28 (Cambridge University Press). The dissertation author was the primary investigator and author of this material.

Chapter 4, in full, has been submitted for publication of the material as it may

appear in the Journal of Fluid Mechanics, "Density and surface tension effects on vortex stability. I Curvature instability" by C. Chang and S. G. Llewellyn Smith, 2020 (Cambridge University Press). The dissertation author was the primary investigator and author of this material.

Chapter 5, in full, has been submitted for publication of the material as it may appear in the Journal of Fluid Mechanics, "Density and surface tension effects on vortex ring stability. II Moore–Saffman–Tsai–Widnall instability" by C. Chang and S. G. Llewellyn Smith, 2020 (Cambridge University Press). The dissertation author was the primary investigator and author of this material.

The research project was funded by the National Science Foundation Award CBET-1706934. The dissertation author was also supported by the Government Scholarship to Study Abroad from the Ministry of Education, Taiwan.

VITA

2020	Doctor of Philosophy in Engineering Sciences (Applied Mechanics), University of California San Diego
2015-2020	Graduate Student Researcher/Teaching Assistant, University of California San Diego
2013-2014	Teaching Assistant, National Taiwan University, Taiwan
2010-2013	Mechanical Engineer, Hon Hai Precision Industry, Taiwan
2010	Master of Science in Fluid Mechanics, Mechanical Engineering, National Taiwan University, Taiwan
2008	Bachelor of Science in Power Mechanical Engineering, National Tsing Hua University, Taiwan

PUBLICATIONS

Llewellyn Smith, S. G., **Chang, C.**, Chu, T., Blyth, M., Hattori, Y. and Salman, H. 2018 Generalized contour dynamics: a review. *Regul. Chaotic Dyn.*, **23**, 507–518.

Chang, C. and Llewellyn Smith, S. G. 2018 The motion of a buoyant vortex filament. *J. Fluid Mech.*, **857**, R1.

Chang, C. and Llewellyn Smith, S. G. 2020 Axisymmetric contour dynamics for buoyant vortex rings. *J. Fluid Mech.*, **887**, A28.

Chang, C. and Llewellyn Smith, S. G. 2020 Density and surface tension effects on vortex stability. I Curvature instability. Submitted to *J. Fluid Mech.*

Chang, C. and Llewellyn Smith, S. G. 2020 Density and surface tension effects on vortex stability. II Moore–Saffman–Tsai–Widnall instability. Submitted to *J. Fluid Mech.*

PRESENTATIONS

Chang, C. and Llewellyn Smith, S. G. Buoyant vortex rings and knots with thin core. American Physical Society, Division of Fluid Dynamics. Portland, November 2016.

Chang, C. and Llewellyn Smith, S. G. Axisymmetric contour dynamics for buoyant vortex rings. American Physical Society, Division of Fluid Dynamics. Denver, November 2017.

Chang, C. and Llewellyn Smith, S. G. Toroidal vortex sheet and buoyant vortex rings. ASME Mechanical Engineering Education Leadership Summit. San Diego, March 2018.

Chang, C. and Llewellyn Smith, S. G. A non-Boussinesq vortex ring. American Physical Society, Division of Fluid Dynamics. Atlanta, November 2018.

Chang, C. and Llewellyn Smith, S. G. Vortex dynamic models with buoyancy. IUTAM symposium on vortex dynamics in science, nature and technology. La Jolla, June 2019.

Chang, C. and Llewellyn Smith, S. G. Stability calculations for vortex rings with unequal densities and surface tension. International Conference on Flow Dynamics. Sendai, November 2019.

FIELDS OF STUDY

Major field: Fluid mechanics

Vortex motion and stability

Professor Stefan G. Llewellyn Smith

Applied mathematics

Professor Stefan G. Llewellyn Smith

ABSTRACT OF THE DISSERTATION

Vortex motion and stability with density variation, buoyancy and surface tension

by

Ching Chang

Doctor of Philosophy in Engineering Sciences (Applied Mechanics)

University of California San Diego, 2020

Professor Stefan G. Llewellyn Smith, Chair

The motion of buoyant vortices is studied using reduced-order models. For a vortex filament, i.e. a curve in three-dimensional space along which vorticity is concentrated as a delta function, the evolution of the filament is calculated using a desingularized Biot–Savart integral. Buoyancy is added using a momentum balance argument while surface tension is also included. A set of equations that couples the transverse motion of the buoyant vortex filament and the axial flow within its core is derived. The new model is verified in an asymptotic limit by comparing it to the previous analytical solution for a thin vortex ring. In another approximation, axisymmetric contour dynamics is implemented

to model a buoyant vortex ring of deforming core. A vortex patch is enclosed by a vortex sheet which emerges from baroclinic generation of vorticity. The evolution of the vortex sheet strength is derived from the Euler equation, and represents the effects of density, buoyancy and surface tension on the axisymmetric vortex ring. Numerical calculations for the integro-differential equations are carried out until the curvature singularity of vortex sheet evolution leads to a blowup. Finally, a linear stability analysis is performed for vortices in the presences of density and surface tension. The basic state solution is given as a perturbation series in a small parameter representing curvature of the vortex or a weak strain acting on it. With the small parameter in the basic state, instabilities are triggered by the resonances between two neutrally stable Kelvin waves for the unperturbed vortex. Those parametric instabilities are the curvature instability and the Moore–Saffman–Tsai–Widnall instability, corresponding to the parameter being curvature or a strain. The effects of density and surface tension on these instabilities are studied by calculating the growth rate and the instability bandwidth in various wavenumber regimes.

Chapter 1

Introduction

By definition, a fluid is any substance that deforms continuously when subjected to a shear force. Typical examples are water, air, gas and anything that flows. Fluids can serve as a medium that transports mass and/or momentum to other objects. Fluids play a very important role in the natural processes in hydrology, physical oceanography, atmospheric dynamics..., and are also essential in the daily life of human civilization including keeping airplanes aloft, keeping HVAC (heating, ventilation, and air condition) systems operating, distributing potable and agricultural water, etc. Fluid mechanics is a branch of mechanics concerned about the statics and dynamics of fluid. Fluid statics is a simpler problem than fluid dynamics since there is no motion and the only unknown is hydrostatic pressure. Unfortunately, fluid dynamics is a much more difficult topic. Given the nature of fluid's continuous deformation and spatially-varying velocity, its motion is usually describe by a "velocity field", $\mathbf{u}(\mathbf{x}, t)$, which is a function of space and time. This Eulerian description is in contrast with the Lagrangian description commonly used in classical mechanics that follows the velocity of a specified particle. To solve for the Eulerian velocity field $\mathbf{u}$, some conservation laws need to be satisfied. The governing equations for the fluid motion, derived from the mass conservation and Newton's second law, are given

by

$$\frac{\partial \rho}{\partial t} + \boldsymbol{\nabla} \cdot (\rho \mathbf{u}) = 0, \tag{1.1}$$

$$\frac{\partial (\rho \mathbf{u})}{\partial t} + \mathbf{u} \cdot \boldsymbol{\nabla}(\rho \mathbf{u}) = -\boldsymbol{\nabla} \left\{ p - \mu \left[\boldsymbol{\nabla} \mathbf{u} + (\boldsymbol{\nabla} \mathbf{u})^T - \frac{2}{3} (\boldsymbol{\nabla} \cdot \mathbf{u}) \right] \right\} + \rho \boldsymbol{g}, \tag{1.2}$$

where the fluid density ρ and pressure p are functions of space and time. $\rho \boldsymbol{g}$ is a body force. μ is dynamic viscosity which is also a function of space and time in general, but is constant for Newtonian fluids. (1.1) is the conservation of mass while (1.2) represents the conservation of momentum. Together they give the compressible, non-Newtonian Navier–Stokes equations. The mathematical challenge to solve the governing equations is rooted in the right-handed side of (1.2) because of the nonlinearity in the convection term of $\mathbf{u} \cdot \boldsymbol{\nabla}(\rho \mathbf{u})$.

Beside the nonlinear term, some simplifications can still be made to the governing equations (1.1) and (1.2) in different regimes. The most common assumption is to make the flow incompressible and the density ρ remains constant. In that case, the mass conservation reduces to zero divergence of the velocity, $\boldsymbol{\nabla} \cdot \mathbf{u} = 0$. On the other hand, the importance of viscosity is usually measured by a dimensionless parameter, the Reynolds number

$$Re = \frac{\rho L U_c}{\mu}, \tag{1.3}$$

which compares the inertia to viscous force, where L and U_c are characteristic length and velocity scales in the flow. For $Re \ll 1$, the flow is extremely viscous, so the inertial terms are negligible and (1.2) reduces to a linear system. For $Re \gg 1$, the flow is approximately inviscid since the effect of viscosity is omitted. The conservation of momentum becomes

$$\frac{\partial \mathbf{u}}{\partial t} + \mathbf{u} \cdot \boldsymbol{\nabla} \mathbf{u} = -\frac{1}{\rho} \boldsymbol{\nabla} p + \boldsymbol{g}, \tag{1.4}$$

for incompressible high-Reynolds-number inviscid flows, or so-called incompressible Euler flows. This kind of flow is the focus of the present dissertation work.

As for most problems in physics, fluid dynamics can be tackled by using laboratory observations, mathematical theories, numerical simulations, or any combination of them. Each approach has its own advantages and disadvantages. For example, laboratory observations require a delicate setup of experiments and a careful data acquisition, as well as a considerable amount of investment on hardware and equipment; mathematical theories and numerical simulations would seem to be more cost efficient alternatives but they are not a direct observation of real world. The nonlinear nature of the momentum equation remains the biggest obstacle to our understanding on the motion of fluid through theoretical or computational approaches. Moreover, fluid flows are complex dynamical systems that can span a range of orders of magnitude, e.g. for studying the mobility of cells or microorganisms, the size is about 10^{-4} to 10^{-5} m while in astrophysics, a fluid system can span $\sim 10^{12}$ m in diameter in the case of accretion disk of black holes or other massive gravitational sources. The most challenging part is when the Reynolds number above a critical value, the nonlinearity dominates and the flow becomes turbulent. A significant feature of turbulent flows is that it consists of multiple scales of eddies. The samllest scale in a turbulent flow is the Kolmogorov length scale η, whose ratio to a characteristic length scale of the flow L is

$$\frac{\eta}{L} \sim \ Re^{-3/4}. \tag{1.5}$$

This means the smallest scale will becomes finer as the Reynolds number increases, and we should resolve the problem from its largest scale to its finest scale. For instance, to understand the aerodynamics of a vehicle traveling at 70 mph on a freeway, the Reynolds number of this flow is at the order of 10^7. So the length scales need to be resolved in this problem will span from a few meters all the way down to micrometers.

With the recent surge of the computing power, computational fluid dynamics (CFD)

has been developed to solve this kind of problems. The most straightforward way to solve it is to brutally resolve all the scales in a computer simulation. A direct numerical simulation (DNS) demands roughly

$$N \sim 160 Re^3 \tag{1.6}$$

grid points to discretize a computational domain of three-dimensional space and time (Pope, 2000, Chapter 9). Using a powerful 1 giga flop (floating-point operation per second) CPU for the vehicle on freeway problem, one needs roughly over a hundred thousand year to complete the run. This is not feasible from an engineering perspective. A method to avoid this not-so-feasible approach is to filter out scales below a predefined threshold. That is large eddy simulations (LES) which can cut down the run time to hours and days, but another mathematical model is required to model the subgrid physics. There are also other methods such as the Reynolds-averaged Navier–Stokes (RANS) equations and a closure problem for the Reynolds stress, e.g. $k - \epsilon$ model, or leveraging the recent developed technologies of parallel computing and GPU (graphics processing unit) acceleration. However, the computational cost and the time consumed are still prohibitive.

In this dissertation work, we will not attempt to directly solve the governing equations for fluid motions using Eulerian numerical schemes with grids. Instead, we will use reduced-order models derived from vortex dynamics to understand the physics of flows. The numerical methods for these vortex models are Lagrangian-based.

1.1 Vortex dynamics

A solid element of square shape will deform into a parallelogram when it is subjected to a shear force. Once the shear is removed, the solid element recovers its initial shape if the applied shear did not exceed the yielding stress. A fluid element has a completely different behavior: it will deform continuously once a stress force is applied even after the

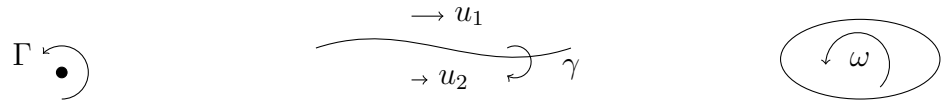

(a) A point vortex (b) A vortex sheet (c) A vortex patch

Figure 1.1: Schematic of zero-, one-, and two-dimensional vortices in two dimensions.

force is removed. The forces applied on a fluid element also may cause linear translation and rotation of the fluid element. The rotational motion of a fluid element is described by vorticity, obtained by taking curl of the velocity,

$$\boldsymbol{\omega} = \boldsymbol{\nabla} \times \mathbf{u}. \tag{1.7}$$

The governing equation for $\boldsymbol{\omega}$ can be obtained by taking the curl of (1.4),

$$\frac{\partial \boldsymbol{\omega}}{\partial t} + \mathbf{u} \cdot \boldsymbol{\nabla} \boldsymbol{\omega} = \boldsymbol{\omega} \cdot \boldsymbol{\nabla} \mathbf{u} + \frac{1}{\rho^2} \boldsymbol{\nabla} \rho \times \boldsymbol{\nabla} p + \boldsymbol{\nabla} \times \boldsymbol{g}, \tag{1.8}$$

where the rate of change in vorticity is determined by convection, stretching and by baroclinic generation.

In many flows, vorticity is an important quantity to understand the fluid motion and dynamics. Especially in high-Reynolds-number flows, vorticity is organized into some coherent structures while the rest of the flow remains nearly irrotational. These coherent vortices are the backbone of fluid motions. We can study the flow using reduced models to calculate the evolution of those compact vortices in two- or three-dimensional domains. As the examples shown in figure 1.1 in two-dimensional flows, vorticity can live on a point, a curve, or in a confined region to model a particular vortex. In three-dimensional flow domains, there are also examples like vortex filaments, vortex sheets, axisymmetric vortex rings... etc. For high-Reynolds-number flows with an interface or solid surfaces, these vortices emerge from those surfaces and usually dominate the motion and the dynamics

of the flow. The flow field, a solenoidal vector field $\mathbf{u}(\mathbf{x}, t)$, can be obtained by inverting (1.7) using the vector potential defined by $\mathbf{u} = \boldsymbol{\nabla} \times \boldsymbol{A}$ and

$$\boldsymbol{\nabla} \times (\boldsymbol{\nabla} \times \boldsymbol{A}) = \boldsymbol{\omega}. \tag{1.9}$$

The velocity is given by

$$\mathbf{u}(\mathbf{x}, t) = \int_V \boldsymbol{\omega}(\mathbf{x}', t) \times \mathbf{K}(\mathbf{x}, \mathbf{x}') \mathrm{d}\mathbf{x}', \tag{1.10}$$

where the integral kernel $\mathbf{K}(\mathbf{x}, \mathbf{x}')$ is a Green function for the linear operator on $\boldsymbol{A}$ in the particular geometry of the domain. V is a compact region occupied by vortices where vorticity is nonzero. (1.10) is the Biot–Savart law for fluid motion and the velocity field is analog to the magnetic field induced by current in electromagnetism. We integrate over the points $\mathbf{x}' \in V$ to calculate the velocity at any point $\mathbf{x}$ in space at a given instant t.

Taking a point vortex or a vortex filament for examples, the vorticity is a delta function in two- or three-dimensional space. To evolve these compact vortices, the self induced velocity can be computed by taking $\mathbf{x} \to \mathbf{x}'$. However, the Green function $\mathbf{K}(\mathbf{x}, \mathbf{x}')$ is the system's response to a delta function and it is singular when $\mathbf{x} \to \mathbf{x}'$. There are several mathematical techniques to desingularize the integral in (1.10). A straightforward way is to cut off the neighborhood of singularity while evaluating the integral. Alternatively one can add a small constant to the denominator in $\mathbf{K}(\mathbf{x}, \mathbf{x}')$ to avoid a division by zero. The two methods are equivalent and a proper physical argument is required to determined the size of cutoff or the small constant in the denominator. We will discuss the detailed treatment for particular vortices in the respective chapters.

The history of vortex dynamics can be dated back a little more than 150 years ago to the seminal paper by Hermann Ludwig Ferdinand von Helmholtz (see von Helmholtz, 1858). The original publication was in German and was translated to English in Tait

(1867). It inspired Sir William Thomson (Lord Kelvin) to conduct a series of study on vortex (Thomson, 1867*b*, 1869, 1875). Although his attempt on the theory (Thomson, 1867*a*) of the fundamental composition of matter in vortex elements did not bear fruit, his work still laid the foundation for the study of vortex dynamics and helps our understanding of fluid motion and dynamics. For example, the Kelvin's circulation theorem states that the circulation around any closed curve $\mathcal{C}$ is conserved in an inviscid, incompressible, barotropic flow.

The development of vortex dynamics has since became an active branch of fluid dynamics and applied mathematics. Before the recent growth of computer power and the emergence of computational fluid dynamics in the past few decades, vortex dynamics was an essential tool for analyzing flow dynamics along with laboratory observations. For example, in the 1960–70s aerodynamicists used helical vortex filaments to model wing-tip vortices and study their motion and stability. Nowadays vortex dynamics is still an important tool to understand the flow physics because it is rooted in the backbone of fluid dynamics: vorticity. Furthermore, vortex-based numerical methods (see Winckelmans, 2004, and the references therein) have the advantages of mesh-free and light to mild demands in computational resources, which make them still relevant to some valuable applications.

1.2 Density, buoyancy and surface tension

A classic and comprehensive text that summarizes the development of vortex dynamics can be found in Saffman (1992). However, in the discussions therein and in the most literature of vortex dynamics, density is usually taken to be uniform throughout the flow. However, the effect of density variation could be important in some applications especially when gravity is also present. The formation of a vortex ring from a thermal

plume is a typical example where the plume itself consists of lighter fluid than that of its ambient. The resulting buoyant vortex ring is very observable as a smoke ring: an exotic example is the smoke rings from volcano (Velasco Fuentes, 2014). The rising motion is not only due to its self-induction but also because of the addition of buoyancy which is the result of coupling density difference and gravity. Gravity is present in the momentum equation in (1.4) as a conservative body force. A common simplification for buoyant flows is the Boussinesq approximation where the effect of density difference is only considered important when it appears with gravity in the momentum equation

$$\frac{\partial \mathbf{u}}{\partial t} + \mathbf{u} \cdot \boldsymbol{\nabla} \mathbf{u} = -\frac{1}{\rho} \boldsymbol{\nabla} p + \boldsymbol{g}'. \tag{1.11}$$

Here $\boldsymbol{g}' = \boldsymbol{g}(\rho_1 - \rho_2)/\rho$ is the reduced gravity (or buoyancy) and ρ_1, ρ_2 are densities for the ambient and the plume. In that case, the vorticity equation becomes

$$\frac{\partial \boldsymbol{\omega}}{\partial t} + \mathbf{u} \cdot \boldsymbol{\nabla} \boldsymbol{\omega} = \boldsymbol{\omega} \cdot \boldsymbol{\nabla} \mathbf{u} + \boldsymbol{\nabla} \times \boldsymbol{g}'. \tag{1.12}$$

The Boussinesq approximation implies that the density difference is very small, i.e. $(\rho_1 - \rho_2)/\rho_1 \ll 1$, while the reduced gravity is of $O(1)$. The flow with a large density difference such as a vortex bubble ring blew by dolphin (Marten *et al.*, 1996) is considered non-Boussinesq.

For a non-Boussinesq flow, although the density might have a continuous variation in the flow, we allow a density jump in reduced models since the vorticity has already been discontinuous. We write (1.4) in two separate equations with two distinct constant densities for a buoyant vortex ring and the ambient air respectively. The flow is solved for the two regions of different densities while the kinematic and dynamic boundary conditions are satisfied on the interface that separates the two densities. The appropriate conditions are that the interface is material and the pressure is continuous. From the perspective of

vortex dynamics, vorticity is created from the baroclinic term in (1.8) as the gradient of density and gravity (represented by the gradient of hydrostatic pressure) do not parallel with each other. Vorticity emerging on the interface makes it become a vortex sheet.

There are several works that use vortex dynamic formulations, particularly vortex sheet, to model the interfacial dynamics between two fluids. That includes free-surface flow problems such as those investigated by Baker *et al.* (1982); Baker & Xie (2011); Shin *et al.* (2018). Vortex sheets are also an appropriate tool to study Rayleigh–Taylor instability (see Pullin, 1982; Tryggvason, 1988; Baker *et al.*, 1993). In terms of numerical computations, one of the great advantage of vortex dynamics over CFD simulations is its Lagrangian nature which makes it having no difficulty to track a material interface. Surface tension can also be included if two fluids are in different phase. This is described by the Young–Laplace equation

$$p_2 - p_1 = T_s \boldsymbol{\nabla} \cdot \boldsymbol{n}, \tag{1.13}$$

where $p_2 - p_1$ is the pressure jump across the interface and $\boldsymbol{n}$ is the normal vector of the interface. T_s is surface tension with a unit of force per length. A vortex sheet model with surface tension has been investigated in Pullin (1982); Hou *et al.* (1994); Baker & Nachbin (1998); Shin *et al.* (2014).

In classical vortex dynamics, the flow is assumed dominated by inertial force in the form of vortices. There are circumstances in which vorticity is balanced by or competes with other physical effects, such as the smoke ring rising up from volcano or the dolphin bubble rings. There are some dimensionless parameters measuring the importance of various physics that we should introduce here. For the density variation, we define the dimensionless Atwood number

$$A = \frac{\rho_2 - \rho_1}{\rho_2 + \rho_1}, \tag{1.14}$$

where $A = 0$ recovers the classical vortex dynamics model. Gravity can be compared to inertia by the Froude number

$$Fr = \frac{U_c}{\sqrt{gL}}. \tag{1.15}$$

The characteristic speed U_c is related to the circulation of vortex by $U_c = \Gamma/L$. The relative importance of buoyancy to inertia is then weighted by

$$\frac{A}{Fr^2} = \frac{(\rho_2 - \rho_1)gL}{(\rho_2 + \rho_1)U_c^2}. \tag{1.16}$$

Lastly, inertial force is compared to surface tension using the Weber number

$$We = \frac{\bar{\rho}U_c^2 L}{T_s}, \tag{1.17}$$

where $\bar{\rho} = (\rho_2 + \rho_1)/2$.

A buoyant vortex filament of circular shape, i.e. a thin vortex ring, has been studied by Turner (1957) and Pedley (1968). However, a formulation for the motion of buoyant filaments of general shape has not been obtained in literature. On the other hand, a vortex ring whose core is not thin has been studied in axisymmetry using contour dynamics (Shariff *et al.*, 1989; Riley, 1998), but its unsteady buoyant version has not been investigated yet.

1.3 Outline of the dissertation

This dissertation work is an attempt to add the effects of density, buoyancy and surface tension into the classical vortex dynamic formulations. It is organized as follows:

Chapter 2 derives the equation of motion for a buoyant vortex filament. Buoyancy is added by using the force balance introduced by Moore & Saffman (1972) using an asymptotic analysis. The vortex core is assumed remaining circular and small compared to

the curvature of the filament, and the Biot–Savart integral is desingularized by subtracting the integral over a local osculating circle. A correction to the self-induced velocity using local induction approximation is then added. A set of coupled equations which gives the motion of a buoyant vortex filament in its transverse and tangential directions is derived, and is validated by an asymptotic solution for a buoyant vortex ring with small inclination.

In Chapter 3, the evolution of an axisymmetric buoyant vortex ring with a deforming core is calculated. This is a problem of vortex patch evolution in axisymmetry. We implement contour dynamics with a correction to the velocity of vortex boundary from the contribution of a vortex sheet. For a buoyant vortex ring, vorticity is generated on its core boundary by the baroclinic torque and the boundary becomes a vortex sheet. An evolution equation for the vortex sheet strength is also derived using the Euler equations. The coupled integro-differential equations are then solved numerically up to a time where a singularity of curvature emerges and the numeric blows up.

In Chapter 4, the parametric instability of a vortex ring is calculated using linear stability analysis including density and surface tension. Infinitesimal disturbances to a straight vortex tube has been found to be neutrally stable. These disturbances are Kelvin waves. When an additional parameter representing a small curvature effect is introduced to the basic state solution, it can feed resonances to two Kelvin waves with azimuthal wavenumber separated by 1. The instability caused by the resonances is named curvature instability. We examine the effect of density and surface tension to the curvature instability when the vortex has a density that differs from that of the flow outside.

Chapter 5 follows the previous chapter, another parametric instability is examined with the effects of density and surface tension. A straight vortex tube subjected to a weak strain field triggers the Moore–Saffman–Tsai–Widnall (MSTW) instability. It arises from the resonances between Kelvin waves with azimuthal wavenuber differed by 2.

In Chapter 6, we conclude the findings in this dissertation work. The results and

their possible applications are discussed, while connections to future work are also outlined.

Chapter 2

Buoyant vortex filaments

This chapter investigate the motion of a thin vortex filament in the presence of buoyancy. The asymptotic model of Moore & Saffman (1972) is extended to take account of buoyancy forces in the force balance on a vortex element. The motion of a buoyant vortex is given by the transverse component of force balance, while the tangential component governs the dynamics of the structure in the core. We show that the local acceleration of axial flow is generated by the external pressure gradient due to gravity. The equations are then solved for vortex rings. An analytic solution for a buoyant vortex ring at a small initial inclination is obtained and it asymptotically agrees with literature.

2.1 Introduction

Vortex dynamics forms an essential part of our understanding of fluid flows, especially for the most elusive flow phenomenon of turbulence (see Pullin & Saffman, 1998). When vorticity is concentrated on a curve in space, the calculation of its self-induced motion is a challenging task. This is due to the singular nature of the Biot–Savart integral. A first approximation comes from the local induction approximation (LIA). For higher-order calculations, a cut-off method (see Saffman, 1992, chapter 11) removes the neighborhood of

the singularity when evaluating the integral. Rosenhead (1930) and Moore (1972) proposed adding a parameter to the denominator to desingularise the Biot-Savart kernel. Their method is equivalent to using a cutoff. Schwarz (1985) used a hybrid model combining a cut-off and the local induction approximation to calculate the motion of vortex filaments in superfluids. Callegari & Ting (1978) investigated vortex filaments with viscous cores and axial velocity using matched asymptotic expansions. More recently, Leonard (2010) calculated the motion of a thin vortex tube with an arbitrary core structure.

Vortex rings have also been intriguing entities in fluid flows, dating back to the pioneering work of Thomson (1867*b*). The theoretical speed of propagation for a thin ring with a hollow core was calculated by Hicks (1884). A good review of vortex rings can be found in Shariff *et al.* (1989). Vortex rings have been observed in geophysics and environmental fluid flows, e.g. bubble rings created by dolphins (see Marten *et al.*, 1996) or a smoke ring from a fireball. The first investigation to take account of buoyancy for a vortex ring was the theoretical work and experiments of Turner (1957). Pedley (1968) performed a theoretical calculation for the motion of bubble rings with and without viscosity. Lundgren & Mansour (1991) computed the motion of bubble rings using a boundary integral method. The development of modern computational methods has led to the investigation of buoyant vortex rings, such as the 3D simulations of Cheng *et al.* (2013). In these studies, buoyant rings are allowed to evolve with their axis initially parallel to gravity, i.e. they start horizontally.

However, the motion of a general vortex filament in combination with buoyancy does not seem to have attracted theoretical interest previously. In this chapter, we derive a mathematical model for the motion of a buoyant thin-core vortex filament. Buoyancy is incorporated by using a force balance on a vortex element. Equations of motion for a buoyant vortex filament of general shape are derived in the following section. Then the effect of buoyancy on the flow structure inside the core is discussed in § 2.3. In § 2.4, we

use our model to investigate a special geometry, a buoyant vortex ring. An analytical solution for an initially non-horizontal ring with small inclination is obtained analytically. Its asymptotic form is compared with the solutions from the literature. In the final section, we draw conclusions and discuss possible future studies.

2.2 Mathematical formulation

We use a force balance on a vortex filament to model its motion. The force balance argument is derived in Moore & Saffman (1972) (referred to as MS72 hereafter) for a constant density Euler flow. Here we consider different densities, ρ_2 and ρ_1, for the vortex filament itself and for the surrounding fluid respectively. Gravity is also included while it is omitted in MS72. The derivation in MS72 is an asymptotic analysis based on three approximations which we also follow: thin vortex core, $a\kappa \ll 1$, where a is the radius of the core and κ the curvature; slow time, $\partial/\partial t \approx \Gamma\kappa^2 \ln(1/a\kappa)$, where Γ is the circulation; and uniform core size, $\partial a/\partial s = O(a^2\kappa^2)$, where s is arclength.

2.2.1 Momentum balance

We use a force balance on a vortex filament to model its motion. The force balance argument is derived in Moore & Saffman (1972) (referred to as MS72 hereafter) for a constant density Euler flow. Here we consider different densities, ρ_2 and ρ_1, for the vortex filament itself and for the surrounding fluid respectively. Gravity is also included while it is omitted in MS72. The derivation in MS72 is an asymptotic analysis based on three approximations which we also follow: thin vortex core, $a\kappa \ll 1$, where a is the radius of the core and κ the curvature; slow time, $\partial/\partial t \approx \Gamma\kappa^2 \ln(1/a\kappa)$, where Γ is the circulation; and uniform core size, $\partial a/\partial s = O(a^2\kappa^2)$, where s is arclength.

A vortex filament with thin core is considered while axial flow is neglected for now.

According to the formulation in MS72, forces acting on an infinitesimal section of filament can be divided into two categories, $\mathbf{F}_E$ and $\mathbf{F}_I$, referred to exterior and interior forces respectively. The exterior force is the force per unit length exerted on the filament core boundary by the fluid outside, and is given by

$$\mathbf{F}_E = \Gamma \left(\boldsymbol{V}_E + \boldsymbol{V}_I - \frac{\partial \boldsymbol{R}}{\partial t} \right) \times \boldsymbol{t} + \frac{\Gamma^2}{4\pi} \kappa \boldsymbol{n} \left(\ln \frac{8}{a\kappa} - 1 \right). \tag{2.1}$$

Here $\partial \boldsymbol{R}/\partial t$ is the local motion of the filament itself, $\boldsymbol{V}_E$ is the background flow evaluated at the filament centerline, and $\boldsymbol{V}_I$ is the velocity contributed by the rest of the filament. It accounts for the non-singular part of Biot-Savart law and can be evaluated using the desingularized Biot-Savart integral,

$$\boldsymbol{V}_I(\boldsymbol{R}_0) = \frac{\Gamma}{4\pi} \left[\int \frac{\mathrm{d}\boldsymbol{R} \times (\boldsymbol{R}_0 - \boldsymbol{R})}{|\boldsymbol{R}_0 - \boldsymbol{R}|^3} - \int \frac{\mathrm{d}\boldsymbol{R}_\odot \times (\boldsymbol{R}_0 - \boldsymbol{R}_\odot)}{|\boldsymbol{R}_0 - \boldsymbol{R}_\odot|^3} \right]. \tag{2.2}$$

The notation $\boldsymbol{R}_0$ in the second integral indicates that it is taken along the osculating circle to $\boldsymbol{R}$ at $\boldsymbol{R}_0$, the point at which $\boldsymbol{V}_I$ is being evaluated. The first term on the RHS of (2.1) is the Kutta-Joukowski lift on the filament. The last two terms are the effect of pressure reduction on the core boundary due to the curvature of filament. The vectors $\boldsymbol{t}$, $\boldsymbol{n}$ are local unit tangent and normal vectors defined by

$$\boldsymbol{t} = \frac{\partial \boldsymbol{R}/\partial \xi}{|\partial \boldsymbol{R}/\partial \xi|}, \qquad \kappa \boldsymbol{n} = \frac{\partial \boldsymbol{t}}{\partial s}, \tag{2.3}$$

where ξ is an arbitrary parameterization of the curve $\boldsymbol{R}$ and s is arclength. The binormal vector is the cross product of tangent and normal vectors, $\boldsymbol{b} = \boldsymbol{t} \times \boldsymbol{n}$ (see figure 2.1).

The interior force comes from integrating the pressure over the end surface and then taking the derivative along the tangent of the filament. Due to the curvature, the

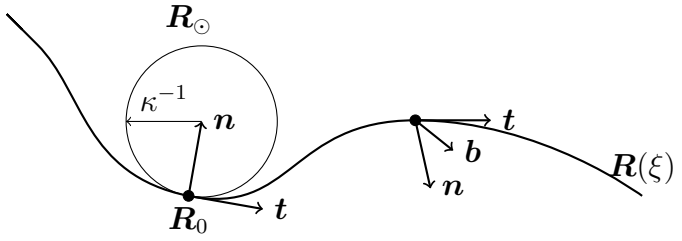

Figure 2.1: A filament $\boldsymbol{R}$ in space is parameterized by ξ. Its tangent, normal and binormal vectors are defined using the Frenet-Serret formulas. The osculating circle $\boldsymbol{R}_\odot$ associated with the point $\boldsymbol{R}_0$ has radius κ^{-1}.

net result is in the normal direction. This gives

$$\mathbf{F}_I = \pi \int_0^a r v(r)^2 \, \mathrm{d}r \kappa \boldsymbol{n} + \frac{\Gamma^2}{8\pi} \kappa \boldsymbol{n}, \tag{2.4}$$

where $v(r)$ is the azimuthal velocity within the core. The second term on the RHS matches the pressure reduction on the boundary from outside. This represents the force acting on the both ends of an infinitesimal filament. We have not included axial flow yet, so this is solely due to the pressure. Then the balance of forces, which is correct to $O(a^2\kappa^2)$ based on the assumptions at the beginning of § 2, gives

$$\mathbf{F}_E + \mathbf{F}_I = 0, \tag{2.5}$$

and the motion is determined by taking cross product of the force balance with the tangent $\boldsymbol{t}$,

$$\frac{\partial \boldsymbol{R}}{\partial t} = \boldsymbol{V}_E + \boldsymbol{V}_I + \frac{\Gamma}{4\pi} \kappa \boldsymbol{b} \left(\ln \frac{8}{a\kappa} - \frac{1}{2} + \frac{\mu}{4} \right), \tag{2.6}$$

with

$$\mu = \frac{1}{2} a^2 \overline{v^2} = \frac{16\pi^2}{\Gamma^2} \int_0^a r v(r)^2 \, \mathrm{d}r \tag{2.7}$$

and the bar denoting the average over the cross-section. For the motion of a vortex ring

in a quiescent fluid, this gives

$$\frac{\partial \boldsymbol{R}}{\partial t} = \frac{\Gamma}{4\pi}\kappa \boldsymbol{b}\left(\ln\frac{8}{a\kappa} - \frac{1}{2} + \frac{\mu}{4}\right), \tag{2.8}$$

since $\boldsymbol{V}_I$ vanishes for rings. The parameter μ is determined by the flow structure inside the core. If the vorticity is uniform within the core, $\mu = 1$ while $\mu = 0$ for a hollow core. In the discussion so far, the density has been constant.

2.2.2 Motion with buoyancy

Now we consider density difference by setting the core density to ρ_2 and outside density to ρ_1. The exterior forces account for the forces acting on the boundary which forms the lateral surface of the element. In § 5 of MS72, the velocity on the boundary is first obtained by matching the asymptotic solutions from both sides. The flow is irrotational outside, so the potential and the boundary are expanded in κ

$$\phi = \phi_0 + \phi_1 + \phi_2 + \cdots, \qquad a = a_0 + a_1 + a_2 + \cdots. \tag{2.9}$$

Then the pressure is computed using Bernoulli's equation, (5.16) of MS72. The calculation for velocity is kinematic so we follow it. Adding gravity to Bernoulli's equation gives

$$p + \rho_1\left[\frac{1}{2}(\boldsymbol{\nabla}\phi_0)^2 + \boldsymbol{\nabla}\phi_0 \cdot \boldsymbol{\nabla}\phi_1 - \frac{\partial \boldsymbol{R}}{\partial t}\cdot\boldsymbol{\nabla}\phi_0 + (z - Z)g\right] = 0, \tag{2.10}$$

where the local r-θ plane is perpendicular to $\boldsymbol{t}$ and $z = Z$ is the vertical position of the centerline (see figure 2.2). The leading-order potentials ϕ_0 is given in (5.8) of MS72 as

$$\phi_0 = \frac{\Gamma\theta}{2\pi}. \tag{2.11}$$

The first-order potential is then given in (5.15) of MS72 as

$$\begin{aligned}\phi_1 =&(\boldsymbol{V}_E + \boldsymbol{V}_I)\cdot(X\boldsymbol{n} + Y\boldsymbol{b}) - \frac{a_0^2}{r^2}\left(\frac{\partial \boldsymbol{R}}{\partial t} - \boldsymbol{V}_E - \boldsymbol{V}_I\right)\cdot(X\boldsymbol{n} + Y\boldsymbol{b}) + \frac{\Gamma Y}{4\pi}\kappa \ln\frac{8}{r\kappa} \\ &+ \frac{\Gamma Y a_0^2}{4\pi r^2}\kappa\left(\ln\frac{8}{a_0\kappa} - 1\right) + \int(\boldsymbol{V}_E + \boldsymbol{V}_I)\cdot\boldsymbol{t}\,\mathrm{d}s,\end{aligned} \tag{2.12}$$

where (X, Y) are coordinates on the $\boldsymbol{n}$-$\boldsymbol{b}$ plane of the Frenet–Serret frame scaled by $O(\kappa^{-1})$ so that $\mathbf{x} = \boldsymbol{R} + X\boldsymbol{n} + Y\boldsymbol{b}$.

Therefore the pressure is given by (compare with 5.17 in MS72)

$$p = \rho_1\left[-\frac{\Gamma^2}{8\pi^2 a^2} + \frac{\Gamma}{\pi a}\left(\frac{Y}{a}\mathbf{Q}\cdot\boldsymbol{n} - \frac{X}{a}\mathbf{Q}\cdot\boldsymbol{b}\right) - \frac{\Gamma^2 X}{4\pi^2 a^2}\kappa\left(\ln\frac{8}{a\kappa} - \frac{1}{2}\right)\right] + \rho_1(Z - z)g, \tag{2.13}$$

where $\mathbf{Q} = \boldsymbol{V}_E + \boldsymbol{V}_I - \partial\boldsymbol{R}/\partial t$ is the relative velocity between the surrounding fluid and the vortex filament. Integrating the pressure per unit length $\mathrm{d}s$ we obtain the exterior force,

$$\mathbf{F}_E = \rho_1\left[\Gamma\mathbf{Q}\times\boldsymbol{t} + \frac{\Gamma^2}{4\pi}\left(\ln\frac{8}{a\kappa} - \frac{1}{2}\right)\kappa\boldsymbol{n} - \frac{\Gamma^2}{8\pi}\kappa\boldsymbol{n} + \pi a^2 g\mathbf{z}\right], \tag{2.14}$$

where $g\mathbf{z} = -\boldsymbol{g}$ and the last term is the weight of the surrounding fluid displaced by the filament, i.e. Archimedes' principle. Note that on the boundary $r = a$, as $X, Y \to 0$, the pressure becomes

$$p(r = a) = p_a = \rho_1\left[-\frac{\Gamma^2}{8\pi^2 a^2} + (Z - z)g\right]. \tag{2.15}$$

This will be the boundary condition for the subsequent calculation of the interior forces.

MS72 starts its discussion of the interior forces by calculating the pressure acting on both ends of the segment. In MS72, the pressure is assumed to be symmetric about the centerline of the filament and calculated using (6.1) from MS72. Here we include density

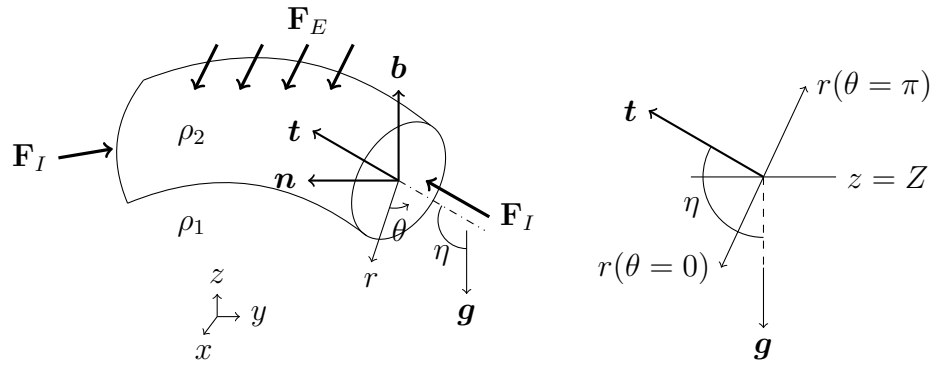

Figure 2.2: The coordinate system on a small element of the filament. The unit tangent $\boldsymbol{t}$ is perpendicular to the r-θ plane and its angle with the gravity is η. We define $\theta = 0$ when the angle between r and $\boldsymbol{g}$ is minimal.

and gravity, yielding

$$\frac{\partial p}{\partial r} = \rho_2 \left(\frac{v_0^2}{r} + g_r \right), \tag{2.16}$$

where r is the local radial coordinate and v_0 is the azimuthal velocity in the interior. g_r is the projection of gravity on r. The pressure depends on r and θ while it depends only on r in MS72.

The force due to pressure acting on one end is

$$\begin{aligned} -\int_0^{2\pi}\int_0^a pr\,\mathrm{d}r\,\mathrm{d}\theta &= \frac{1}{2}\int_0^{2\pi}\left[\int_0^a r^2\frac{\partial p}{\partial r}\,\mathrm{d}r - a^2 p(r=a)\right]\mathrm{d}\theta \\ &= \frac{1}{2}\left(\rho_2\pi a^2\overline{v^2} + \int_0^{2\pi}\int_0^a r^2 g_r\,\mathrm{d}r\,\mathrm{d}\theta\right) + \rho_1\left(\frac{\Gamma^2}{8\pi} - \pi a^2 g s\cos\eta\right), \end{aligned} \tag{2.17}$$

where the bar indicates the average over the end surface area. The double integral vanishes since $g_r = r\cos\theta\ g\sin\eta$. The last two terms come from evaluating the pressure on $r = a$ and using the geometric relation $z - Z = -(r\cos\theta\sin\eta + s\cos\eta)$, which illustrated in figure 2.2. The pressure force on the end acting along the filament is calculated by differentiating (2.17) with respect to s,

$$\rho_2\frac{\partial}{\partial s}\left(\frac{1}{2}\pi a^2\overline{v^2}\boldsymbol{t}\right) + \rho_1\left(\frac{\Gamma^2}{8\pi}\kappa\boldsymbol{n} - \pi a^2 g\cos\eta\ \boldsymbol{t}\right). \tag{2.18}$$

When axial flow is nonzero, there are two additional contributions to the interior force $\mathbf{F}_I$: the tangential momentum flux across the two ends of the infinitesimal filament, and the rate of change of tangential momentum inside. The momentum flux across the ends is given by combining (6.4) and (6.5) of MS72,

$$-\rho_2 \iint w \left(w\boldsymbol{t} + \mathbf{u}_\perp + \frac{\partial \boldsymbol{R}}{\partial t} \right) \mathrm{d}A = -\rho_2 \left(\pi a^2 \overline{w^2}\boldsymbol{t} + \frac{a^2 \overline{w} \Gamma}{4} \kappa \boldsymbol{b} + \pi a^2 \overline{w} \frac{\partial \boldsymbol{R}}{\partial t} \right), \tag{2.19}$$

where w is the axial flow and the bar means the average over the cross section. The momentum flux carried by the mean axial flow is decomposed into local tangential component, local perpendicular component ($\mathbf{u}_\perp$ on the r-θ plane) and the motion of the filament, which correspond to those three terms respectively. The rate of change of tangential momentum inside is given by MS72 (6.6),

$$-\rho_2 \frac{\partial \xi}{\partial s} \frac{\partial}{\partial t} \left(\pi a^2 \overline{w} \boldsymbol{t} \frac{\partial s}{\partial \xi} \right) = -\rho_2 \left[\pi \frac{\partial}{\partial t} (a^2 \overline{w} \boldsymbol{t}) + \pi a^2 \overline{w} \boldsymbol{t} \frac{\partial}{\partial t} \left(\ln \frac{\partial s}{\partial \xi} \right) \right]. \tag{2.20}$$

We have a density ρ_2 for the filament, so the two equations above are multiplied by ρ_2. Finally, we combine all the interior forces (2.18)–(2.20) and obtain

$$\begin{aligned} \mathbf{F}_I =& \rho_2 \pi \frac{\partial}{\partial s} \left[\left(\frac{1}{2} a^2 \overline{v^2} - a^2 \overline{w^2} \right) \boldsymbol{t} - a^2 \overline{w} \frac{\partial \boldsymbol{R}}{\partial t} - \frac{a^2 \overline{w} \Gamma}{4\pi} \kappa \boldsymbol{b} \right] - \rho_1 \pi a^2 g \cos\eta \, \boldsymbol{t} \\ & - \rho_2 \pi \left[\frac{\partial}{\partial t} (a^2 \overline{w} \boldsymbol{t}) + a^2 \overline{w} \boldsymbol{t} \frac{\partial}{\partial t} \left(\ln \frac{\partial s}{\partial \xi} \right) \right] + \rho_1 \frac{\Gamma^2}{8\pi} \kappa \boldsymbol{n}. \end{aligned} \tag{2.21}$$

We balance all the forces using

$$\mathbf{F}_E + \mathbf{F}_I + \mathbf{F}_B = 0, \tag{2.22}$$

where $\mathbf{F}_B = \rho_2 \pi a^2 \boldsymbol{g}$ is the body force, i.e. the filament's weight. The transverse component

of the force balance becomes

$$\begin{aligned}&\rho_1\left[\Gamma\mathbf{Q}\times\boldsymbol{t}+\frac{\Gamma^2}{4\pi}\left(\ln\frac{8}{a\kappa}-\frac{1}{2}\right)\kappa\boldsymbol{n}\right]+(\rho_1-\rho_2)\pi a^2 g\left[\mathbf{z}-(\boldsymbol{t}\cdot\mathbf{z})\boldsymbol{t}\right]\\&+\rho_2\pi\left(\frac{1}{2}a^2\overline{v^2}-a^2\overline{w^2}+\frac{a^2\overline{w}\Gamma}{4\pi}\tau\right)\kappa\boldsymbol{n}-\rho_2\left[2\pi a^2\overline{w}\frac{\partial\boldsymbol{t}}{\partial t}+\Gamma\frac{\partial}{\partial s}\left(\frac{a^2\overline{w}}{4}\kappa\right)\boldsymbol{b}\right]=0.\end{aligned}\tag{2.23}$$

Note that $\partial\boldsymbol{b}/\partial s=-\tau\boldsymbol{n}$ where τ is torsion. The $\boldsymbol{t}$-component is related to the core structure which will be discussed in the next section. The motion is given by taking the cross product of $\boldsymbol{t}$ with (2.23),

$$\begin{aligned}\frac{\partial\boldsymbol{R}}{\partial t}=&\boldsymbol{V}_E+\boldsymbol{V}_I+\frac{\Gamma}{4\pi}\kappa\boldsymbol{b}\left(\ln\frac{8}{a\kappa}-\frac{1}{2}+\frac{1}{4}\frac{\rho_2}{\rho_1}\right)+\left(1-\frac{\rho_2}{\rho_1}\right)\frac{\pi a^2 g}{\Gamma}\boldsymbol{t}\times\mathbf{z}\\&+\frac{\rho_2}{\rho_1}\left(-\frac{\pi a^2\overline{w^2}}{\Gamma}+\frac{a^2\overline{w}}{4}\tau\right)\kappa\boldsymbol{b}-\frac{\rho_2}{\rho_1}\left[\frac{2\pi a^2\overline{w}}{\Gamma}\boldsymbol{t}\times\frac{\partial\boldsymbol{t}}{\partial t}-\frac{\partial}{\partial s}\left(\frac{a^2\overline{w}}{4}\kappa\right)\boldsymbol{n}\right].\end{aligned}\tag{2.24}$$

To calculate the motion of a buoyant vortex filament using (2.24), one still needs the evolution equations for a and $\overline{w}$ which will be derived in the following section.

2.3 The internal structure

In order to calculate $\overline{w}$, we look into the flow structure within the core. This is achieved by examining the tangential component of (2.22):

$$\begin{aligned}&\rho_2\pi\frac{\partial}{\partial s}\left(\frac{1}{2}a^2\overline{v^2}-a^2\overline{w^2}\right)-2\rho_2\pi a^2\overline{w}\frac{\partial}{\partial t}\left(\ln\frac{\partial s}{\partial\xi}\right)-\rho_2\pi\left[V_{||}\frac{\partial}{\partial s}(a^2\overline{w})+\frac{\partial}{\partial t}(a^2\overline{w})\right]\\=&(\rho_1-\rho_2)\pi a^2 g\cos\eta\end{aligned}\tag{2.25}$$

where $V_{||}=\boldsymbol{t}\cdot\partial\boldsymbol{R}/\partial t$ is the tangential velocity. Buoyancy contributes an extra term when we compare (2.25) to (8.15) in MS72. To simplify the tangential equation, (8.5) in MS72, the decomposition $w=W(t)+q(s,t)+\Gamma\chi(r/a)/b$ is used, with a constant length b and with $\chi(r/a)$ the variation of w in the r-θ plane. This is justified based on the argument

that q is $O(\kappa)$. We shall use

$$w = \overline{w}(s,t) + \frac{\Gamma}{b}\chi(\frac{r}{a}) \tag{2.26}$$

for buoyant case here, since the dependence of w on s (and ξ) is $O(1)$ and $\overline{\chi} = 0$. We then obtain

$$\overline{w^2} = \overline{w}^2(s,t) + \frac{\Gamma^2}{b^2}\nu \tag{2.27}$$

with a constant

$$\nu = 2\int_0^a \chi^2(\frac{r}{a})\ r\mathrm{d}r. \tag{2.28}$$

The continuity equation in (8.10) of MS72 for the vorticity core is

$$\frac{\partial\xi}{\partial s}\frac{\partial}{\partial t}\left(a^2\frac{\partial s}{\partial\xi}\right) + a^2\frac{\partial\overline{w}}{\partial s} = 0. \tag{2.29}$$

For incompressible flow, the volume of the core is conserved with a uniform core size so that

$$\frac{\mathrm{d}}{\mathrm{d}t}(a^2 L) = 0, \tag{2.30}$$

where $L(t)$ is the total length of the filament. It can be shown that using (3.5) and (2.30),

$$\frac{\partial\overline{w}}{\partial s} = -\frac{\partial}{\partial t}\left(\ln\frac{\partial s}{\partial\xi}\right) + \frac{1}{L}\frac{\mathrm{d}L}{\mathrm{d}t}, \tag{2.31}$$

which is identical to (8.12) in MS72. From (2.7) we find that $a^2\overline{v^2}$ is a constant with respect to s and (3.3) gives $\partial\overline{w^2}/\partial s = \partial\overline{w}^2/\partial s$. The tangential component then becomes

$$-\rho_2\pi\frac{D}{Dt}(L\overline{w}) = (\rho_1 - \rho_2)\pi L g\cos\eta, \tag{2.32}$$

where $D/Dt = \partial/\partial t + V_{||}\partial/\partial s$ is defined to be the material derivative along the filament.

In general, the buoyancy force will accelerate or decelerate the axial flow inside the

core. An exception is when the the tangent vector and gravity are perpendicular to each other, i.e. $\eta = \pi/2$; in this case $L\overline{w}$ is conserved. We will examine a nearly horizontal ring in this circumstance in the next section. It is worth noting that in the hollow vortex limit where $\rho_2 \to 0$, the equation becomes singular. This is due to our assumption of slow time which removes the small time scale and the large acceleration due to an adjustment to balance with the RHS of (2.32). The remedy should be reformulating the force balance and including the inertial term. However, such a treatment lies beyond the scope of this chapter. For a buoyant vortex filament of a given shape $\boldsymbol{R}$, its motion can be calculated using (2.24) and (3.2) with a given density ratio, ρ_2/ρ_1. For the case of non-zero axial flow inside the core, an additional equation (2.32) is coupled with (2.24) and (2.30) to determine the motion of a buoyant vortex filament.

2.4 Solution for buoyant rings

We consider a vortex ring $\boldsymbol{R}$ of light fluid in a heavier ambient, centered at the origin with radius R_0 and its axis initially inclined at an angle α_0 from the direction of gravity (see Figure 2.3). The equation of motion (2.24) for the ring becomes

$$\begin{aligned}\frac{\partial \boldsymbol{R}}{\partial t} = \frac{\Gamma}{4\pi R}\boldsymbol{b}\left(\ln\frac{8R}{a} - \frac{1}{2} + \frac{1}{4}\frac{\rho_2}{\rho_1}\right) + \left(1 - \frac{\rho_2}{\rho_1}\right)\frac{\pi a^2 g}{\Gamma}\boldsymbol{t}\times\mathbf{z} \\ + \frac{\rho_2}{\rho_1}\left[-\frac{\pi a^2\overline{w^2}}{\Gamma R}\boldsymbol{b} - \frac{2\pi a^2\overline{w}}{\Gamma}\boldsymbol{t}\times\frac{\partial \boldsymbol{t}}{\partial t} + \frac{a^2}{4R}\frac{\partial \overline{w}}{\partial s}\boldsymbol{n}\right].\end{aligned} \tag{2.33}$$

The ring radius R will vary in time, but the volume of the core is conserved for incompressible flow:

$$a^2 R = a_0^2\ R_0. \tag{2.34}$$

2.4.1 Formulation

We use local coordinates on the ring defined by

$$\boldsymbol{R}(t,\theta) = \boldsymbol{X}_c(t) + R(t) \begin{bmatrix} \cos\theta\cos\alpha(t) \\ \sin\theta \\ \cos\theta\sin\alpha(t) \end{bmatrix}, \tag{2.35}$$

whose time derivative is

$$\frac{\partial \boldsymbol{R}}{\partial t} = \frac{\mathrm{d}\boldsymbol{X}_c}{\mathrm{d}t} + \frac{\mathrm{d}R}{\mathrm{d}t} \begin{bmatrix} \cos\theta\cos\alpha \\ \sin\theta \\ \cos\theta\sin\alpha \end{bmatrix} + R\frac{\mathrm{d}\alpha}{\mathrm{d}t} \begin{bmatrix} -\cos\theta\sin\alpha \\ 0 \\ \cos\theta\cos\alpha \end{bmatrix}. \tag{2.36}$$

Using the Frenet–Serret formulas, we obtain

$$\boldsymbol{n} = \begin{bmatrix} -\cos\theta\cos\alpha \\ -\sin\theta \\ -\cos\theta\sin\alpha \end{bmatrix}, \quad \boldsymbol{b} = \begin{bmatrix} -\sin\alpha \\ 0 \\ \cos\alpha \end{bmatrix}, \quad \boldsymbol{t} \times \frac{\partial \boldsymbol{t}}{\partial t} = \boldsymbol{n}\frac{\mathrm{d}\alpha}{\mathrm{d}t}\sin\theta. \tag{2.37}$$

The equation of motion (4.1) becomes

$$\frac{\partial \boldsymbol{R}}{\partial t} = \frac{U+W_1}{R} \begin{bmatrix} -\sin\alpha \\ 0 \\ \cos\alpha \end{bmatrix} + \frac{\beta}{R} \begin{bmatrix} \cos\theta \\ \sin\theta\cos\alpha \\ 0 \end{bmatrix} + \frac{W_2}{R} \begin{bmatrix} -\cos\theta\cos\alpha \\ -\sin\theta \\ -\cos\theta\sin\alpha \end{bmatrix} \tag{2.38}$$

where

$$U(R) = \frac{\Gamma}{4\pi}\left(\frac{3}{2}\ln 4R - \frac{1}{2}\ln a_0^2 R_0 - \frac{1}{2} + \frac{1}{4}\frac{\rho_2}{\rho_1}\right), \quad \beta = \frac{\pi a_0^2 R_0}{\Gamma}\left(1 - \frac{\rho_2}{\rho_1}\right) g \tag{2.39}$$

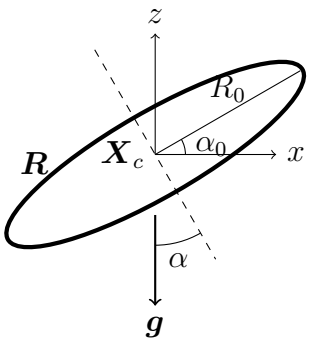

Figure 2.3: Initial setting of a vortex ring is tilting an angle α_0 from x axis. Gravity $\boldsymbol{g}$ is in the negative z direction.

come from vorticity and buoyancy, while

$$W_1(R) = -\frac{\rho_2}{\rho_1}\frac{\pi a_0^2 R_0 \overline{w^2}}{\Gamma R}, \quad W_2(R,\theta) = \frac{\rho_2}{\rho_1}\left(-\frac{2\pi a_0^2 R_0 \overline{w}}{\Gamma}\frac{\mathrm{d}\alpha}{\mathrm{d}t}\sin\theta + \frac{a_0^2 R_0}{4R}\frac{\partial \overline{w}}{\partial s}\right) \tag{2.40}$$

are associated with axial flow inside the core.

Combining (2.36) and (2.38), we obtain a set of evolution equations for $\boldsymbol{X}_c$:

$$\frac{\mathrm{d}x_c}{\mathrm{d}t} = -\frac{U+W_1}{R}\sin\alpha, \quad \frac{\mathrm{d}y_c}{\mathrm{d}t} = 0, \quad \frac{\mathrm{d}z_c}{\mathrm{d}t} = \frac{U+W_1}{R}\cos\alpha, \tag{2.41}$$

which is coupled to the evolution of R and α by

$$\frac{\mathrm{d}R}{\mathrm{d}t} = \frac{\beta}{R}\cos\alpha - \frac{W_2}{R}, \quad \frac{\mathrm{d}\alpha}{\mathrm{d}t} = -\frac{\beta}{R^2}\sin\alpha, \quad \frac{\mathrm{d}}{\mathrm{d}t}(R\sin\alpha) = -\frac{W_2}{R}\sin\alpha. \tag{2.42}$$

For a ring with density equal to the ambient value, there is no buoyancy, so that $\beta = 0$ and $\mathrm{d}\alpha/\mathrm{d}t = 0$. Then if the axial flow $\overline{w}$ is a constant then $W_2 = 0$ and W_1 is a constant. Therefore $\mathrm{d}R/\mathrm{d}t = 0$ and the ring radius remains constant. As we know, a vortex ring with no buoyancy just moves without expansion or turning. Axial flow changes its translation speed by $-\pi a^2\overline{w^2}/R\Gamma$.

When buoyancy is present, $\beta \neq 0$. Axial flow is locally accelerated due to the pres-

sure gradient discussed in section 3. In this case, $\overline{w}$ has temporal and spatial dependence, and $\mathrm{d}R/\mathrm{d}t$ varies with θ. As a result, the ring cannot maintain its circular shape and (2.35) becomes invalid. On the other hand, if axial flow is always negligible, an analytic solution for (2.41) and (2.42) can be derived. We may take the ring to be nearly horizontal, so that $\cos\eta \approx 0$ and (2.32) gives the solution $\overline{w} \approx 0$. Then we may solve the evolution equations analytically.

2.4.2 A slightly non-horizontal buoyant ring

According to Turner (1957) and Pedley (1968), we know that the radius of a horizontal ring grows as it rises. We also anticipate that α will decrease, so that the ring will turn toward the horizontal. Here we take the initial angle α_0 to be small, and require no axial flow so that $W_1 = W_2 = 0$ while keeping the buoyancy term. The evolution equations become

$$\frac{\mathrm{d}x_c}{\mathrm{d}t} = -\frac{U}{R}\sin\alpha, \quad \frac{\mathrm{d}y_c}{\mathrm{d}t} = 0, \quad \frac{\mathrm{d}z_c}{\mathrm{d}t} = \frac{U}{R}\cos\alpha, \tag{2.43}$$

$$\frac{\mathrm{d}R}{\mathrm{d}t} = \frac{\beta}{R}\cos\alpha, \quad \frac{\mathrm{d}\alpha}{\mathrm{d}t} = -\frac{\beta}{R^2}\sin\alpha, \quad \frac{\mathrm{d}}{\mathrm{d}t}(R\sin\alpha) = 0. \tag{2.44}$$

The last equation gives $R\sin\alpha = R_0\sin\alpha_0$. Then we solve for α by integrating (4.12b) to obtain

$$\int^{\alpha} \frac{\mathrm{d}\alpha'}{\sin^3\alpha'} = -\frac{\beta t}{R_0^2\sin^2\alpha_0} + C_1.$$

The integral on the left hand side can be evaluated using the initial condition $\alpha(t=0) = \alpha_0$, giving

$$\frac{\beta t}{R_0^2\sin^2\alpha_0} = \frac{1}{2}\left(\csc\alpha\cot\alpha - \csc\alpha_0\cot\alpha_0 + \ln\frac{\csc\alpha_0 - \cot\alpha_0}{\csc\alpha - \cot\alpha}\right). \tag{2.45}$$

Since α is an implicit function of time, we will also solve other quantities implicitly in terms of α rather than explicitly in time. The radius is found by integrating (4.12a), yielding

$$\frac{1}{2}\mathrm{d}R^2 = \beta\cos\alpha\frac{\mathrm{d}t}{\mathrm{d}\alpha}\mathrm{d}\alpha. \tag{2.46}$$

With $R(\alpha_0) = R_0$, the solution is

$$R(\alpha) = R_0\frac{\sin\alpha_0}{\sin\alpha}. \tag{2.47}$$

It is trivial to conclude that $y_c(t) = 0$. Integrating the equations for $x_c(t)$, $z_c(t)$ with initial condition $(0, 0)$ yields

$$x_c(t) = \frac{\Gamma}{4\pi}R_0\sin\alpha_0\left[A_0\left(\ln\frac{\csc\alpha - \cot\alpha}{\csc\alpha_0 - \cot\alpha_0}\right) - \frac{3}{2}\int_{\alpha_0}^{\alpha}\frac{\ln(\sin\alpha')}{\sin\alpha'}d\alpha'\right] \tag{2.48}$$

and

$$z_c(t) = \frac{\Gamma}{4\pi}R_0\sin\alpha_0\left\{A_0(\csc\alpha - \csc\alpha_0) - \frac{3}{2}\left[\frac{\ln(\sin\alpha)+1}{\sin\alpha} - \frac{\ln(\sin\alpha_0)+1}{\sin\alpha_0}\right]\right\}, \tag{2.49}$$

where

$$A_0 = \frac{3}{2}\ln(R_0\sin\alpha_0) + \ln\frac{8}{a_0\sqrt{R_0}} - \frac{1}{2} + \frac{1}{4}\frac{\rho_2}{\rho_1}$$

is a constant determined by the initial condition. The integral in x_c is related to the dilogarithm function Li_2 and is given by

$$\begin{aligned}\int_{\alpha_0}^{\alpha}\frac{\ln(\sin\alpha')}{\sin\alpha'}\mathrm{d}\alpha' = &-\frac{1}{4}\ln 2\left[\ln\frac{1+\cos\alpha}{1-\cos\alpha} - \ln\frac{1+\cos\alpha_0}{1-\cos\alpha_0}\right]\\ &+\frac{1}{8}\left[\ln^2(1-\cos\alpha) - \ln^2(1+\cos\alpha) - \ln^2(1-\cos\alpha_0) + \ln^2(1+\cos\alpha_0)\right]\\ &+\frac{1}{4}\left[Li_2(\frac{1+\cos\alpha}{2}) - Li_2(\frac{1-\cos\alpha}{2}) - Li_2(\frac{1+\cos\alpha_0}{2}) + Li_2(\frac{1-\cos\alpha_0}{2})\right].\end{aligned} \tag{2.50}$$

2.4.3 Long time behavior

Using the small angle expansion, we approximate

$$\frac{\beta t}{R_0^2 \sin^2 \alpha_0} = \frac{1}{2}\left(\alpha^{-2} - \ln \frac{\alpha}{2}\right) + O(1), \tag{2.51}$$

so that, to leading order,

$$\alpha(t) \approx \frac{R_0 \sin \alpha_0}{\sqrt{2\beta t}}. \tag{2.52}$$

Therefore, we need $\alpha \to 0$ as $t \to \infty$. The ring turns to the horizontal for long times.

The radius is approximately

$$R(t) = R_0 \frac{\sin \alpha_0}{\sin \alpha(t)} \approx \sqrt{2\beta t}. \tag{2.53}$$

This asymptotic behavior agrees with the investigations by Turner (1957) and Lundgren & Mansour (1991).

The trajectory is approximately

$$x_c \approx -\frac{3\Gamma}{64\pi} R_0 \sin \alpha_0 \left[(\ln t)^2 + \frac{8}{3} A_0 \ln t\right]; \quad z_c \approx \frac{3\Gamma}{16\pi}\sqrt{2\beta}\; t^{\frac{1}{2}} \ln t, \tag{2.54}$$

where x_c should be asymptotically a constant as $t \to \infty$. If we differentiate z_c with respect to time, we find

$$\frac{\mathrm{d}z_c}{\mathrm{d}t} \approx \frac{3\Gamma}{16\pi}\sqrt{2\beta}\; t^{-\frac{1}{2}} \left(\frac{1}{2}\ln t + 1\right). \tag{2.55}$$

This agrees with Pedley's result of the speed varying as $t^{-1/2} \ln t$ for a horizontal ring.

2.5 Conclusion

We have studied the motion of a buoyant vortex filament using a force balance approach, to take account for all the forces acting on a element of vortex whose density is different from its surrounding fluid. Buoyancy forces arise from integrating pressure over the boundary. For a simple geometry such as a ring, buoyancy causes its radius to increase when it moves against gravity; conversely a buoyant ring moving downward will shrink. The motion of a buoyant filament also depends on axial flow inside its core. An investigation of the internal structure shows that axial flow is generated inside the core, and its rate of change is proportional to the projection of gravity on the local tangent. The acceleration/deceleration of axial flow reaches maximum when the background pressure gradient aligns with the local tangent. If the tangent vector is horizontal, there is locally no acceleration of axial flow.

A set of equations (2.24), (2.30) and (2.32) are obtained for the motion of a buoyant vortex filament. For a filament of arbitrary shape, the calculation needs to be carried out numerically. For a simple circular geometry, we obtain an exact solution for the evolution of an initially non-horizontal ring, valid when the ring has small inclination so that axial flow is not significant. Our calculation shows that buoyancy will change the orientation of the ring and turn it to the horizontal. Our asymptotic solution agree with the results of Turner (1957) and Pedley (1968).

The solution for a ring given here is restricted by several assumptions. It is worth investigating when the angle α becomes large. In this case, it is also important to examine the effect of axial flow which becomes non-trivial and a numerical calculation is required. The other extension is to investigate a buoyant vortex ring with large core radius using axisymmetric contour dynamics. The stability analysis on a buoyant vortex ring is another intriguing topic.

Chapter 2, in full, has been published in the Journal of Fluid Mechanics, "The motion of a buoyant vortex filament" by C. Chang and S. G. Llewellyn Smith, 2018, **857**, R1 (Cambridge University Press). The dissertation author was the primary investigator and author of this material.

Chapter 3

Axisymmetric contour dynamics for buoyant vortex rings

This chapter uses a reduced order model to study the motion of a buoyant vortex ring with non-negligible core size. Buoyancy is considered in both non-Boussinesq and Boussinesq situations using an axisymmetric contour dynamics formulation. The density of the vortex ring differs from that of the ambient fluid, and both densities are constant and conserved. The motion of the ring is calculated by following the boundary of the vortex core, which is also the interface between the two densities. The velocity of the contour comes from a combination of a specific continuous vorticity distribution within its core and a vortex sheet on the core boundary. An evolution equation for the vortex sheet is derived from the Euler equation, which simplifies considerably in the Boussinesq limit. Numerical solutions for the coupled integro-differential equations are obtained. The dynamics of the vortex sheet and the formation of two possible singularities, including singularities in the curvature and the shock-like profile of the vortex sheet strength, are discussed. Three dimensionless groups, the Atwood, Froude and Weber numbers, are introduced to measure the importance of physical effects acting on the motion of a buoyant vortex ring.

3.1 Introduction

Vortex rings have attracted much attention from applied mathematicians and fluid dynamicists over the history of vortex dynamics. Early studies can be traced back to the work of Thomson (1867*b*) and Hicks (1884). Their theories for the steady motion of a vortex ring assumed that the core is small and circular. The vortex core refers to the region enclosed by a contour shown in figure 3.1. The area of that region allows us to define a vortex core radius a. If a is very small compared to the radius of the vortex ring about its axis of symmetry, we define it as a thin ring; otherwise the ring is "fat". A detailed description of the profile of the vortical core was missing until Fraenkel (1972) provided an asymptotic formulation for small cross-section rings. Norbury (1972) found steady "fat" vortex rings close to the Hill's spherical vortex. Norbury (1973) then connected the previous two solutions via a one-parameter family of steady vortex rings ranging from thin to fat rings. This solution has an azimuthal vorticity distribution inside the ring given by

$$\omega_\phi = r\Omega, \tag{3.1}$$

where r is the radial distance to the axis of symmetry and Ω is constant. Then ω_ϕ satisfies the vorticity equation in axisymmetric geometry,

$$\frac{\mathrm{D}}{\mathrm{D}t}\left(\frac{\omega_\phi}{r}\right) = 0, \tag{3.2}$$

where $\mathrm{D}/\mathrm{D}t$ is the material derivative. We are using cylindrical coordinates (r, ϕ, z).

In general, classic vortex dynamics deals with incompressible, inviscid Euler flows. The flows are dominated by vorticity and the fluid density is set constant throughout. Shariff, Leonard & Ferziger (1989) provides a comprehensive review of vortex rings, while Shariff & Leonard (1992) has a clear discussion of the formation, dynamics, interactions

and the stability of vortex rings. In many circumstances, e.g. in geophysical and environmental settings, fluid flows are not only governed by vorticity but also by other physical effects. The additional physics we want to address here is buoyancy, the combined effect of density difference and gravity. Well-known example of buoyant vortices are the bubble rings created and manipulated by dolphins (see Marten *et al.*, 1996), which might be important to understand animal behaviour. One can also observe bubble rings created by human divers in the ocean or a swimming pool. A smoke ring can be created from a fireball or a thermal plume, and smoke rings expelled from a volcano have also been observed (Velasco Fuentes, 2014). From a fluid dynamics perspective, the first study of buoyant vortex rings was the theoretical work and laboratory observations of Turner (1957). The theoretical study of Pedley (1968) confirmed Turner's finding of the expansion of a buoyant vortex ring in inviscid flows and predicted finite lifetimes for bubble rings. Chang & Llewellyn Smith (2018) calculated the motion of thin buoyant vortex filaments including a buoyant ring with a small inclination. However, these results are for thin vortex rings whose core size is much smaller than their radius.

Buoyant vortex rings with large cores have been studied theoretically and numerically by Lundgren & Mansour (1991) and Chen *et al.* (1999). Their calculations start from a spherical bubble rising due to buoyancy. The bubble is penetrated by the surrounding fluid from its bottom because of the gradient of hydrostatic pressure and then changes its topology to a bubble ring. Lundgren & Mansour (1991) used a boundary-integral method based on potential theory to calculate the motion of bubbles before and after they turned into rings. A model equation similar to that in Turner (1957) and Pedley (1968) was used when the vortex ring became very thin at later times. Chen *et al.* (1999) used the incompressible Navier–Stokes equations to calculate the transition from a spherical bubble to a bubble ring numerically. Another numerical study by Cheng, Lou & Lim (2013) carried out three-dimensional DNS that showed that a bubble ring is eventually destroyed by

instability. The recent experimental studies of Vasel-Be-Hagh, Carriveau & Ting (2015*a*) and Vasel-Be-Hagh *et al.* (2015*b*) investigate the formation and the dynamics of bubble rings along with the viscous drag acting on a buoyant vortex ring.

Here we use a contour dynamics method in axisymmetric geometry to study buoyant vortex rings. Contour dynamics was first used by Zabusky, Hughes & Roberts (1979) to calculate the nonlinear evolution of a vortex patch in two dimensions. It was later adapted to axisymmetry in Pozrikidis (1986); Shariff *et al.* (1989); see also Riley (1998) and Shariff, Leonard & Ferziger (2008). A detailed description and numerical techniques of the method can be found in Dritschel (1989) and in the review of Pullin (1992). Blyth *et al.* (2014) showed that buoyancy enters the vorticity equation through the baroclinic term. To take account of buoyancy, we assign constant densities ρ_1, ρ_2 to the surrounding fluid and the vortex ring respectively. The density gradient becomes a Dirac delta function on the interface and the baroclinic torque is zero everywhere except on the interface. As a result, vorticity is generated on the interface and forms a vortex sheet. An evolution equation for the vortex sheet is essential for buoyancy to be included into the contour dynamics formulation. Other additional physics such as magnetic force (see Hattori & Moffatt, 2006; Llewellyn Smith & Hattori, 2012) also enters in the form of a vortex sheet. A review of contour dynamics method with additional physics can be found in Llewellyn Smith *et al.* (2018). The evolution equation for vortex sheet strength between different density fluids can be found in Baker *et al.* (1982) and Baker & Xie (2011) for two-dimensional free-surface waves. A similar formulation was used with gravity absent in Sohn & Hwang (2005) and Shin, Sohn & Hwang (2018) for two-density flows. Tryggvason (1988) and Stock, Dahm & Tryggvason (2008) derived an evolution equation for a vortex sheet to investigate the problems of Rayleigh–Taylor instability and the interaction between vortices and a density interface.

Surface tension can also be important in the dynamics of buoyant vortex rings,

and the vortex sheet equation will contain a term representing surface tension. Studies including surface tension in the vortex sheet dynamics are Baker & Nachbin (1998), Shin, Sohn & Hwang (2014), Sohn (2015) and Shin *et al.* (2018). Most studies solve two-dimensional problems and with an initially straight line or a slightly perturbed vortex sheet, although Baker & Moore (1989) and Sohn (2015) study a circular vortex sheet in two dimensions.

In this chapter, calculations for a vortex sheet in axisymmetry are carried out. In § 3.2, we introduce axisymmetric contour dynamics and derive an evolution equation for the vortex sheet on the interface using the Euler equation. The relevant dimensionless numbers in this problem are also discussed. In § 3.3, we present our numerical approaches for solving the coupled integro-differential equations in axisymmetric domain. Numerical results are presented in § 3.4. We conclude in § 3.5.

3.2 Mathematical formulation

We consider a buoyant vortex ring in an ideal fluid. The governing equations are

$$\boldsymbol{\nabla} \cdot \mathbf{u} = 0, \tag{3.3}$$

$$\rho \frac{\mathrm{D}\mathbf{u}}{\mathrm{D}t} = -\boldsymbol{\nabla} p + \rho \boldsymbol{g}. \tag{3.4}$$

The cross-section of a vortex ring core forms a confined region in the r-z plane (see figure 3.1) and the vorticity is zero everywhere except inside or on this contour. The contour is material and represented by a parameterized curve $\boldsymbol{R}$. Its evolution determines the motion of the axisymmetric vortex ring. The flow is axisymmetric without swirl, so the velocity field and the vorticity field are $\mathbf{u} = (u_r, 0, u_z)$ and $\boldsymbol{\omega} = (0, \omega_\phi, 0)$, respectively. We

can calculate the motion by evolving the contour using

$$\frac{\mathrm{d}\boldsymbol{R}}{\mathrm{d}t} = \mathbf{u}, \tag{3.5}$$

where the velocity is

$$u_r = -\frac{1}{r}\frac{\partial \psi}{\partial z}, \qquad u_z = \frac{1}{r}\frac{\partial \psi}{\partial r}. \tag{3.6}$$

The Stokes streamfunction is given by

$$\psi(r, z, t) = \iint \omega_\phi(r', z', t) G(r, z|r', z')\, \mathrm{d}r'\, \mathrm{d}z', \tag{3.7}$$

and satisfies the equation

$$\frac{1}{r}\left(\frac{\partial^2}{\partial r^2} - \frac{1}{r}\frac{\partial}{\partial r} + \frac{\partial^2}{\partial z^2}\right)\psi = -\omega_\phi. \tag{3.8}$$

This differential equation is solved using the Green's function

$$G(r, z|r', z') = \frac{\sqrt{rr'}}{2\pi}\left[\left(\frac{2}{k} - k\right)K(k) - \frac{2}{k}E(k)\right], \tag{3.9}$$

where

$$k^2 = \frac{4rr'}{(r + r')^2 + (z - z')^2}. \tag{3.10}$$

Here $K(k)$ and $E(k)$ are the complete elliptic integrals of the first and second kind respectively. The double integral in (3.7) is transformed into a contour integral using Green's theorem and the velocity field in (3.6) is obtained. The velocity on the boundary is then evaluated and the contour is evolved in time. This technique is called contour dynamics. More details of contour dynamics calculation for vortex rings can be found in Pozrikidis (1986); Shariff *et al.* (1989); Riley (1998) and Shariff *et al.* (2008).

If a vortex sheet is present on the interface, the velocity will consist of contributions from both the vortex sheet on the interface and the continuous vorticity inside. The latter is referred to as a vortex patch. For a classic vortex ring with one density throughout the flow, there is only a vortex patch. Riley (1998) gives a good discussion of axisymmetric vortex patches. The continuous vorticity distribution is taken to be $\omega_\phi = r\Omega$, where Ω is a constant (see § 1). Using Green's theorem gives the contour integrals

$$\mathbf{u}_p(r,z) = \frac{\Omega}{r}\oint G\cos\theta' r'\,\mathrm{d}s'\ \hat{\mathbf{r}} + \Omega\oint [H\cos\theta'(z'-z) - G\sin\theta']\,\mathrm{d}s'\ \hat{\mathbf{z}}, \tag{3.11}$$

where s is the arc length and $\theta(r,z)$ is the angle between the outward normal to the interface and the unit vector in z (see figure 3.1). All variables with primes in the integral are functions of (r',z'). The function G is given in (3.9), while

$$H(r,z|r',z') = \frac{r'K(k)}{\pi\sqrt{(r+r')^2+(z-z')^2}}. \tag{3.12}$$

For the vortex sheet, carrying out the integral in (3.7) along the interface and using (3.6) gives the self-induced velocity of a vortex sheet with strength γ as (see Hattori & Moffatt, 2006)

$$\mathbf{u}_s(r,z) = -\frac{1}{r}\oint \frac{\partial G}{\partial z}\gamma'\,\mathrm{d}\xi'\ \hat{\mathbf{r}} + \frac{1}{r}\oint \frac{\partial G}{\partial r}\gamma'\,\mathrm{d}\xi'\ \hat{\mathbf{z}}, \tag{3.13}$$

where ξ is a parameterisation without any specific physical significance that increases clockwise along the contour (see figure 3.1). The contour is evolved using $\mathbf{u} = \mathbf{u}_p + \mathbf{u}_s$ in (3.5).

3.2.1 The non-Boussinesq case

For a vortex ring whose density differs from that of the environment, the density jump on the interface results in baroclinic generation of vorticity. Baroclinic torque creates

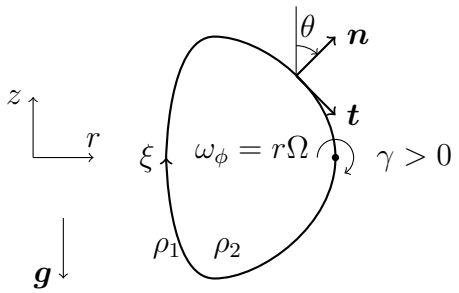

Figure 3.1: A schematic illustration of the contour in axisymmetric domain; ω_ϕ and γ are positive into the plane. The parameterisation ξ goes clockwise.

a vortex sheet on the interface. In axisymmetric geometry, the vortex sheet is composed of vorticity perpendicular to the r-z plane, i.e. in the azimuthal direction. The interface can be written as a closed curve $\boldsymbol{R} = (R(\xi, t), Z(\xi, t))$, where ξ is the parameterisation introduced earlier. The local tangent and normal vectors are

$$\boldsymbol{t} = \frac{\partial \boldsymbol{R}}{\partial \xi} \left| \frac{\partial \boldsymbol{R}}{\partial \xi} \right|^{-1}, \qquad \boldsymbol{n} = \frac{\partial \boldsymbol{t}}{\partial s} \kappa^{-1}, \tag{3.14}$$

where κ is the curvature, s is arclength, and

$$\frac{\partial s}{\partial \xi} = \left| \frac{\partial \boldsymbol{R}}{\partial \xi} \right| = L \tag{3.15}$$

is the arc length metric. The normal vector points out of the vortex.

On either side of the interface, the densities are ρ_1 and ρ_2, where the subscripts 1 and 2 indicate outside and inside. The corresponding velocities are $\mathbf{u}_1$, $\mathbf{u}_2$ and the vortex sheet strength is defined by $\gamma = L(\mathbf{u}_1 - \mathbf{u}_2) \cdot \boldsymbol{t}$. The tangential velocity on the interface is given by averaging velocities from either side, $\bar{\mathbf{u}} = (\mathbf{u}_1 + \mathbf{u}_2)/2$. A Lagrangian velocity following material points is defined by

$$\widetilde{\mathbf{u}} = \bar{\mathbf{u}} + \alpha \frac{\gamma}{2L} \boldsymbol{t}. \tag{3.16}$$

For $\alpha = 1$ or -1, the material points follow the motion of outside or inside fluid respectively (see Baker *et al.*, 1982). Then velocities on either side of the interface are

$$\mathbf{u}_1 = \bar{\mathbf{u}} + \frac{\gamma}{2L}\boldsymbol{t} = \widetilde{\mathbf{u}} + (1-\alpha)\frac{\gamma}{2L}\boldsymbol{t}, \qquad \mathbf{u}_2 = \bar{\mathbf{u}} - \frac{\gamma}{2L}\boldsymbol{t} = \widetilde{\mathbf{u}} - (1+\alpha)\frac{\gamma}{2L}\boldsymbol{t}. \tag{3.17}$$

Evaluating the Euler equation on both sides gives

$$\frac{\partial \mathbf{u}_1}{\partial t} + (\mathbf{u}_1 \cdot \boldsymbol{\nabla})\mathbf{u}_1 = -\frac{1}{\rho_1}\boldsymbol{\nabla} p + \boldsymbol{g}, \tag{3.18}$$

$$\frac{\partial \mathbf{u}_2}{\partial t} + (\mathbf{u}_2 \cdot \boldsymbol{\nabla})\mathbf{u}_2 = -\frac{1}{\rho_2}\boldsymbol{\nabla} p + \boldsymbol{g}. \tag{3.19}$$

We follow the procedure in Baker *et al.* (1982) to eliminate pressure. We first subtract (3.19) from (3.18) and replace $\mathbf{u}_1$ and $\mathbf{u}_2$ in the advection term by $\widetilde{\mathbf{u}}$ from (3.17), giving

$$\frac{\mathrm{d}}{\mathrm{d}t}\left(\frac{\gamma}{L}\boldsymbol{t}\right) + \frac{\gamma}{L}\boldsymbol{t}\cdot\boldsymbol{\nabla}\widetilde{\mathbf{u}} - \alpha\frac{\gamma}{L}\boldsymbol{t}\cdot\boldsymbol{\nabla}\left(\frac{\gamma}{L}\boldsymbol{t}\right) = -\left(\frac{1}{\rho_1} - \frac{1}{\rho_2}\right)\boldsymbol{\nabla} p. \tag{3.20}$$

A material derivative following Lagrangian points is defined as

$$\frac{\mathrm{d}}{\mathrm{d}t} = \frac{\partial}{\partial t} + (\widetilde{\mathbf{u}} \cdot \boldsymbol{\nabla}). \tag{3.21}$$

Similarly, adding (3.18) and (3.19) together, and replacing $\mathbf{u}_1$ and $\mathbf{u}_2$ by $\widetilde{\mathbf{u}}$ and $\bar{\mathbf{u}}$ gives

$$2\frac{\mathrm{d}\bar{\mathbf{u}}}{\mathrm{d}t} - \alpha\frac{\gamma}{L}\boldsymbol{t}\cdot\boldsymbol{\nabla}\bar{\mathbf{u}} + \frac{\gamma}{2L}\boldsymbol{t}\cdot\boldsymbol{\nabla}\left(\frac{\gamma}{L}\boldsymbol{t}\right) = -\left(\frac{1}{\rho_2} + \frac{1}{\rho_1}\right)\boldsymbol{\nabla} p + 2\boldsymbol{g}. \tag{3.22}$$

The ratio between the coefficients of the pressure gradient in (3.20) and (3.22) is the Atwood number

$$A = \frac{\rho_1 - \rho_2}{\rho_1 + \rho_2}. \tag{3.23}$$

Eliminating the pressure yields

$$\frac{\mathrm{d}}{\mathrm{d}t}\left(\frac{\gamma}{L}\boldsymbol{t}\right)+\frac{\gamma}{L}\boldsymbol{t}\cdot\boldsymbol{\nabla}\widetilde{\mathbf{u}}-\alpha\frac{\gamma}{L}\boldsymbol{t}\cdot\boldsymbol{\nabla}\left(\frac{\gamma}{L}\boldsymbol{t}\right)=-2A\left[\frac{\mathrm{d}\bar{\mathbf{u}}}{\mathrm{d}t}-\frac{\alpha}{2}\frac{\gamma}{L}\boldsymbol{t}\cdot\boldsymbol{\nabla}\bar{\mathbf{u}}+\frac{\gamma}{4L}\boldsymbol{t}\cdot\boldsymbol{\nabla}\left(\frac{\gamma}{L}\boldsymbol{t}\right)-\boldsymbol{g}\right]. \tag{3.24}$$

To simplify the equation above, it can be shown that

$$\frac{1}{L}\frac{\mathrm{d}L}{\mathrm{d}t}=\boldsymbol{t}\cdot[(\boldsymbol{t}\cdot\boldsymbol{\nabla})\widetilde{\mathbf{u}}],\qquad \boldsymbol{t}\cdot\boldsymbol{\nabla}=\frac{1}{L}\frac{\partial}{\partial\xi}. \tag{3.25}$$

By projecting (3.24) on the tangential direction and using the Frenet–Serret formulas,

$$\frac{1}{L}\frac{\partial\boldsymbol{t}}{\partial\xi}=\kappa\boldsymbol{n},\quad \frac{1}{L}\frac{\partial\boldsymbol{n}}{\partial\xi}=-\kappa\boldsymbol{t}, \tag{3.26}$$

we obtain

$$\frac{\mathrm{d}\gamma}{\mathrm{d}t}-\frac{\alpha}{2}\frac{\partial}{\partial\xi}\left(\frac{\gamma}{L}\right)^2=-2AL\left[\boldsymbol{t}\cdot\frac{\mathrm{d}\bar{\mathbf{u}}}{\mathrm{d}t}-\frac{\alpha}{2}\frac{\gamma}{L^2}\frac{\partial\bar{\mathbf{u}}}{\partial\xi}\cdot\boldsymbol{t}+\frac{1}{8}\frac{1}{L}\frac{\partial}{\partial\xi}\left(\frac{\gamma}{L}\right)^2-\boldsymbol{t}\cdot\boldsymbol{g}\right]. \tag{3.27}$$

This equation agrees with equation (2.15) in Baker *et al.* (1982), although their problem is two-dimensional and they use complex variables and Bernoulli's equation. We can match each term to their two-dimensional formulation, so the vortex sheet dynamics are the same in two-dimensional and axisymmetric flows. In this chapter, we set $\alpha = 0$, i.e. we follow material points on the mean velocity so that $\widetilde{\mathbf{u}} = \bar{\mathbf{u}}$. We now drop the tildes and bars to obtain

$$\frac{\mathrm{d}\gamma}{\mathrm{d}t}=-2AL\left[\boldsymbol{t}\cdot\frac{\mathrm{d}\mathbf{u}}{\mathrm{d}t}+\frac{1}{8}\frac{1}{L}\frac{\partial}{\partial\xi}\left(\frac{\gamma}{L}\right)^2-\boldsymbol{t}\cdot\boldsymbol{g}\right]. \tag{3.28}$$

A similar equation can also be found in Shin *et al.* (2018), although gravity is omitted in their formulation.

The evolution equation for γ is coupled with (3.11) and (3.13). These equations can be transformed into a Fredholm integral equation of the second kind for $\mathrm{d}\gamma/\mathrm{d}t$. Using

(3.11), (3.13) and the definition of the unit tangent, we have

$$\begin{aligned}\boldsymbol{t}\cdot\frac{\mathrm{d}\mathbf{u}}{\mathrm{d}t} &= \boldsymbol{t}\cdot\frac{\mathrm{d}\mathbf{u}_p}{\mathrm{d}t}+\boldsymbol{t}\cdot\frac{\mathrm{d}\mathbf{u}_s}{\mathrm{d}t}\\ &= \frac{1}{R}\left(-\frac{1}{L}\frac{\partial R}{\partial\xi}\oint\frac{\mathrm{d}\gamma'}{\mathrm{d}t}\frac{\partial G}{\partial Z}\mathrm{d}\xi'+\frac{1}{L}\frac{\partial Z}{\partial\xi}\oint\frac{\mathrm{d}\gamma'}{\mathrm{d}t}\frac{\partial G}{\partial R}\mathrm{d}\xi'\right)+f(R,Z,\gamma,\mathbf{u}),\end{aligned}\tag{3.29}$$

where f is a function of R, Z, γ and $\mathbf{u}$, provided in Appendix A.1. The evolution equation of $\mathrm{d}\gamma/\mathrm{d}t$ is coupled with the Lagrangian advection equation in (3.5).

3.2.2 The Boussinesq limit

When the density difference across the interface is small but gravity remains important, we may assume $\rho_1 \approx \rho_2$ in all terms except for gravity. This is the Boussinesq approximation. The evolution equation for γ in the Boussinesq limit is

$$\frac{\mathrm{d}\gamma}{\mathrm{d}t} = 2AL\boldsymbol{t}\cdot\boldsymbol{g} = \left(1-\frac{\rho_2}{\bar{\rho}}\right)L\boldsymbol{t}\cdot\boldsymbol{g},\tag{3.30}$$

where $\bar{\rho}=(\rho_1+\rho_2)/2$ (other definitions are possible). In the Boussinesq approximation, the acceleration term $\boldsymbol{t}\cdot(\mathrm{d}\mathbf{u}/\mathrm{d}t)$ vanishes in the vortex sheet equation. This gives an advantage in solving the integro-differential equations numerically, since $\mathrm{d}\gamma/\mathrm{d}t$ is no longer determined by a Fredholm integral function and can be integrated by straightforward time-stepping.

3.2.3 Surface tension

When a vortex ring consists of air or vapor inside a liquid, the pressure is discontinuous across the interface. This dynamical jump is balanced by surface tension T_s,

$$p_2-p_1=\kappa T_s,\tag{3.31}$$

where κ is the curvature of the interface. Typically T_s is a constant. We can replace the pressure in (3.18) and (3.19) by p_1 and $p_1 + \kappa T_s$, respectively, then carry out the same calculation as in § 2.1. We obtain

$$\frac{\mathrm{d}\gamma}{\mathrm{d}t} = -2AL\left[\boldsymbol{t}\cdot\frac{\mathrm{d}\mathbf{u}}{\mathrm{d}t} + \frac{1}{8}\frac{1}{L}\frac{\partial}{\partial\xi}\left(\frac{\gamma}{L}\right)^2 - \boldsymbol{t}\cdot\boldsymbol{g}\right] + \frac{T_s}{\bar{\rho}}\frac{\partial\kappa}{\partial\xi}. \tag{3.32}$$

The rate of change of the vortex sheet strength contains a contribution proportional to the gradient of curvature along the interface when surface tension is present.

3.2.4 Dimensionless parameters

There are four dimensionless parameters for this problem. One is the aspect ratio of the ring, $S = a_0/\mathcal{R}_0$, where a_0 is the initial radius of vorticity core and $\mathcal{R}_0$ is the initial radius of vortex ring. Another dimensionless number can be taken as the Froude number

$$Fr = \frac{U_c}{\sqrt{ga_0}}, \tag{3.33}$$

where U_c is a velocity scale. We set $U_c = a_0^2\Omega$, which characterizes the translation of a homogeneous ring. The time scale is $a_0/U_c = 1/(a_0\Omega)$. The vortex sheet strength γ can be scaled by a_0U_c while ξ has no dimension. A dimensionless form of (3.32) is then given by

$$\frac{\mathrm{d}\gamma}{\mathrm{d}t} = -2AL\left[\boldsymbol{t}\cdot\frac{\mathrm{d}\mathbf{u}}{\mathrm{d}t} + \frac{1}{8}\frac{1}{L}\frac{\partial}{\partial\xi}\left(\frac{\gamma}{L}\right)^2 + \frac{1}{Fr^2}\boldsymbol{t}\cdot\hat{\mathbf{z}}\right] + \frac{1}{We}\frac{\partial\kappa}{\partial\xi}, \tag{3.34}$$

where gravity $\boldsymbol{g} = -g\hat{\mathbf{z}}$. The last parameter in the dimensionless equation is the Weber number,

$$We = \frac{\bar{\rho}U_c^2a_0}{T_s} \tag{3.35}$$

A special case is $\Omega = 0$, when there is no continuous vorticity inside the vortex. We then choose the velocity scale using $U_c = \sqrt{ga_0}$, giving $Fr = 1$.

We call the third term on the right-hand side of (3.34) the buoyancy or source term, since vorticity is created by baroclinic generation. The second term on the right-hand side is the quadratic or nonlinear term. The first term is the dynamic-coupling term, in which the dynamics of the contour is coupled to the evolution of the sheet strength. The last term corresponds to surface tension.

3.3 Numerical method

Before we start our discussion of the numerical scheme, it is worth surveying the literature to identify similar problems that have been investigated. In table 3.1 we list some references with calculations of vortex sheet evolution. The vortex sheet strength does not evolve when density differences, body forces and surface tension all vanish. Once density differences are introduced, the dynamic-coupled and quadratic terms in (3.34) are nonzero. Body forces behave like a source in (3.34). The self-induced velocity of the vortex sheet is calculated using the Biot–Savart law. If a vortex sheet is a closed contour enclosing vorticity, the contribution from vortex patch (3.11) must be added.

Our numerical scheme consists of four main parts: an interpolation method to approximate the location of the contour and compute spatial derivatives, quadrature to evaluate contour integrals, an integral equation to obtain the vortex sheet strength and a time-stepping method to evolve the contour. The contour is discretised using a set of Lagrangian points, i.e. material points, $\boldsymbol{X}_n$ in the r-z plane with $n = 1, 2, \ldots, N$. The initial contour is given by

$$R(\xi, 0) = \mathcal{R}_0 + a_0 \cos\xi, \;\; Z(\xi, 0) = a_0 \sin\xi \tag{3.36}$$

for $\xi \in [0, 2\pi)$; $\mathcal{R}_0$ is the initial radius of the ring and a_0 is the radius of its core. For small ring sizes, this is almost the steadily propagating solution of Norbury (1973). We

Table 3.1: Previous studies on vortex sheet evolution compared to present study.

	Domain	Density difference	Body force	Surface tension	Vortex patch
Baker *et al.* (1982)	2D	yes	gravity	no	no
Krasny (1986*a*)	2D	no	no	no	no
Baker *et al.* (1993)	2D	yes	gravity	no	no
Hou, Lowengrub & Shelley (1994)	2D	yes	gravity	yes	no
Baker & Nachbin (1998)	2D	no	no	yes	no
Baker & Xie (2011)	2D	yes	gravity	no	no
Shin *et al.* (2018)	2D	yes	no	yes	no
Pozrikidis (1986)	axisymm	no	no	no	yes
Shariff *et al.* (1989)	axisymm	no	no	no	yes
Nitsche & Krasny (1994)	axisymm	no	no	no	no
Nitsche (2001)	axisymm	no	no	no	no
Hattori & Moffatt (2006)	axisymm	no	magnetic	no	no
Llewellyn Smith & Hattori (2012)	axisymm	no	magnetic	no	yes
Present work	axisymm	yes	gravity	no	yes

set $\mathcal{R}_0 = 1$ in all calculations. These Lagrangian points are evolved using (3.5),

$$\frac{\mathrm{d}\boldsymbol{X}_n}{\mathrm{d}t} = \mathbf{u}_n, \tag{3.37}$$

where $\mathbf{u}_n$ is $\mathbf{u}$ evaluated numerically on $\boldsymbol{X}_n$.

3.3.1 Interpolation and spatial differentiation

Since the contour is a closed curve, it is natural to use a Fourier series to interpolate between points,

$$\boldsymbol{R}(\xi) = \sum_{k=-N/2}^{N/2-1} \hat{\boldsymbol{X}}_k \, \mathrm{e}^{\mathrm{i}k\xi}, \tag{3.38}$$

where the $\hat{\boldsymbol{X}}_k$ are the Fourier coefficients of the Lagrangian points' locations. Here $k = -N/2,\ldots, -1, 0, 1,\ldots, N/2-1$ are the wavenumbers. The parameter ξ is equally spaced in $[0, 2\pi)$. The mth derivative along the contour is computed from the Fourier series

$$\boldsymbol{R}^{(m)}(\xi) = \sum_{k=-N/2}^{N/2-1} (\mathrm{i}k)^m \hat{\boldsymbol{X}}_k \, \mathrm{e}^{\mathrm{i}k\xi}. \tag{3.39}$$

The spatial distribution of the vortex sheet strength γ_n is also interpolated using Fourier series. A Fourier filter is used to cut off the highest one-third of the spectrum to mitigate the the aliasing error from the quadratic term.

$$\hat{f}(k) = \begin{cases} 1, & |k| \le N/3 \\ 0, & |k| > N/3, \end{cases} \tag{3.40}$$

The aliasing error from the quadratic term can also be mitigated. A filter proposed by Krasny (1986*b*) is also implemented to suppress the growth of noise due to round-off error using a threshold of $O(10^{-12})$. At every time step, filters are applied whenever the time

derivatives, $\mathbf{u}$ and $\mathrm{d}\gamma/\mathrm{d}t$, are obtained. Krasny's filter is applied first, then (3.40) right after it. Once the time derivatives are filtered, (R, Z) and γ are marched forward by one time step and the same filtering process applied to the new (R, Z) and γ.

3.3.2 Quadrature rule

The velocity $\mathbf{u}$ for each material point is the sum of (3.11) and (3.13), in which the contour integrals are computed numerically. The quadrature can be done using the trapezoidal rule which gives spectral convergence for periodic functions (Trefethen & Weideman, 2014). However the functions G and H are singular as $(r', z') \to (r, z)$, because the complete elliptic integral of the first kind, $K(k)$, is unbounded when $k \to 1$. There are several ways to remove the singularity. One way is the vortex blob method (see Krasny, 1986*a*): a small parameter ϵ is introduced into the denominator in (3.10), giving

$$k^2 = \frac{4rr'}{(r + r')^2 + (z - z')^2 + \epsilon^2}. \tag{3.41}$$

The idea is essentially the same as the Moore–Rosenhead method (see Saffman, 1992, p. 213) to desingularise the Biot–Savart integral for vortex filaments, in which a small parameter ϵ is added into denominator to avoid a division by zero. It acts to remove scales smaller than ϵ. The appropriate value of ϵ is discussed below.

A formally exact method is to subtract the singular part of the integrand. The regularised integral is then computed numerically using the trapezoidal rule. The asymptotic behavior of the singularity of (3.9) is (Pozrikidis, 1986)

$$G_s \sim \frac{r'}{2\pi} \ln \frac{4}{\sqrt{1 - k^2}}. \tag{3.42}$$

Shariff *et al.* (1989); Nitsche & Krasny (1994); Nitsche (2001); Hattori & Moffatt (2006);

Llewellyn Smith & Hattori (2012) use this method to remove the singularity. A local series is then integrated term by term over segments adjacent to the singular point. Another method used in two dimensions (Baker *et al.*, 1993; Hou *et al.*, 1994; Baker & Xie, 2011; Shin *et al.*, 2018) is the trapezoidal rule based on alternative/mid points to avoid the singular point. This idea is not pursued here (but see § 3.5).

While the series expansion method should formally yield higher accuracy, it suffers from two problems. First, the function takes a different form on the segment including the singularity which may reduce the accuracy of the trapezoidal rule. Second, it is difficult to implement when solving the dynamic-coupled term in the vortex sheet equation, since it requires a local approximation to $\mathrm{d}\gamma/\mathrm{d}t$, which is unknown. As a result, the blob method appears to be the most natural regularisation and is the one that was used. Nevertheless we can examine the difference between the two. The contours in figure 3.2(a) show very little difference using $\epsilon = 0.01$. Some differences can be noticed near the roll-up at $t = 0.8$, but the bulk motions of the two are almost the same. That serves our purpose well enough to model the motion of a buoyant vortex ring, even though the small scales are not perfectly resolved. We also test different value of ϵ. In figure 3.2(b), the profiles almost overlap for $\epsilon \leq 0.01$, and the maximum error of velocity profile is $O(10^{-6})$. The volume is a conserved quantity and the change in volume is 0.2% during $t = 0$–0.84 with $\epsilon = 0.01$. With $\epsilon = 0.05$ the computation lasts for a longer time $t = 0$–1.09 and the change in volume is 0.6%. In the present study, we used $\epsilon = 0.05$ in order to achieve longer integration in time.

The convergence test for $\mathbf{u}$ with respect to N uses the following approach: first we calculate the velocity $\mathbf{u}^{(N/2)}$ with grid resolution $N/2$, then we double the resolution to N by adding one new point between every two existing points. The velocity is then calculated again as $\mathbf{u}^{(N)}$. We compute the change in velocity at the original points, then take its norm as

$$\epsilon_N = ||\mathbf{u}^{(N)} - \mathbf{u}^{(N/2)}||. \tag{3.43}$$

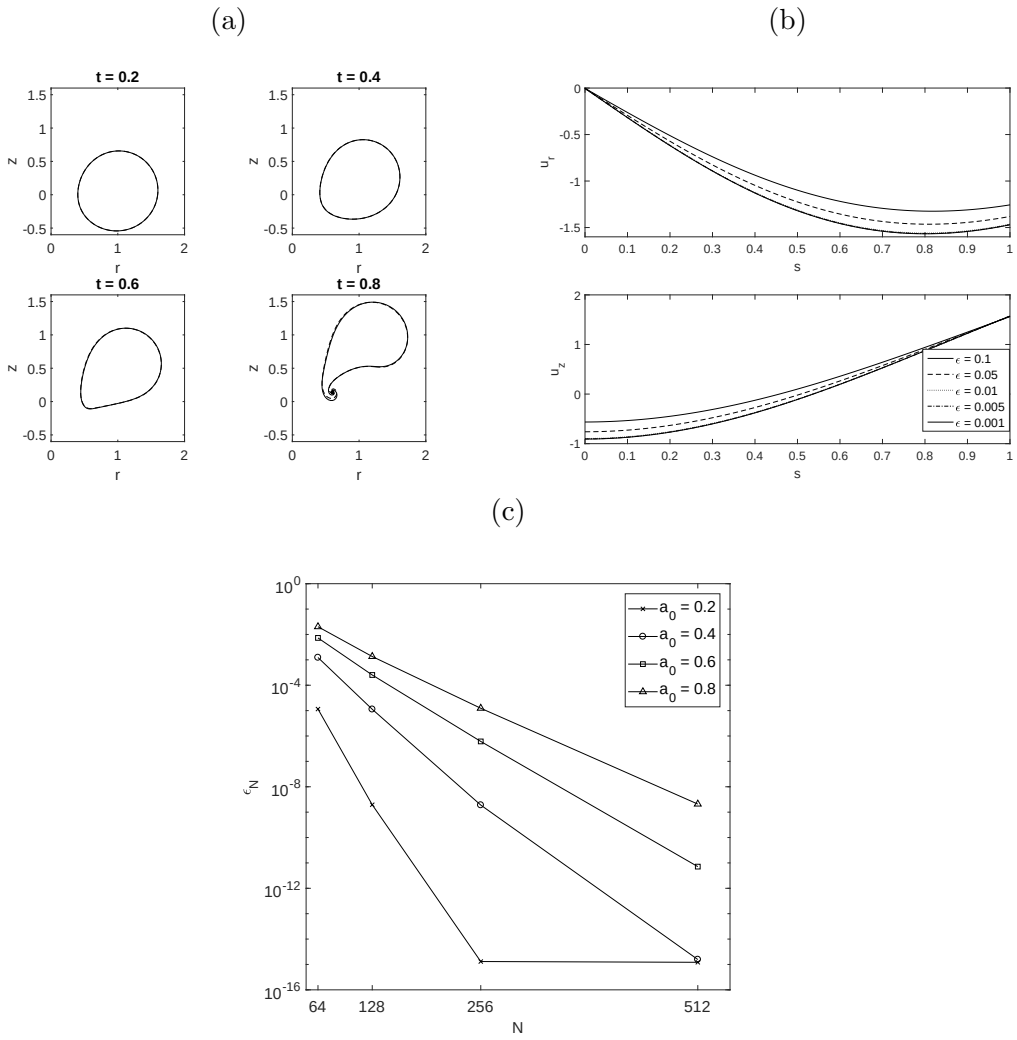

Figure 3.2: (a) Comparison of the blob method (solid line) and the series expansion method (dashed line) using velocity $\mathbf{u}_s$ only. $\epsilon = 0.01$; (b) a close look of velocity profile for various ϵ; (c) convergence test with different core size a_0.

We find $\epsilon_N \to 0$ when $N \to \infty$, where ϵ_N is a function of N and a_0 plotted in figure 3.2(c). Different initial vortex core radii a_0 require different values of N. If we set $\epsilon_N = 10^{-4}$ as our desired accuracy, $a_0 = 0.2$ satisfies this criterion with $N = 64$, while $a_0 = 0.8$ the required resolution rises to $N = 256$. Therefore, we choose $N = 64$ for $a_0 = 0.2$ and $N = 256$ for $a_0 = 0.8$, $N = 128$ for $a_0 = 0.4$ and $N = 256$ for $a_0 = 0.6$ to keep ϵ_N below 10^{-4}. For higher accuracy, e.g. $\epsilon_N < 10^{-8}$, $a_0 = 0.2$ needs resolution $N = 128$ and $a_0 = 0.8$ needs at least $N = 512$.

3.3.3 Integral equation

To solve for γ, the rate of change of γ is calculated by solving the integral equation given by combining (3.29) and (3.32):

$$\frac{\mathrm{d}\gamma}{\mathrm{d}t} = -2A\mathcal{L}\frac{\mathrm{d}\gamma}{\mathrm{d}t} + \mathcal{F}, \tag{3.44}$$

where the linear integral operator is

$$\mathcal{L}g = \frac{1}{R}\left(-\frac{\partial R}{\partial \xi}\oint \frac{\partial G}{\partial Z} g \,\mathrm{d}\xi' + \frac{\partial Z}{\partial \xi}\oint \frac{\partial G}{\partial R} g \,\mathrm{d}\xi'\right)$$

and $\mathcal{F}$ contains all the terms on the right-hand side of (3.32) except the terms in $\mathrm{d}\gamma/\mathrm{d}t$. The Green function G is regularised by the blob method. The integral operator $\mathcal{L}$ is discretised using the trapezoidal rule and $\mathcal{F}_i$ is $\mathcal{F}$ evaluated at $\boldsymbol{X}_n$. Then (3.44) becomes

$$\left.\frac{\mathrm{d}\gamma}{\mathrm{d}t}\right|_i = -2A\sum_j \mathcal{L}_{ij}\left.\frac{\mathrm{d}\gamma}{\mathrm{d}t}\right|_j + \mathcal{F}_i. \tag{3.45}$$

The discretised equation can be transformed into the linear system

$$(\delta_{ij} + 2A\mathcal{L}_{ij})\left.\frac{\mathrm{d}\gamma}{\mathrm{d}t}\right|_i = \mathcal{F}_i. \tag{3.46}$$

The matrix is diagonally dominant and (3.46) can be solved by successive over-relaxation (SOR) efficiently.

3.3.4 Time-stepping

Finally, $\boldsymbol{X}$ and γ are advanced in time using the classic four-stage Runge–Kutta scheme

$$\frac{\mathrm{d}\boldsymbol{X}}{\mathrm{d}t} = \frac{1}{6}\left[\mathbf{u}_{(1)} + 2\mathbf{u}_{(2)} + 2\mathbf{u}_{(3)} + \mathbf{u}_{(4)}\right], \tag{3.47}$$

where the $\mathbf{u}_{(j)}$ are intermediate values (e.g. see Iserles, 2009, § 3.2). The time step Δt is fixed at 0.001 in our calculations. The initial value of γ is zero. The two filters introduced earlier are also applied to intermediate values.

3.4 Numerical results

We first discuss the γ-equation and its solutions. We show the possible emergence of curvature singularities that limit the length of numerical calculations. Then we present numerical results and discuss their dependence on the dimensionless numbers A and Fr. Finally we quantify the motion of the ring using integral quantities.

3.4.1 Boussinesq vs non-Boussinesq cases

The evolution equation for γ, (3.34), is central when using axisymmetric contour dynamics to calculate the motion of buoyant vortex rings. The first two terms on the right-hand side of (3.34) are multiplied by the Atwood number A and represent the contribution from density difference alone. The third term with gravity has a prefactor A/Fr^2 which measures the strength of buoyancy. We exclude surface tension for now, so that $We \to \infty$. When the density difference is small but gravity is strong, we have $A \to 0$ but $A/Fr \gtrsim 1$.

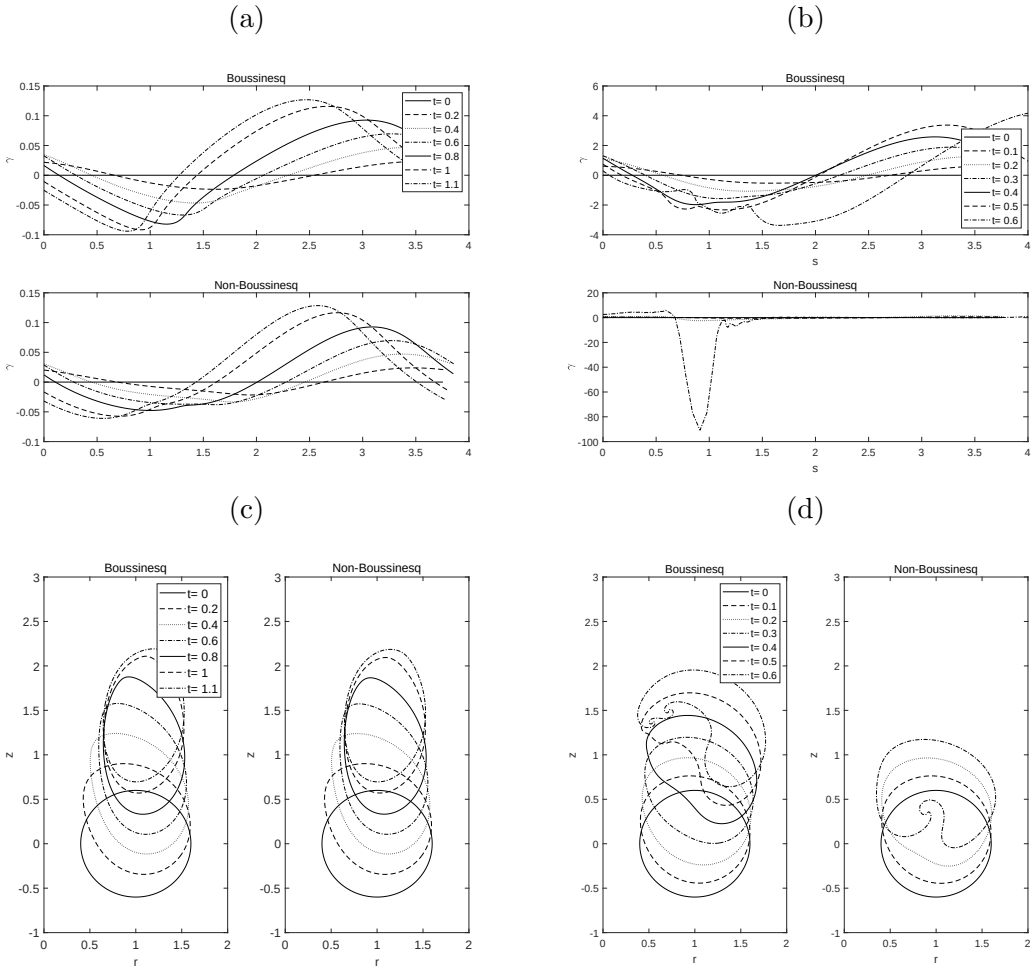

Figure 3.3: (a, b) The vortex sheet strength γ along the boundary and (c, d) the snapshots of contours. The Atwood numbers are $A = 0.01$, 0.5 for (a, c) and (b, d), respectively. All cases have $Fr = 1$ and $We = \infty$. For the Boussinesq case, γ is obtained using (3.30), while (3.28) is used for non-Boussinesq calculations.

The problem can then be approximated by the Boussinesq formulation. For small Atwood number, e.g. $A = 0.01$, the vortex sheets evolved using (3.28) and (3.30) are almost identical (figure 3.3a). Profiles computed from both γ equations are very similar, as shown in figure 3.3(c). Since A is small, the first two terms in the non-Boussinesq formulation are negligible.

We increase the Atwood number to 0.5. The solutions for γ are show in figure 3.3(b) and the corresponding contours in figure 3.3(d). The Boussinesq and non-Boussinesq cases differ when A is sufficiently large. The contour in the Boussinesq case have evolved into two roll ups when $t = 0.6$. The non-Boussinesq case is similar to the Boussinesq calculation before $t = 0.2$, but then the contour starts to deform more drastically than the Boussinesq case when $t > 0.2$. The non-Boussinesq calculation stops around $t = 0.3$ when the contour develops a sharp tip near $(0.92, 0.36)$ in figure 3.3(d) at which point the Fourier spectrum has saturated (see below), but before any roll-ups appear. The roll-ups are associated with the formation of finite-time singularity in curvature which has been found in many other studies on vortex sheet calculations.

3.4.2 Singularities and vortex sheet dynamics for moderate A

We plot the curvature of vortex sheets in the non-Boussinesq case for $A = 0.3$, 0.5 in figure 3.4. The formation of a spike in each case is apparent. This could indicate a finite-time curvature singularity as seen in the literature. The formation of curvature singularities of a vortex sheet was studied by Moore (1979). These singularities can be observed physically when singularities in the complex plane reach the real axis. Meiron, Baker & Orszag (1982) and Krasny (1986b) numerically confirmed Moore's asymptotic result. Cowley, Baker & Tanveer (1999) showed how singularities move in the complex plane and reach the real axis in finite time. Krasny (1986b) studied the formation of these singularities using the point–vortex approach, while Krasny (1986b) and Cowley

et al. (1999) identified the singularity as having a $\frac{3}{2}$-power form. Baker *et al.* (1993) applied a vortex sheet model to the Rayleigh–Taylor instability problem, and showed that singularities do not reach the real axis in finite time if one layer of fluid has zero density (i.e. $A = 1$). These investigations considered two-dimensional periodic problems. The present calculation is axisymmetric, but the same kind of curvature singularity is possible. The nature of these singularities is worthy of a more detailed study, but that lies beyond the scope of this work as our intention is to calculate the motion of buoyant vortex rings. The reason we discuss singularities here is to point out that such a spike will cause a numerical blowup in our calculations. Even though our blob method may not allow actual singularity formation, the resulting growth in curvature appears strong enough to terminate the simulation for the values of ϵ required to obtain good overall numerical accuracy.

The Fourier spectrum of $\mathrm{d}\gamma/\mathrm{d}t$ in figure 3.5 shows the growth of higher modes. The spectrum still fills up when a filter is applied. The calculation blows up when the highest filtered mode, $|k| = N/3$, reaches the order of magnitude of the $|k| = 1$ mode. For the Boussinesq case, the highest mode grows but never exceeds the magnitude of mode $|k| = 1$ during the calculation. The difference between the vortex sheet evolution equations for the Boussinesq and non-Boussinesq cases comes from the first two terms in (3.28), which we now examine in detail. The behaviour of $\mathrm{d}\gamma/\mathrm{d}t$ is investigated by examining the evolution of each term in (3.28), as shown in figure 3.6. At $t = 0.1$, $\mathrm{d}\gamma/\mathrm{d}t$ is dominated by the source term (III), i.e. buoyancy, along with the dynamic-coupled term (I). The quadratic term (II) is small compared to the first two and negligible. As the calculation proceeds to $t = 0.2$, the dynamic-coupled term dominates $\mathrm{d}\gamma/\mathrm{d}t$ while the source terms become less important. The quadratic term became of the same order as the source term, and this is when the dynamics becomes more complicated. The contour in figure 3.3(d) starts to deviate from its initially circular shape. The sharp drop of vortex sheet strength profile

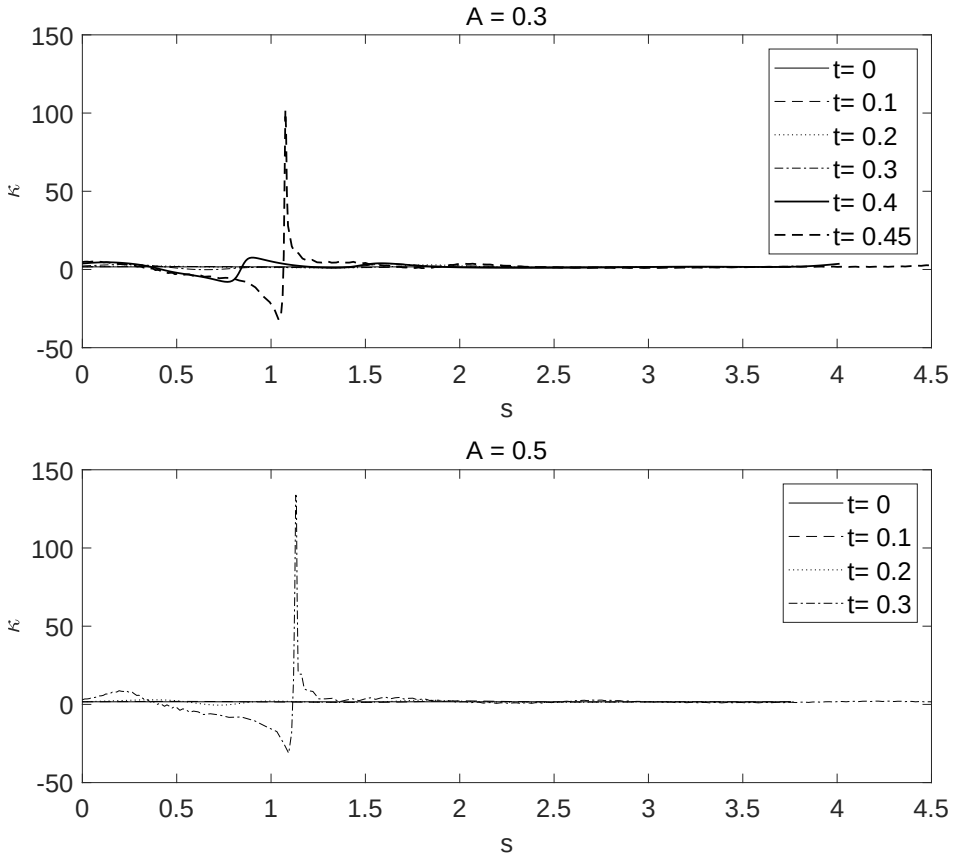

Figure 3.4: Curvature along the contour for $A = 0.3$ and 0.5. The height of the spike increases as A increases.

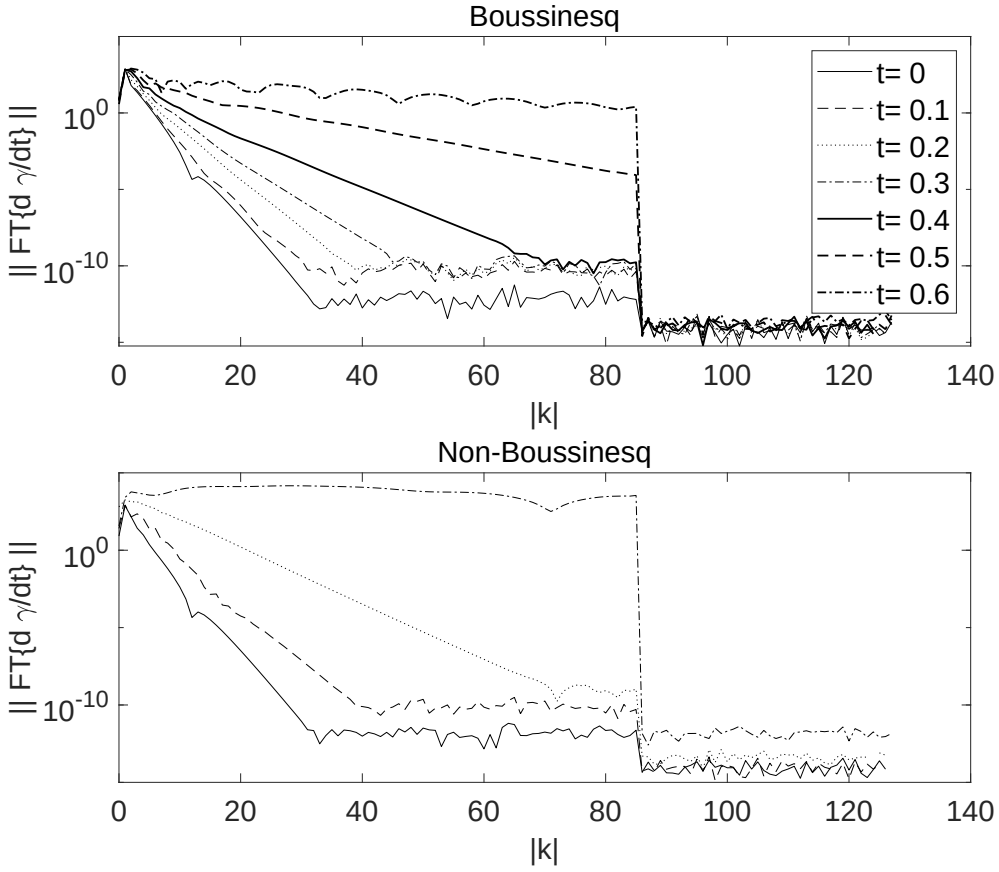

Figure 3.5: Fourier spectra of $\mathrm{d}\gamma/\mathrm{d}t$ for Boussinesq and non-Boussinesq calculations for $A = 0.5$, $Fr = 1$ and $We = \infty$, shown in figure 3.3(b) and (d). The calculations were stopped when the Fourier coefficient of highest mode becomes $\simeq O(1)$.

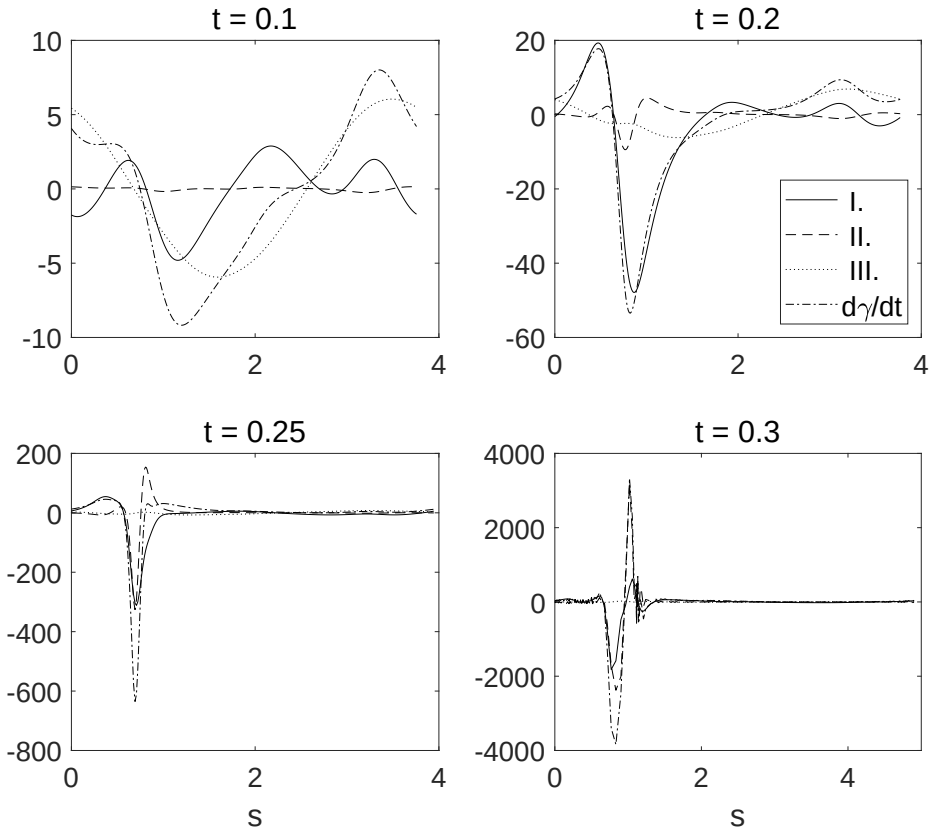

Figure 3.6: Terms in (3.28). Right-hand side terms are I: dynamic-coupled term, i.e. f in (3.29); II: quadratic term; III: buoyancy. $A = 0.5$ and $Fr = 1$. Their sum is $\mathrm{d}\gamma/\mathrm{d}t$.

near $s = 0.83$ indicates that a roll-up is beginning. In the plots at later times $t = 0.25$ and 0.3, the ratio of the source term diminished. At this moment, the entire dynamics is dominated by the sharp spike in the γ-profile, which is a combined contribution from the dynamic-couple and the quadratic terms. Note that while this is happening, the matrix on the left-hand side of the linear system (3.46) remains diagonally dominated, so that the linear system is well-conditioned.

3.4.3 Non-Boussinesq vortex rings

We first fix the aspect ratio at $S = 0.6$ for the following calculation. Our aim is to investigate how buoyancy alters the motion of the rings. Buoyancy is a result of combining

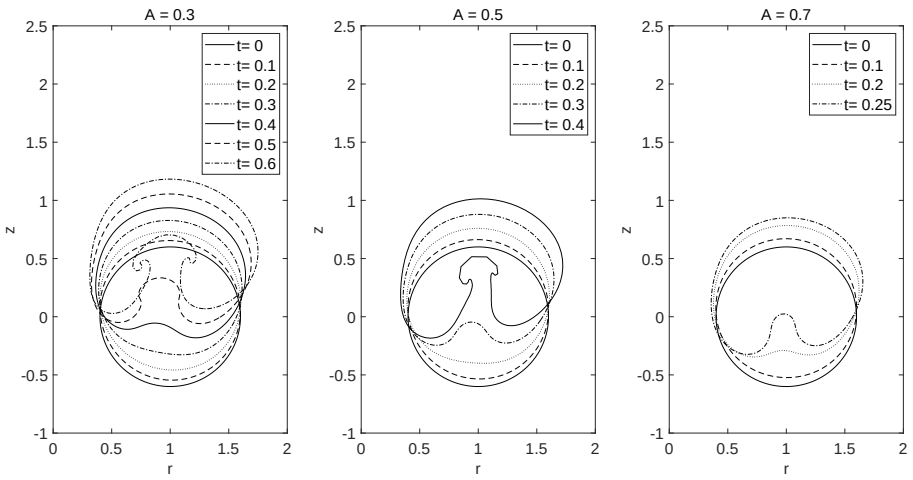

Figure 3.7: Evolution of contour with different Atwood numbers $A = 0.3,\ 0.5,\ 0.7$, from left to right respectively. Other parameters are kept constant: $S = 0.6$, $Fr = 0.3$ and $We = \infty$.

density difference and gravity, and can be measured by A/Fr^2. We examine the terms on the right-hand side of (3.34). If A is small and Fr is large, buoyancy is negligible and $\mathrm{d}\gamma/\mathrm{d}t \approx 0$, so the vortex ring retains its classic solution. If Fr decreases such that A/Fr^2 equals or greater than $O(1)$, the buoyant vortex ring is in the Boussinesq limit. If A increases significantly, every term in the γ-equation become important and the vortex ring evolves in the non-Boussinesq regime.

The evolution of contours for cases with Atwood numbers, $A = 0.3,\ 0.5,\ 0.7$, is shown in figure 3.7. In each case, we observe that contours were deformed from their initially circular shape. The lower half of the contour bent inward and the ambient fluid squeezed into the vortical core from below. Similar behaviour was obtained in Lundgren & Mansour (1991) for a spherical vortex bubble. As the contour for $A = 0.3$ and 0.5 evolves, two counter-rotating roll-ups develop. These are due to the dot product of local tangent and gravity, i.e. $\boldsymbol{t} \cdot \hat{\mathbf{z}}$, in the buoyancy term. The dot product is negative when the local tangent of the contour points down and positive when it points up. As the result, the source term has different signs on the left and right half of the contour. Once the vortex

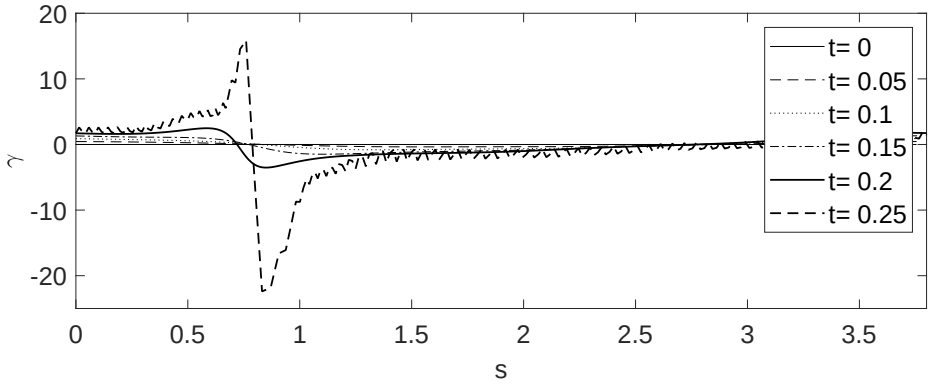

Figure 3.8: Vortex sheet strength γ evolving into a shock-like profile. $A = 0.7$, $Fr = 0.3$ and $We = \infty$.

sheet is created by the baroclinic torque, it rotates in opposite directions. In the $A = 0.3$ and 0.5 cases, a mushroom-like structure can be seen when the contour evolves for a longer time. We did not include surface tension in the calculations here, but we anticipate that surface tension will suppress the development of roll-up. The mushroom structure did not appear for the $A = 0.7$ case, when the calculation stopped earlier than the former two cases, before any roll-up will appear. Since roll-up did not happen, the failure of the calculation does not seem to be related to the curvature singularities we discussed above. We look into the vortex sheet strength profile for $A = 0.7$ by plotting γ along the contour. We found that as the vortex sheet strength evolved, a shock-like discontinuity developed in its profile, as shown in figure 3.8. This originates from the quadratic term in the vortex sheet equation. For large enough Atwood number, the evolution equation for γ resembles the inviscid Burgers equation, which is known to allow shocks. The whole calculation then broke down once the discontinuity appeared in γ and subsequently spread to other numerical quantities.

Calculations were carried out in a wider parameter space for A and Fr, as shown in figure 3.9. The dotted curves are lines of constant A/Fr^2 that represent the strength of buoyancy. The Weber number is infinite. The contours are shown at the moment when

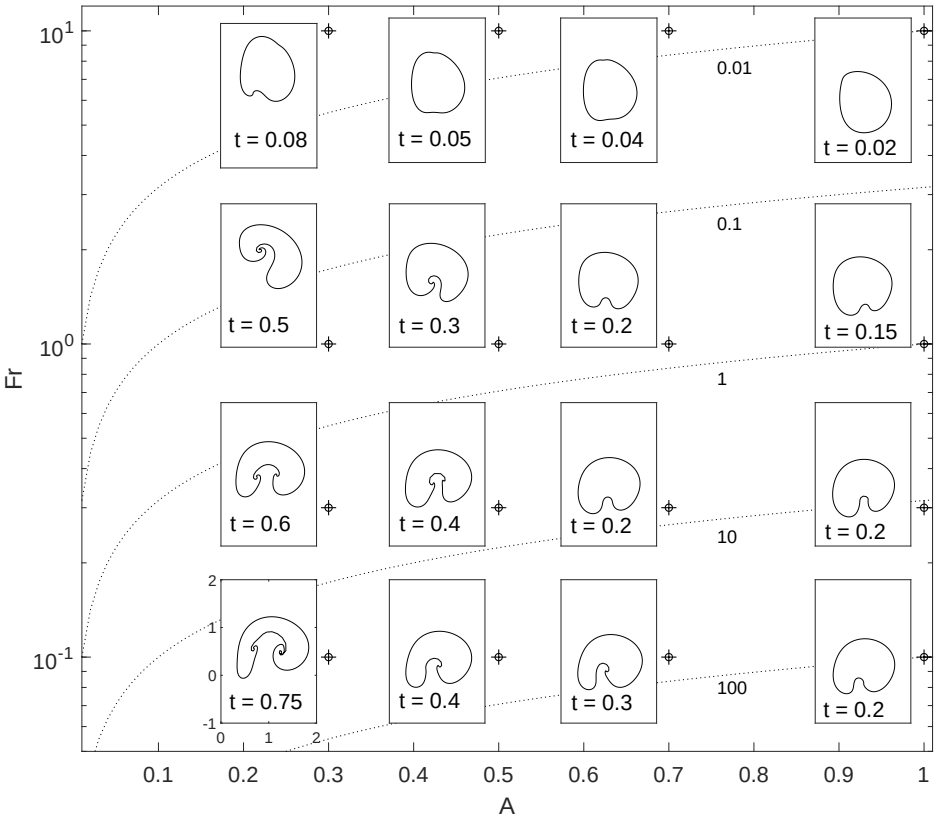

Figure 3.9: Contour at the time indicated in each inset for a range of (A, Fr). The dotted curves have constant A/Fr^2 values of 0.01, 0.1, 1, 10, 100; $S = 0.6$ and $We = \infty$ are kept constant.

the magnitude of highest filtered mode $|k| = N/3$ is in the same order to the magnitude of mode $|k| = 1$ so that failure of the calculations is imminent. The bottom left corner is where A and Fr are both small, and hence it is the Boussinesq limit. The cases with $A = 1$ on the right have more limited calculation time, since the nonlinear term $\partial\gamma^2/\partial\xi$ becomes important and leads to a shock-like discontinuity in γ as discussed above. On the top of the chart, the computations are also very limited. In this regime, the vortex sheet equation is dominated by the dynamic-coupled and the quadratic terms while buoyancy is weak. Our numerical scheme is not very stable in this regime. In general, contours on the bottom-left portion of the domain are more manageable for numerical calculation.

The aspect ratio of the ring S was then varied from 0.6 to 0.2, 0.1 and 0.05. As shown in figure 3.10, the contour is still bending inward from its bottom, but its inner half (closer to the axis of symmetry) is lifted up compared to the $S = 0.6$ case. The mushroom-like structure is not observed during the calculation. Calculations stopped because a shock-like profile of γ formed. When the aspect ratio dropped to 0.05, the dynamic became different from those with larger S. The contour maintained its near-circular shape until $t = 0.4$, then it started to deform into an elliptic shape. Then it paused its upward motion and stayed near $(1.08, 0.11)$ during $t = 0.4$–0.5. From $t = 0.7$ it resumed its upward motion, and a small tip appeared on the top of the contour before the calculation failed. In figure 3.11, we plot the centroid (defined in § 4.4) for $S = 0.05$. Initially Z_c increases linearly and then is nearly constant around $t = 0.4$–0.5, before increasing again. Before the contour deviated from its circular shape, the initial vertical velocity can be estimated using the thin ring model from Chang & Llewellyn Smith (2018):

$$\frac{\partial Z_c}{\partial t} = \frac{\Gamma}{4\pi\mathcal{R}}\left(\ln\frac{8}{S} - \frac{1}{2} + \frac{1}{4}\frac{\rho_2}{\rho_1}\right),$$

where Γ is the circulation and the expansion rate of the ring can be estimated by

$$\frac{\partial R_c}{\partial t} = \left(1 - \frac{\rho_2}{\rho_1}\right) \frac{\pi a^2 g}{\Gamma},$$

which are plotted by dashed lines in figure 3.11 for $S = 0.05$. Then R_c expanded rapidly before $t = 0.4$, then diminished a little before resuming its expansion. While the current calculations eventually fail, for a thin ring Pedley (1968) has shown that the radius of a buoyant ring increases as $\sqrt{t}$ when $t \to \infty$.

The vertical acceleration can be calculated by differentiating $\partial Z_c/\partial t$:

$$\begin{aligned} \frac{\partial^2 Z_c}{\partial t^2} &= -\frac{\Gamma}{4\pi\mathcal{R}^2}\left(\ln\frac{8}{S} - \frac{1}{2} + \frac{1}{4}\frac{\rho_2}{\rho_1}\right)\frac{\partial \mathcal{R}}{\partial t} - \frac{\Gamma}{4\pi\mathcal{R}}\frac{1}{S}\frac{\partial S}{\partial t}, \\ &= \frac{a^2 g}{4\mathcal{R}^2}\left(1 - \frac{\rho_2}{\rho_1}\right)\left(-\ln\frac{8}{S} + 2 - \frac{1}{4}\frac{\rho_2}{\rho_1}\right), \end{aligned} \tag{3.48}$$

where the continuity equation gives $-2S^{-1}\partial S/\partial t = 3\mathcal{R}^{-1}\partial\mathcal{R}/\partial t$. Scaling (3.48) by U_c^2/a_0, the acceleration of a thin ring due to buoyancy is

$$\left(1 - \frac{\rho_2}{\rho_1}\right)\frac{S^2}{4Fr^2}\left(-\ln\frac{8}{S} + 2 - \frac{1}{4}\frac{\rho_2}{\rho_1}\right).$$

3.4.4 Centroid and circulation

We now present some quantitative results of contour evolution. Two integral quantities are used to quantify vortex motion and dynamics: the centroid and the circulation. The centroid of the vortical core is calculated using the formula (Pozrikidis, 1986):

$$R_c^2 = \frac{\oint R^3 Z \boldsymbol{t}\cdot\mathbf{r}\,\mathrm{d}s}{\oint RZ\boldsymbol{t}\cdot\mathbf{r}\,\mathrm{d}s}, \quad Z_c = \frac{\oint R^3 Z^2 \boldsymbol{t}\cdot\mathbf{r}\,\mathrm{d}s}{2\oint R^3 Z\boldsymbol{t}\cdot\mathbf{r}\,\mathrm{d}s}. \tag{3.49}$$

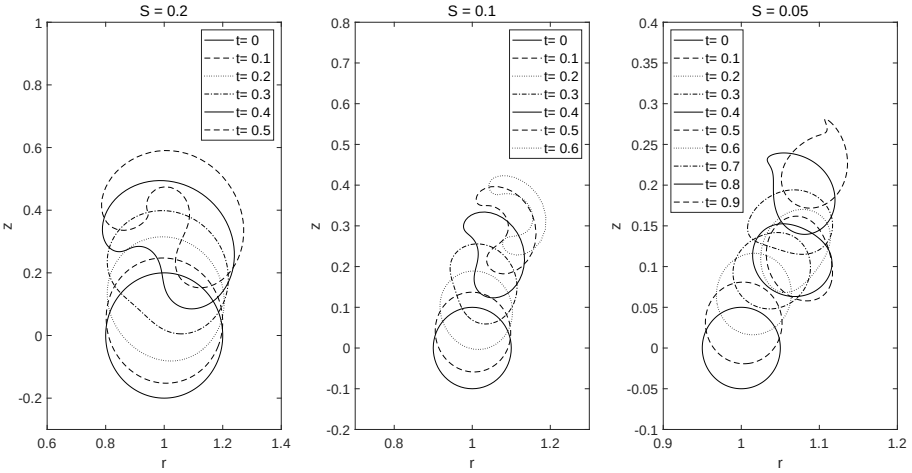

Figure 3.10: Evolution of contour with aspect ratio $S = 0.2,\ 0.1,\ 0.05$, respectively. Other parameters are kept constant: $A = 0.3$, $Fr = 0.3$ and $We = \infty$.

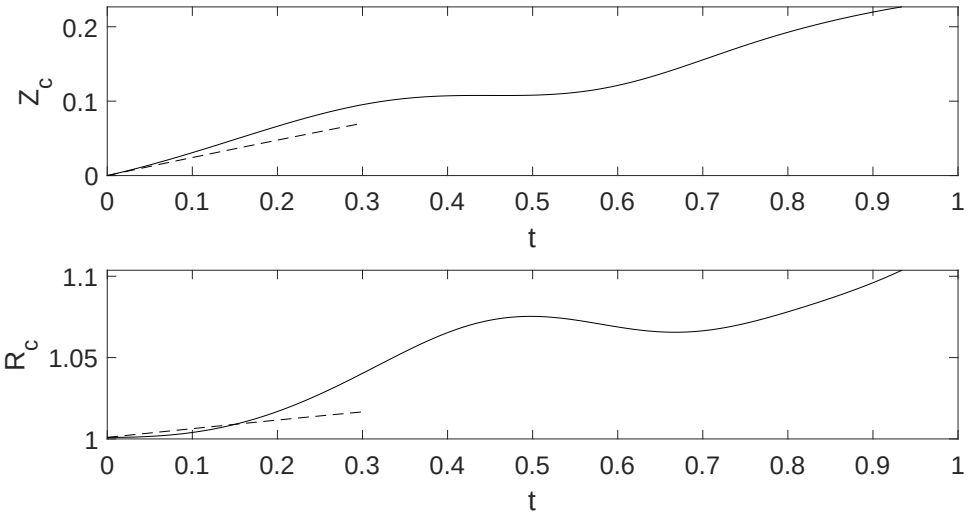

Figure 3.11: Evolution of the centroid for the case with aspect ratio $S = 0.05$ shown in figure 3.10. Dashed lines are estimations using thin ring model.

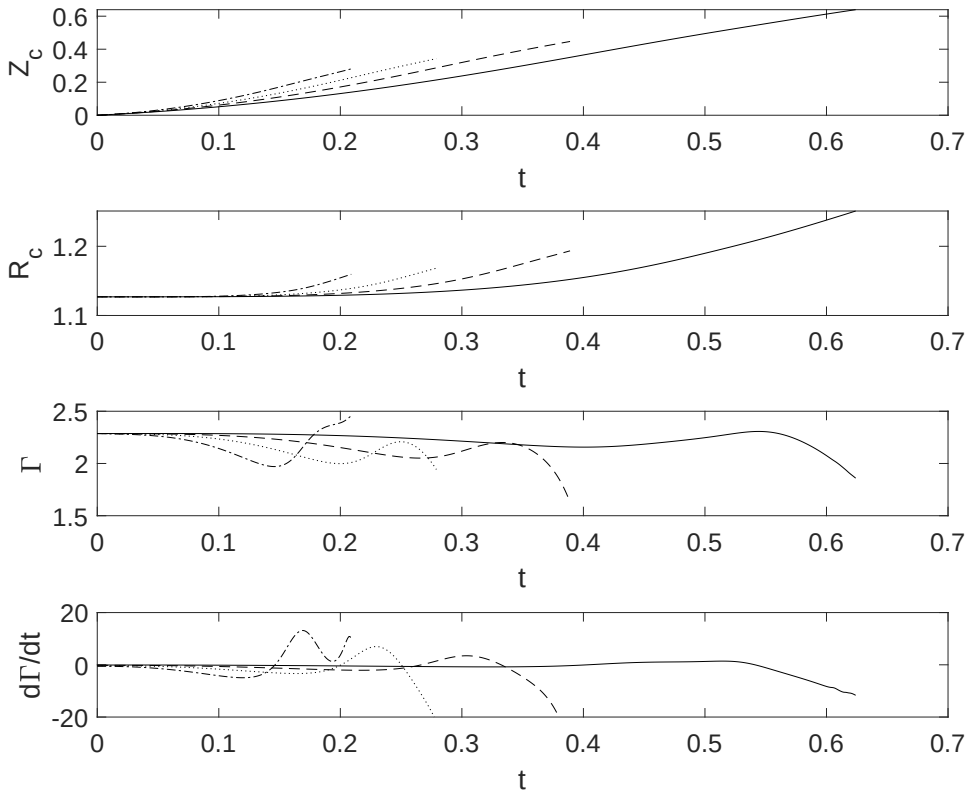

Figure 3.12: Evolution of centroid (R_c, Z_c), circulation Γ and its derivative $\mathrm{d}\Gamma/\mathrm{d}t$ for $A = 0.3$; —, $A = 0.5$; - -, $A = 0.7$; $\cdots$, $A = 1$; $\cdot$ –. The other dimensionless numbers are $S = 0.6$, $Fr = 0.3$, $We = \infty$.

To control the strength of buoyancy, we set $Fr = 0.3$ and increase A from 0.3 to 1. Figure 3.12 shows the evolution of the centroid (R_c, Z_c). Buoyancy increases the speed of the vortex ring in the vertical direction and expands the ring. The speed of translation for $A = 0.3$ is a constant and Z_c is almost linear in time. When A is increased, the ring accelerates slightly. The slope of Z_c becomes steeper in time for $A > 0.3$, which indicates that a stronger buoyancy accelerates the vortex ring in the vertical direction. The growth of R_c shown in figure 3.12 indicates the expansion of the vortex ring, which increases as buoyancy strengthens.

The evolution of circulation Γ and its derivative are plotted in figure 3.12. The

circulation of a buoyant vortex ring has contributions from both patch and sheet, with

$$\Gamma = \Gamma_p + \oint \gamma \, \mathrm{d}\xi, \quad \Gamma_p = \Omega \oint R^2 \boldsymbol{t} \cdot \mathbf{z} \, \mathrm{d}s, \tag{3.50}$$

where Γ_p is the part from the vortex patch computed using the contour integral given in Pozrikidis (1986). The sign is reversed because we evaluate the integral clockwise. The circulation contributed by the vortex sheet is calculated by integrating γ along the contour. When there is no density difference and buoyancy, circulation is conserved according to Kelvin's circulation theory, i.e. $\Gamma = \Gamma_p$ and $\mathrm{d}\Gamma/\mathrm{d}t = 0$. The material derivative of Γ can be obtained by integrating (3.34) along the contour. For the Boussinesq case, there is only one term on the right-hand side,

$$\frac{\mathrm{d}\Gamma}{\mathrm{d}t} = -2\frac{A}{Fr^2} \oint L\boldsymbol{t} \cdot \mathbf{z} \, \mathrm{d}\xi, \tag{3.51}$$

and $\mathrm{d}\Gamma/\mathrm{d}t$ is a function of the shape of the contour only. The shape is characterized by the local tangent $\boldsymbol{t}$ and the metric L. For the non-Boussinesq case, $\mathrm{d}\Gamma/\mathrm{d}t$ also requires integration over the dynamic-coupled and the quadratic terms, which are functions of γ and the dynamics of the contour. For $A = 0.3$, the rate of change of the circulation is approximately zero in figure 3.12. For larger values of A, the circulation decreases. This can be compared to the contours shown in figure 3.9. As the contours evolve and are deformed into two lobes, the vorticity on the contour is swept into the region between the two lobes and accumulate. The net effect is a negative circulation contributed by the vortex sheet. With Γ_p kept constant, the total circulation then drops. The circulation for $A = 1$ and $Fr = 0.3$ reached a minimum at $t = 0.145$ then increases beyond its initial value.

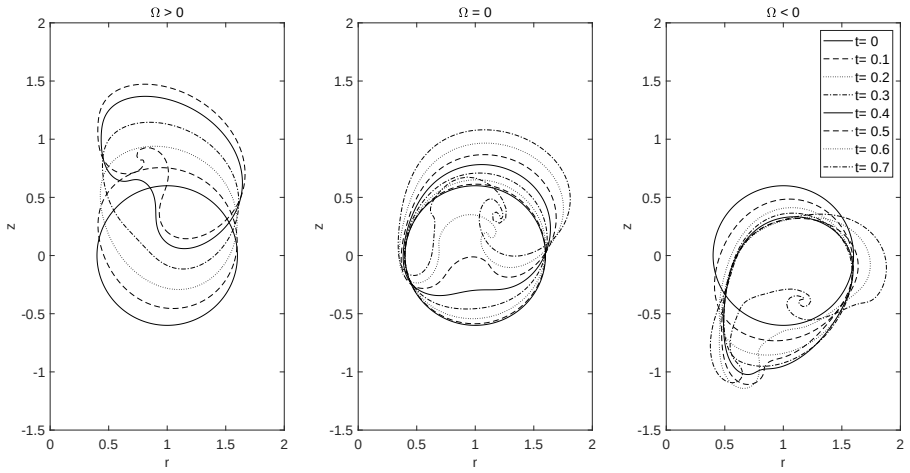

Figure 3.13: Evolution of contour for positive, zero, and negative Ω from left to right respectively. $S = 0.6$, $A = 0.3$, $We = \infty$.

3.4.5 Calculations for $\Omega \leq 0$

The results we have shown so far are for $\Omega > 0$, for which the ring is moving upward against gravity. Other possibilities include $\Omega = 0$, when the vorticity inside the core vanishes and the vortex ring is "hollow", and $\Omega < 0$, for which the vortex ring moves downward when there is no buoyancy. We calculate both cases and compare them to the $\Omega > 0$ case in figure 3.13. For $\Omega > 0$ and $\Omega < 0$, we set $|\Omega| = 6.7392$ so that $Fr = 1$. The Froude number is greater than that used in figure 3.7, so the bulk vorticity inside the core is more dominant here than the cases shown in figure 3.7 ($Fr = 0.3$). The contour still bent inward from the bottom, but it did not evolve into two counter-rotating rollups like a mushroom structure. Instead a single rollup, located on the inner half (closer to the axis of symmetry) and rotating counter-clockwise, appeared first. The outer half (away from the axis of symmetry) moved slower and is dragged behind the inner half. When the continuous vorticity Ω inside vanishes, we observe a different behaviour: a rollup rotating clockwise appeared on the outer half of the contour earlier than its counter-clockwise counterpart. This might show that the two counter-rotating rollups appeared in the $Fr = 0.3$ are

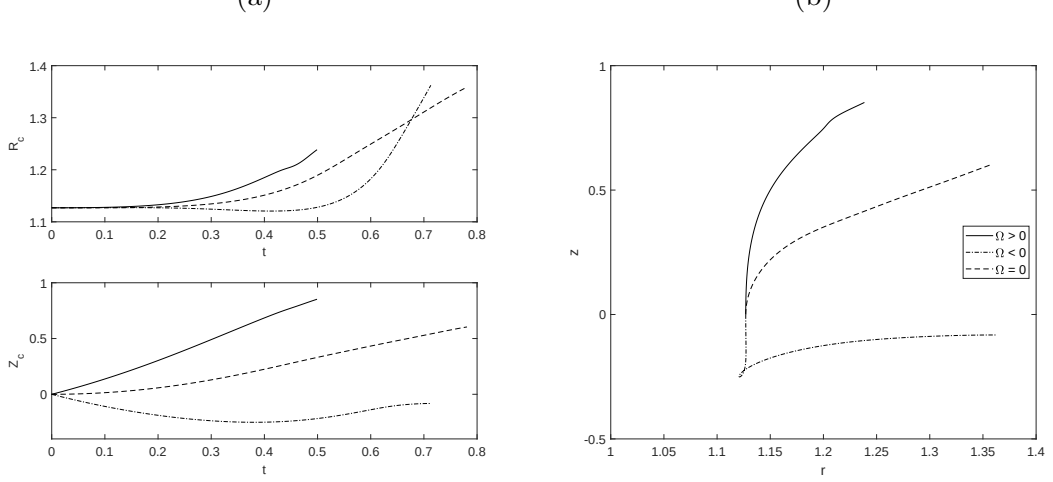

Figure 3.14: Evolution of (a) centroid: (R_c, Z_c) and (b) the trajectories for $\Omega > 0$; —, $\Omega = 0$; - -, $\Omega < 0$; $\cdot$ –.

associated with the dominant balance between the bulk vorticity (vortex ring) and the vortex sheet (density and gravity) respectively. When the bulk vorticity dominates, the counter-clockwise rollup appears, while when vortex sheet dominates the clockwise rollup emerges first. The expansion of the ring radius and the vertical speed of the ring are also decreased when the continuous vorticity vanishes (figure 3.14).

If we reverse the direction in which vortex ring travels by setting $\Omega = -6.7392$, the contour moved downward initially as shown in figure 3.13. This downward movement reversed at $t \approx 0.4$ where Z_c started to increase (figure 3.13). A clockwise rollup emerged and the end of calculation at $t = 0.7$ indicating vortex sheet grown to a stage that took over the dominance on the evolution of the contour. A long lobe close to the axis of symmetry can be seen being dragged behind as the bulk motion of the contour moves up.

3.4.6 Energy conservation

The kinetic energy of the flow associated with the vortex sheet is

$$T_s = (\rho_1 - \rho_2)\,\pi \oint \psi\ \mathbf{u}\cdot\boldsymbol{t}L\,\mathrm{d}\xi + (\rho_1+\rho_2)\,\pi \oint \frac{\psi\gamma}{2}\,\mathrm{d}\xi, \tag{3.52}$$

while the contribution from vortex patch can be calculated as a contour integral, as in (A3) of Pozrikidis (1986). The potential energy is

$$U = \pi(\rho_2-\rho_1)g \oint RZ^2\frac{\partial R}{\partial \xi}\,\mathrm{d}\xi. \tag{3.53}$$

(See appendix A.2 for detailed derivations.) In the absence of surface tension, the total energy (kinetic plus potential) is conserved under inviscid dynamics. The volume, which should also be constant in time, is numerically well conserved. For $\rho_1 = \rho_2$ and for the Boussinesq case shown in figure 3.15(a,c) respectively, this is true for energy. In the non-Boussinesq case, the numerical conservation of total energy is limited (see figure 3.15 b). It is conserved well until a certain time of integration, which decreases as A increases. For $A = 0.3$ shown in figure 3.15(b), total energy is conserved until around $t = 0.35$, whereas it is conserved when $t < 0.6$ for $A = 0.1$ and when $t < 0.12$ for $A = 0.7$. The numerical failure of energy conservation must be due to the extra terms in the non-Boussinesq cases: the dynamic-coupled term ($\mathbf{t}\cdot d\mathbf{u}/dt$) and the quadratic term ($\partial\gamma^2/\partial\xi$). The numerical problem could be due to a number of reasons including the desingularisation used in the numerical method, the growth of γ and the possible appearance of singularities discussed in § 4.2 (see figure 6). We also observed the Fourier spectrum filling up in figure 5: the numerical growth of high modes is correlated to the failure of energy conservation. Further study of the limitations of energy convervation is left as future work.

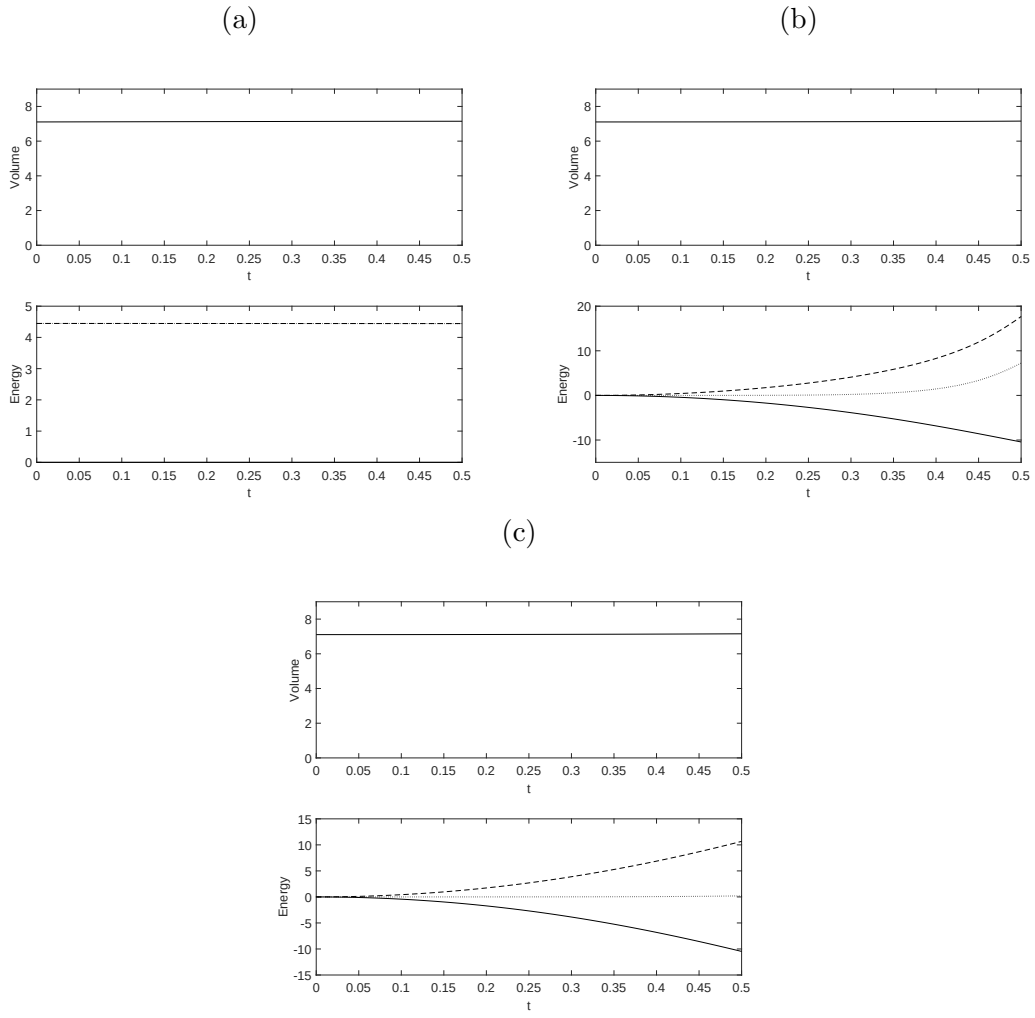

Figure 3.15: $\Omega = 0$, (a) $A = 0$; (b) $A = 0.3$; (c) Boussinesq calculation for $A = 0.3$. Potential energy; —, kinetic energy; - -, potential plus kinetic energy; $\cdots$.

3.5 Conclusion

We have presented theoretical and numerical results on the motion of a buoyant vortex ring in the non-Boussinesq regime. We derived a vortex sheet equation in (3.28) from the Euler equation. A set of coupled integro-differential equations, (3.5), (3.11), (3.13) and (3.28), is used to calculate the motion of a buoyant vortex ring. The nondimensionalized vortex sheet equation in (3.34) contains three dimensionless parameters: the Atwood number, A, the Froude number, Fr and the Weber number, We, representing different physical effects. When A and Fr are both small, the flow is in the Boussinesq limit; the vortex sheet is dominated by the gravity term and decoupled from the dynamics of the contour. The problem moves into the non-Boussinesq regime when A and Fr becomes moderate to large. In this regime, the γ equation is coupled with $\mathrm{d}\mathbf{u}/\mathrm{d}t$. The apparent emergence of curvature singularities limits the validity in time of our numerical calculations, as discussed in § 3.4.2

Our numerical results show that the contour can deform drastically when the vortex sheet is present. Numerical results are obtained for both the Boussinesq and non-Boussinesq cases where the Atwood and the Froude numbers are small to moderate. Calculations for large Froude number and Atwood number close to one have been attempted but the results are very limited. In § 3.4.3 we pointed out that a shock-like discontinuity in the vortex sheet strength γ leads to numerical failure for those cases. This does not appear to be a curvature singularity, although this may be an artifact of the blob method, since Baker & Xie (2011) showed curvature singularities approaching the real axis in the complex plane for $A = 1$. Our results for small to moderate Atwood and Froude numbers show how the motion of vortex rings deviate from a classic steady solution into nonlinear evolution when adding density effect and buoyancy. The core of the vortex ring is deformed in such a fashion that the surrounding fluid squeezes in from the bottom. In some cases, a mushroom-like pattern develops with two counter-rotating roll-ups on the contour. Surface

tension is given in our formulation, but we did not include it in the numerical results. The numerics for surface tension requires careful treatment, so the present work emphasized the effects of density and buoyancy. Our results give insights into flows dominated by buoyancy and vorticity, which have implications on geophysical and environmental fluid dynamics. Possible future work includes investigations of the stability of these vortex rings, the effect of surface tension, and as an investigation of curvature singularities in axisymmetry. These last two work would require the development of a numerical method that is robust in the presence of surface tension and that does not use blobs, e.g. adapting the midpoint rule used by Baker & Nachbin (1998) to work in axisymmetric geometry.

Chapter 3, in full, has been published in the Journal of Fluid Mechanics, "Axisymmetric contour dynamics for buoyant vortex rings" by C. Chang and S. G. Llewellyn Smith, 2020, **887**, A28 (Cambridge University Press). The dissertation author was the primary investigator and author of this material.

Chapter 4

Effects of density and surface tension on curvature instability of a vortex ring

The curvature instability of thin vortex rings is a parametric instability discovered from short-wavelength analysis by Hattori & Fukumoto (2003). A full-wavelength analysis using normal modes then followed in Fukumoto & Hattori (2005). This chapter extends the calculation to the case with different densities inside and outside the vortex core in the presence of surface tension. The maximum growth rate and the instability half-bandwidth are calculated from the dispersion relation given by the resonance between two Kelvin waves of m and $m+1$, where m is the azimuthal wavenumber. The result shows that vortex rings are unstable to resonance waves in the presence of density and surface tension. The curvature instability for the principal modes is enhanced by density variations in the small axial wavenumber regime, while the asymptote for short wavelengths is close to the constant density case. The effect of surface tension is marginal. The growth rates of non-principal modes are also examined and long waves are most unstable.

4.1 Introduction

Vortices are coherent fluid entities that can transport properties and mass through an ambient fluid. A number of geometries such as vortex columns, vortex rings, and helical vortices have been the focus of specific study. Given their apparent vulnerability to small fluctuations and susceptibility to disruption, their stability has drawn attentions from scientists and engineers, including the laboratory experiments of Maxworthy (1972, 1977); Widnall & Sullivan (1973) on vortex rings, and the theoretical studies of Widnall & Bliss (1971); Widnall (1972) on helical vortices. For vortex rings, Widnall *et al.* (1974) found that a vortex ring is unstable to bending waves. (see also Widnall & Tsai, 1977; Saffman, 1978).

We start our discussion with the simplest three-dimensional geometry. A straight vortex column with uniform vorticity inside its core is the simplest geometry in which to study the three-dimensional instabilities of vortices. Infinitesimal disturbances of this basic state of a vortex column are found to be neutrally stable and called Kelvin waves (see Saffman, 1992, § 12.1). However, an instability mechanism proposed by Widnall *et al.* (1974) showed the potential for instability: if a vortex column is perturbed by a small parameter, ϵ, to account for a small geometric or physical effect, the resulting steady-state solution can be written as a perturbation series of ϵ. This basic solution is then disturbed by Kelvin waves, which can interact with the $O(\epsilon)$ part of the basic state, potentially leading to instabilities. For example, a vortex column subjected to the external strain field $(\epsilon y, -\epsilon x, 0)$ perpendicular to the axis of the vortex column, is unstable as was discovered by Moore & Saffman (1975) and Tsai & Widnall (1976). This is known as the Moore–Saffman–Tsai–Widnall (MSTW) instability. The strained vortex column disturbed by Kelvin waves whose interaction leads to a resonance between two Kelvin waves with azimuthal wavenumber separated by 2. This resonance leads to the exponential growth of infinitesimal waves. The MSTW instability has been studied extensively in, e.g. Eloy & Le

Dizès (2001); Fukumoto (2003), and is related to the elliptic instability in the short-wave limit (see Bayly, 1986; Waleffe, 1990; Leweke & Williamson, 1998).

The same perturbation expansion in ϵ can be used for the stability analysis of a thin vortex ring. For a thin vortex ring, ϵ is defined as

$$\epsilon = \frac{a}{R} \tag{4.1}$$

where a is its core size and R is the ring radius. If $\epsilon \ll 1$, the ring appears locally as a vortex tube perturbed by small curvature ϵ. We obtain the basic state solution for a vortex ring as an expansion in ϵ. Using the coordinates in figure 4.1, the resulting instability problem was first set up for a thin vortex ring with an uniform core in Widnall & Tsai (1977). Their short-wavelength analysis shows that the MSTW instability arises from the interaction between Kelvin waves and the basic state at $O(\epsilon^2)$. They concluded that the MSTW instability is responsible for the instability of a thin vortex ring observed in the experiments of Widnall & Sullivan (1973). However Hattori & Fukumoto (2003) discovered another instability that they named curvature instability. They showed that disturbances are then also unstable in the short-wavelength limit by calculating the growth rate using the geometric optics method. Fukumoto & Hattori (2005) then carried out a normal mode analysis using the setup of Widnall & Tsai (1977). A dipole field arising from the basic state in $O(\epsilon)$ leads to resonances between two Kelvin waves of wavenumber separated by 1 and instability emerges. All possible resonant pairs of Kelvin waves with azimuthal wavenumber m and $m + 1$ were examined, and larger m were found to be more unstable. Fukumoto & Hattori (2005) also argued that curvature instability is more unstable than the MSTW instability for a uniform core when $\epsilon \ll 1$.

Recent studies have examined vortices with a non-uniform core: Blanco-Rodriguez & Le Dizès (2016) and Blanco-Rodriguez & Le Dizès (2017) use Gaussian distributions of

vorticity for the vortex core and subjected to elliptic and curvature instabilities. Hattori, Blanco-Rodriguez & Dizès (2019) studied the short-wavelength instabilities of a vortex ring with Gaussian distributions of vorticity and swirl. They found from direct numerical simulations that only the elliptic instability is observed when there is no swirl flow, while the curvature instability emerges when swirl is present but is limited to certain wavenumber range. This is the first numerical evidence confirming the curvature instability of a vortex ring.

All the studies above are for constant-density flows. There are, however, many example of vortex rings in natural and industrial situations for which density effects are important. Vortex rings generated by density differences are examples of thermals (Turner, 1973), and are important in geological and environmental safety applications. (Saffman, 1992, § 5.8) discusses the motion of buoyant vortex rings using conserved quantities, while Baumann *et al.* (1992) examines their fall. Dolphins are known to create air-filled bubble rings (Marten *et al.*, 1996). Once created, these thin hollow rings seem to survive until the dolphins destroy them, raising the question of their stability. Here we aim to extend the linear stability analysis to a vortex ring with density differing from that of its ambient.

The densities are unequal but constant inside and outside the core. Surface tension is also considered. This configuration is consistent with previous work, and we follow them by taking a Rankine vortex as the ring's core. In present chapter, we follow the calculation in Fukumoto & Hattori (2005) and carry out a normal mode analysis for the curvature instability. In § 4.2, the linearised governing equations and boundary conditions for infinitesimal disturbances are given. The basic state solution as a perturbation series up to $O(\epsilon)$ is also given. We discuss Kelvin waves with densities and surface tension in §,4.3. The growth rate and the half-bandwidth of the curvature instability and numerical examples are presented in § 4.4. We draw conclusions in §,4.5 and return to the MSTW instability in the next chapter.

Figure 4.1: (a) Top view of a thin vortex ring and (b) a cross-section view of the xy-plane. The ring moves in the x-direction ($\theta = 0$).

4.2 Formulation

A vortex ring with radius R and core size a is considered. The core is taken to be thin, so that $\epsilon = a/R \ll 1$. The outer region and the vortical core have constant densities ρ_1 and ρ_2 respectively. The circulation around the core is Γ. The problem is nondimensionalized using length scale a, velocity scale $U_c = \Gamma/(2\pi a)$, and time scale $2\pi a^2/\Gamma$, while the pressure scale is taken to be $\rho_2(\Gamma/2\pi a)^2$. The velocity potential describing the outer irrotational flow is scaled by $\Gamma/2\pi$.

Density differences in the presence of a gravity field lead to buoyancy effects acting on the vortex ring. However, buoyant vortex rings (whether light or heavy, $\rho_1 \neq \rho_2$) do not move steadily (see e.g. Turner, 1957; Pedley, 1968; Chang & Llewellyn Smith, 2018). Light vortex rings expand with the radius growing like $\sqrt{t}$, and the speed slows down as $t^{-1/2} \ln t$. To avoid this complication, we consider buoyancy to have a slowly-varying effect so that the mean flow is "frozen" in time. This is justified on the basis that the Froude number

$$Fr = \frac{\Gamma/(2\pi a)}{\sqrt{ag}}$$

is very large. The time scale of the rotational motion inside the core $\sim a^2/\Gamma$, while the time scale of buoyant motion is $\sim \sqrt{a/g}$. Then $\sqrt{a/g} \gg a^2/\Gamma$ is equivalent to $Fr \gg 1$,

so the vortex ring can be considered frozen on the time scale of a^2/Γ. Therefore, gravity term is omitted in the governing equations.

4.2.1 Governing equations

Following Fukumoto & Hattori (2005), we use a coordinate system (r, θ, s) co-moving with the ring, as shown in figure 4.1, with velocity $\mathbf{u} = (u, v, w)$. The undisturbed core boundary is taken to be $r = 1$. Since the core is rotational, the governing equations in the inner region are the Euler equations,

$$\boldsymbol{\nabla} \cdot \mathbf{u} = 0, \qquad \frac{\partial \mathbf{u}}{\partial t} + \mathbf{u} \cdot \boldsymbol{\nabla}\mathbf{u} = -\boldsymbol{\nabla} p. \tag{4.2}$$

Vorticity is zero outside the core of the vortex ring, and the Laplace equation in the outer irrotational region is

$$\nabla^2 \Phi = 0, \tag{4.3}$$

where Φ is the velocity potential.

In the (r, θ, s) coordinates the Euler equations become

$$\frac{\partial u}{\partial t} + \mathbf{u} \cdot \boldsymbol{\nabla} u - \frac{v^2}{r} - \epsilon \frac{w^2 \sin\theta}{h_s} = -\frac{\partial p}{\partial r}, \tag{4.4}$$

$$\frac{\partial v}{\partial t} + \mathbf{u} \cdot \boldsymbol{\nabla} v + \frac{uv}{r} - \epsilon \frac{w^2 \cos\theta}{h_s} = -\frac{1}{r}\frac{\partial p}{\partial \theta}, \tag{4.5}$$

$$\frac{\partial w}{\partial t} + \mathbf{u} \cdot \boldsymbol{\nabla} w + \epsilon \frac{w(u \sin\theta + v \cos\theta)}{h_s} = -\frac{1}{h_s}\frac{\partial p}{\partial s}, \tag{4.6}$$

where $h_s = 1 + \epsilon r \sin\theta$, and

$$\mathbf{u} \cdot \boldsymbol{\nabla} = u\frac{\partial}{\partial r} + \frac{v}{r}\frac{\partial}{\partial \theta} + \frac{w}{h_s}\frac{\partial}{\partial s}. \tag{4.7}$$

The continuity equation is

$$\frac{1}{r}\frac{\partial}{\partial r}(ru) + \frac{1}{r}\frac{\partial v}{\partial \theta} + \frac{1}{h_s}\frac{\partial w}{\partial s} + \frac{\epsilon}{h_s}(u\sin\theta + v\cos\theta) = 0. \tag{4.8}$$

Outside the core, Laplace's equation becomes

$$\frac{1}{r}\frac{\partial}{\partial r}\left(r\frac{\partial \Phi}{\partial r}\right) + \frac{1}{r^2}\frac{\partial^2 \Phi}{\partial \theta^2} + \frac{1}{h_s^2}\frac{\partial^2 \Phi}{\partial s^2} + \frac{\epsilon}{h_s}\left(\sin\theta\frac{\partial \Phi}{\partial r} + \frac{\cos\theta}{r}\frac{\partial \Phi}{\partial \theta}\right) = 0. \tag{4.9}$$

4.2.2 Boundary conditions

The boundary of the vortex is taken to be $r = F(\theta;\epsilon)$, where $F(\theta;\epsilon)$ will be found as part of the solution. The inner and outer solutions are matched on the core boundary. For inviscid flows, the matching conditions are given by the kinematic and the dynamic conditions. The kinematic condition is

$$\frac{\mathrm{D}}{\mathrm{D}t}(r-F)\bigg|_{r\to F^-} = \frac{\mathrm{D}}{\mathrm{D}t}(r-F)\bigg|_{r\to F^+} = 0, \tag{4.10}$$

where $\mathrm{D}/\mathrm{D}t$ is the usual Lagrangian time derivative and $\pm$ represent the inside and outside of the boundary, respectively.

The dynamic condition relates the jump in pressure across the boundary to surface tension. Because the outer flow is irrotational, we can use the unsteady Bernoulli equation to express the pressure there in terms of a velocity potential. Taking pressure to vanish at infinity without loss of generality, one obtains

$$\frac{\rho_2}{\rho_1}p + \frac{\partial \Phi}{\partial t} + \frac{1}{2}|\boldsymbol{\nabla}\Phi|^2 = S\boldsymbol{\nabla}\cdot\boldsymbol{n}. \tag{4.11}$$

Here S is dimensionless surface tension $\sigma/[\rho_1 a(\Gamma/2\pi a)^2]$ and $\boldsymbol{n} = \nabla(r-F)/|\nabla(r-F)|$ is the outward normal vector on the boundary.

4.2.3 The mean flow solution

Linear stability analysis needs a steady state solution as a base to be "perturbed" by infinitesimal disturbances. At $O(1)$, a steady solution exists describing the vortex ring in a moving coordinate system. The solution (written using uppercase letters) can be obtained as a perturbation series in ϵ:

$$\boldsymbol{U} = \boldsymbol{U}_0 + \epsilon \boldsymbol{U}_1 + \cdots, \quad P = P_0 + \epsilon P_1 + \cdots, \quad \Phi = \Phi_0 + \epsilon \Phi_1 + \cdots, \tag{4.12}$$

as in § 2 of Fukumoto & Hattori (2005) who take $\rho_1 = \rho_2$. The leading-order solution corresponds to a vortex column perturbed by the small dimensionless curvature of the vortical core. The shape of the boundary is formally expanded in ϵ, but is taken to be circular, so that the expansion is redundant.

Here we use the same basic state with a correction for $\rho_1 \neq \rho_2$. A normal mode analysis of the disturbances then leads to a dispersion relation and possible instability. We now obtain the basic solution for the stability calculation using (4.12). The leading-order mean flow solution is the Rankine vortex with velocity and pressure fields

$$(U_0, V_0, W_0) = (0, r, 0), \quad P_0 = \frac{1}{2}\left(r^2 - 1 - \frac{\rho_1}{\rho_2}\right) + \frac{\rho_1}{\rho_2} S \tag{4.13}$$

inside the core ($r < 1$). The boundary of the vortex is circular, so that $F_0 = 1$. The velocity potential outside ($r > 1$) is

$$\Phi_0 = \theta. \tag{4.14}$$

Curvature leads to the following $O(\epsilon)$ contribution to the mean flow:

$$U_1 = \frac{5}{8}(1 - r^2)\cos\theta, \qquad V_1 = \frac{1}{8}(7r^2 - 5)\sin\theta, \qquad P_1 = \left(\frac{3}{8}r^3 - \frac{5}{8}r\right)\sin\theta \tag{4.15}$$

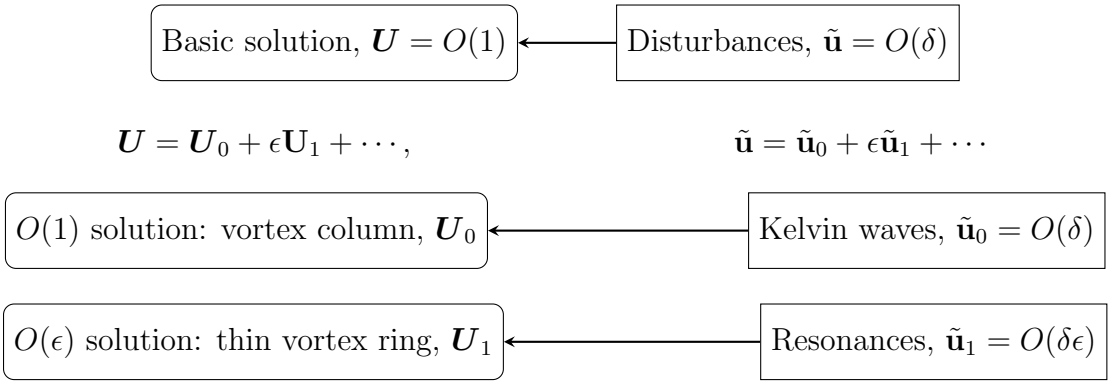

Figure 4.2: Schematic structure of the present calculation. The basic state solution is given as a perturbation series in ϵ.

in the inner region, while the outer solution is a dipole field:

$$\Phi_1 = \frac{1}{8}\left[2\left(r - \frac{1}{r}\right) - \frac{\rho_2}{\rho_1}\left(r + \frac{1}{r}\right) - 4S\left(r + \frac{1}{r}\right) - 4r\log r\right]\cos\theta. \tag{4.16}$$

The shape of the boundary has been taken to remain circular to $O(\epsilon)$, i.e. $F_1 = 0$. See appendix B.1.1 for detailed calculations yielding (4.13)–(4.16). The mean flow solution can be compared to the result of Fukumoto & Hattori (2005) by taking $\rho_2/\rho_1 = 1$ and $S = 0$.

4.2.4 Linearised equations and boundary conditions for infinitesimal disturbances

We disturb the mean flow derived in the previous subsection, and write

$$U + \tilde{u}, \quad V + \tilde{v}, \quad W + \tilde{w}, \quad P + \tilde{p}, \quad \Phi + \tilde{\phi}, \tag{4.17}$$

where the disturbed boundary is $r = F + \tilde{f}$. The structure of the solution is outlined in figure 4.2. Disturbances, denoted by tilde, are $O(\delta)$ compared to the mean flow with $\delta \ll 1$. In parallel, the solution is expanded in ϵ, the small non-dimensional core size. For this

stability analysis, we are interested in disturbances at $O(\delta)$ and $O(\delta\epsilon)$. The vortex column solution given by $\boldsymbol{U}_0$ is neutrally stable, supporting Kelvin waves $\tilde{\mathbf{u}}_0$. However, when a small parameter ϵ is introduced, instability can be excited corresponding to resonance or parametric instability. Disturbances are decomposed into normal modes in s and t, that are expanded in ϵ as

$$\tilde{\mathbf{u}} = (\tilde{\mathbf{u}}_0 + \epsilon\tilde{\mathbf{u}}_1 + \cdots)\mathrm{e}^{\mathrm{i}(ks-\omega t)}, \tag{4.18}$$

$$\tilde{p} = (\tilde{p}_0 + \epsilon\tilde{p}_1 + \cdots)\mathrm{e}^{\mathrm{i}(ks-\omega t)}, \tag{4.19}$$

$$\tilde{\phi} = (\tilde{\phi}_0 + \epsilon\tilde{\phi}_1 + \cdots)\mathrm{e}^{\mathrm{i}(ks-\omega t)}, \tag{4.20}$$

where the real part is implicit with no loss of generality. The wavenumber and the frequency are also expanded as

$$k = k_0 + \epsilon k_1 + \cdots, \qquad \omega = \omega_0 + \epsilon\omega_1 + \cdots. \tag{4.21}$$

The core boundary disturbance is

$$\tilde{f} = (\tilde{f}_0 + \epsilon\tilde{f}_1 + \cdots)\mathrm{e}^{\mathrm{i}(ks-\omega t)}. \tag{4.22}$$

Since the disturbances $(\tilde{\mathbf{u}}, \tilde{p}, \tilde{\phi})$ are small compared to the basic solution $(\boldsymbol{U}, P, \Phi)$, (4.6)–(4.9) can be linearised.

$O(\delta)$ linearised equations and boundary conditions

The linearised equations for disturbances at $O(\delta)$ are

$$-\mathrm{i}\omega_0\tilde{u}_0 + \frac{V_0}{r}\frac{\partial\tilde{u}_0}{\partial\theta} - \frac{2V_0\tilde{v}_0}{r} = -\frac{\partial\tilde{p}_0}{\partial r}, \tag{4.23}$$

$$-\mathrm{i}\omega_0\tilde{v}_0 + \frac{V_0}{r}\frac{\partial\tilde{v}_0}{\partial\theta} + \left(\frac{\partial V_0}{\partial r} + \frac{V_0}{r}\right)\tilde{u}_0 = -\frac{1}{r}\frac{\partial\tilde{p}_0}{\partial\theta}, \tag{4.24}$$

$$-\mathrm{i}\omega_0\tilde{w}_0 + \frac{V_0}{r}\frac{\partial\tilde{w}_0}{\partial\theta} = -\frac{\partial\tilde{p}_0}{\partial s}, \tag{4.25}$$

$$\frac{1}{r}\frac{\partial}{\partial r}(r\tilde{u}_0) + \frac{1}{r}\frac{\partial\tilde{v}_0}{\partial\theta} + \frac{\partial\tilde{w}_0}{\partial s} = 0 \tag{4.26}$$

inside and

$$\frac{1}{r}\frac{\partial}{\partial r}\left(r\frac{\partial\tilde{\phi}_0}{\partial r}\right) + \frac{1}{r^2}\frac{\partial^2\tilde{\phi}_0}{\partial\theta^2} + \frac{\partial^2\tilde{\phi}_0}{\partial s^2} = 0 \tag{4.27}$$

outside the core. The linearised boundary conditions at $r = 1$ are

$$\tilde{u}_0 = \frac{\partial\tilde{\phi}_0}{\partial r} = -\mathrm{i}\omega_0\tilde{f}_0 + \frac{\partial\tilde{f}_0}{\partial\theta}, \tag{4.28}$$

$$\frac{\rho_2}{\rho_1}\tilde{p}_0 - \mathrm{i}\omega_0\tilde{\phi}_0 + \frac{\partial\tilde{\phi}_0}{\partial\theta} = \left(1 - \frac{\rho_2}{\rho_1}\right)\tilde{f}_0 - S\left(\frac{\partial^2\tilde{f}_0}{\partial\theta^2} - k_0^2\tilde{f}_0\right). \tag{4.29}$$

The solutions to this problem are Kelvin waves, as detailed below and in appendix B.2.

$O(\delta\epsilon)$ linearised equations and boundary conditions

We proceed to $O(\delta\epsilon)$. The inner solution satisfies

$$-\mathrm{i}\omega_0\tilde{u}_1 + \frac{\partial\tilde{u}_1}{\partial\theta} - 2\tilde{v}_1 + \frac{\partial\tilde{p}_1}{\partial r} = \left(\mathrm{i}\omega_1 - \frac{\partial U_1}{\partial r}\right)\tilde{u}_0 - U_1\frac{\partial\tilde{u}_0}{\partial r} - \frac{V_1}{r}\frac{\partial\tilde{u}_0}{\partial\theta} - \left(\frac{1}{r}\frac{\partial U_1}{\partial\theta} - \frac{2V_1}{r}\right)\tilde{v}_0, \tag{4.30}$$

$$-\mathrm{i}\omega_0\tilde{v}_1 + 2\tilde{u}_1 + \frac{\partial\tilde{v}_1}{\partial\theta} + \frac{1}{r}\frac{\partial\tilde{p}_1}{\partial\theta} = \left(\mathrm{i}\omega_1 - \frac{1}{r}\frac{\partial V_1}{\partial\theta} - \frac{V_1}{r}\right)\tilde{v}_0 - U_1\frac{\partial\tilde{v}_0}{\partial r} - \frac{V_1}{r}\frac{\partial\tilde{v}_0}{\partial\theta} - \left(\frac{\partial V_1}{\partial r} + \frac{V_1}{r}\right)\tilde{u}_0, \tag{4.31}$$

$$-\mathrm{i}\omega_0\tilde{w}_1 + \frac{\partial\tilde{w}_1}{\partial\theta} + \mathrm{i}k_0\tilde{p}_1 = -\mathrm{i}(k_1 - k_0 r\sin\theta)\tilde{p}_0 + (\mathrm{i}\omega_1 - r\cos\theta)\tilde{w}_0 - U_1\frac{\partial\tilde{w}_0}{\partial r} - \frac{V_1}{r}\frac{\partial\tilde{w}_0}{\partial\theta}, \tag{4.32}$$

$$\frac{\partial\tilde{u}_1}{\partial r} + \frac{\tilde{u}_1}{r} + \frac{1}{r}\frac{\partial\tilde{v}_1}{\partial\theta} + \mathrm{i}k_0\tilde{w}_1 = -\mathrm{i}(k_1 - k_0 r\sin\theta)\tilde{w}_0 - \tilde{u}_0\sin\theta - \tilde{v}_0\cos\theta. \tag{4.33}$$

The velocity potential outside satisfies

$$\frac{\partial^2\tilde{\phi}_1}{\partial r^2}+\frac{1}{r}\frac{\partial\tilde{\phi}_1}{\partial r}+\frac{1}{r^2}\frac{\partial^2\tilde{\phi}_1}{\partial\theta^2}-k_0^2\tilde{\phi}_1=2(k_0k_1-k_0^2r\sin\theta)\tilde{\phi}_0-\sin\theta\frac{\partial\tilde{\phi}_0}{\partial r}-\frac{\cos\theta}{r}\frac{\partial\tilde{\phi}_0}{\partial\theta}. \quad (4.34)$$

The linearised boundary conditions at $r=1$ are

$$-\mathrm{i}\omega_0\tilde{f}_1+\frac{\partial\tilde{f}_1}{\partial\theta}-\tilde{u}_1=\mathrm{i}\omega_1\tilde{f}_0-V_1\frac{\partial\tilde{f}_0}{\partial\theta}+\frac{\partial U_1}{\partial r}\tilde{f}_0, \quad (4.35)$$

$$\tilde{u}_1=\frac{\partial\tilde{\phi}_1}{\partial r}, \quad (4.36)$$

$$\frac{\rho_2}{\rho_1}\tilde{p}_1-\mathrm{i}\omega_0\tilde{\phi}_1+\frac{\partial\tilde{\phi}_1}{\partial\theta}=\mathrm{i}\omega_1\tilde{\phi}_0-\frac{\partial\Phi_1}{\partial\theta}\frac{\partial\tilde{\phi}_0}{\partial\theta}+\left(1-\frac{\rho_2}{\rho_1}\right)\tilde{f}_1+2S\sin\theta\tilde{f}_0 \quad (4.37)$$
$$-S\left(\frac{\partial^2\tilde{f}_1}{\partial\theta^2}-k_0^2\tilde{f}_1-2k_0k_1\tilde{f}_0+2\sin\theta\ k_0^2\tilde{f}_0+\cos\theta\frac{\partial\tilde{f}_0}{\partial\theta}\right).$$

The dispersion relations at $O(\delta)$ and $O(\delta\epsilon)$ are obtained from (4.28–4.29), and (4.36–4.37) respectively. The condition (4.35) is used only to determine the boundary shape $\tilde{f}_1$, and is not required to calculate the dispersion relation when surface tension term vanishes (Fukumoto & Hattori, 2005).

4.3 $O(\delta)$ solution: Kelvin waves on a vortex column

The disturbances satisfying (4.23)–(4.27) are written as

$$\tilde{\mathbf{u}}_0(r,\theta)=\mathbf{u}_0^{(m)}(r)\mathrm{e}^{\mathrm{i}m\theta},\quad \tilde{p}_0(r,\theta)=p_0^{(m)}(r)\mathrm{e}^{\mathrm{i}m\theta},\quad \tilde{\phi}_0(r,\theta)=\phi_0^{(m)}(r)\mathrm{e}^{\mathrm{i}m\theta}, \quad (4.38)$$

where m is the azimuthal wavenumber. The solution at leading order is a Kelvin wave, described in appendix B.2. The Kelvin waves are coupled to the dipole field (4.15)–(4.16) through the right-hand sides of (4.30)–(4.34). When two Kelvin waves with wavenumber m and $m+1$ appear in the forcing terms on the right-hand side of (4.30)–(4.34), the

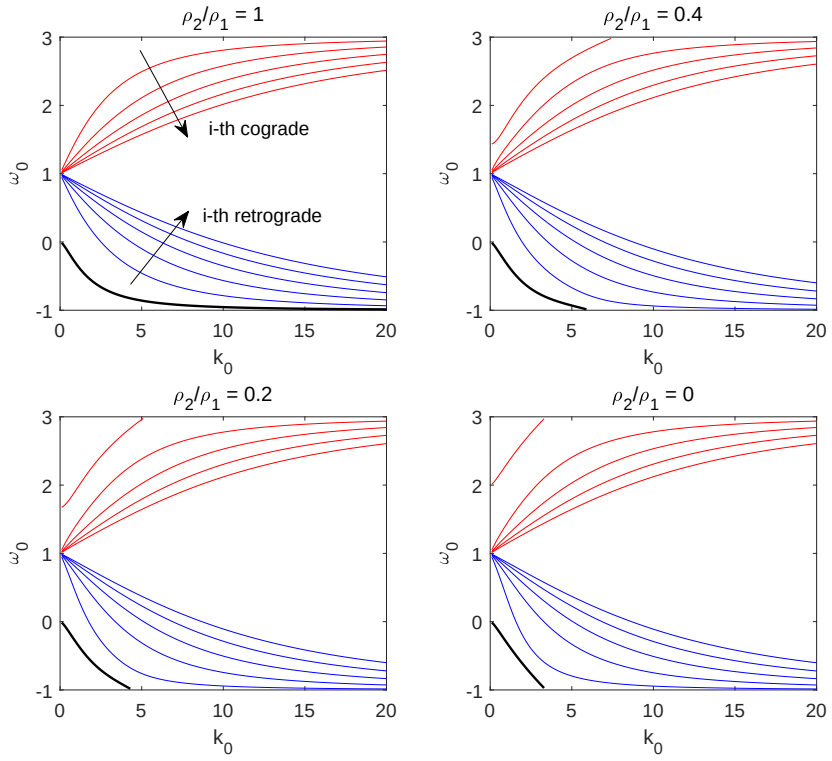

Figure 4.3: Dispersion curves for the Kelvin wave with $m = 1$ for density ratios from one to zero. Red curves are cograde branches and blue curves are retrograde branches. Only the first five branches are plotted, which have the largest value of $|\omega_0 - m|$ in each of the cograde and retrograde modes. An isolated branch (thick black curve) can be seen emanating from $(k_0, \omega_0) = (0, m-1)$. Surface tension is zero for all plots.

solution at the $O(\delta\epsilon)$ will possess modes for $m-1$, m, $m+1$ and $m+2$. We focus on the resonance between pairs of Kelvin waves $(m, m+1)$ in this study.

The solution (B.16) and (B.18) contains the amplitudes of Kelvin waves, α_0, β_0, that are determined using the boundary conditions. The boundary conditions (4.28) and (4.29) for wavenumber m become

$$-\mathrm{i}(\omega_0 - m) f_0^{(m)} = u_0^{(m)} = \frac{\mathrm{d}\phi_0}{\mathrm{d}r}^{(m)}, \tag{4.39}$$

$$\frac{\rho_2}{\rho_1} p_0^{(m)} - \mathrm{i}(\omega_0 - m)\phi_0^{(m)} = \left(1 - \frac{\rho_2}{\rho_1}\right) f_0^{(m)} + S(m^2 + k_0^2) f_0^{(m)}. \tag{4.40}$$

Substituting $p_0^{(m)}$, $u_0^{(m)}$, $\phi_0^{(m)}$ and $f_0^{(m)}$ (see appendix B.2) into the equations above, we obtain a set of homogeneous linear equations for $\alpha_0^{(m)}$ and $\beta_0^{(m)}$. For non-trivial $\alpha_0^{(m)}$ and $\beta_0^{(m)}$, the determinant must be zero, which gives the dispersion relation for mode m:

$$\left[1+\frac{E_1}{(\omega_0-m)^2}\left(m-k_0\frac{K_{m+1}(k_0)}{K_m(k_0)}\right)\right]J_{m+1}(\eta_1)=\left\{-m\frac{\omega_0-m}{\omega_0-m+2}\right.$$
$$\left.+\left[\frac{\rho_2}{\rho_1}-E_1\frac{m}{(\omega_0-m)(\omega_0-m+2)}\right]\left(m-k_0\frac{K_{m+1}(k_0)}{K_m(k_0)}\right)\right\}\frac{\eta_1}{k_0^2}\,J_m(\eta_1), \tag{4.41}$$

where

$$E_1=1-\frac{\rho_2}{\rho_1}+S(k_0^2+m^2).$$

Here J_m is the Bessel function of the first kind and K_m is the modified Bessel function of the second kind; η_1 is the radial wavenumber for the Kelvin wave defined in (B.17). For the $m+1$-wave, the boundary conditions are the same formulas as in (4.40) except that m is replaced by $m+1$, and similarly for the solution in appendix B.2. Using the boundary conditions and the solution for the $m+1$-mode, we obtain the dispersion relation,

$$\left[1-\frac{E_2}{(\omega_0-m-1)^2}\left(m+1+k_0\frac{K_m(k_0)}{K_{m+1}(k_0)}\right)\right]J_m(\eta_2)=\left\{-(m+1)\frac{\omega_0-m-1}{\omega_0-m-3}\right.$$
$$\left.+\left[\frac{\rho_2}{\rho_1}+E_2\frac{m+1}{(\omega_0-m-1)(\omega_0-m-3)}\right]\left(m+1+k_0\frac{K_m(k_0)}{K_{m+1}(k_0)}\right)\right\}\frac{\eta_2}{k_0^2}\,J_{m+1}(\eta_2), \tag{4.42}$$

for it, where $E_2=1-\rho_2/\rho_1+S[k_0^2+(m+1)^2]$ and η_2 is also the radial wavenumber for $m+1$.

If we set the density ratio to one and surface tension to zero, we can easily recover (4.42) and (4.41) from the dispersion relation for Kelvin waves (B6 and B7 in Fukumoto & Hattori, 2005). The dispersion curves for modes for $m=1$ are plotted in figure 4.3 and 4.4 as functions of density ratio and surface tension. There are infinitely many branches of cograde and retrograde modes for each Kelvin wave with wavenumber m. Figures 4.3 and 4.4 show the first five branches in each of the cograde and the retrograde modes. An

isolated branch is also shown. We designate the branch with the largest value of $|\omega_0 - m|$ for a given k_0 as the first cograde/retrograde branch and then counting the branches toward $\omega_0 = m$. So the uppermost cograde branch and the bottommost retrograde branch are the first cograde and first retrograde modes. Every mode of m has cograde branches going upward where $\omega_0 > m$ and retrograde branches going downward where $\omega_0 < m$, plotted in red and blue respectively. All the cograde and retrograde branches radiate out from $(k_0, \omega_0) = (0, m)$ when $\rho_2/\rho_1 = 1$. There is an isolated branch starting from $(0, m-1)$ that only appears when $m \neq 0$. In figure 4.3, we can see how decreasing the density ratio from one to zero changes the dispersion relation of Kelvin waves: all the branches move away from the centerline $\omega_0 = m$, the cograde ones shift toward $\omega_0 = m + 2$ and the retrograde and isolated branches shift toward $\omega_0 = m - 2$. While the branches shift, the starting point of all the branches remains the same. One exception is the outermost cograde branch: its starting point moves from $(0, m)$ upward to $(0, m+1)$ when ρ_2/ρ_1 drops to zero in figure 4.3. We refer this as "isolation" of the cograde mode. Similar changes are also observed when surface tension increases from zero to one in figure 4.4: the cograde branches move toward $\omega_0 = m + 2$, the retrograde and isolated branches move toward $\omega_0 = m - 2$. The uppermost cograde mode departs from the other cograde modes and becomes isolated. The impact of this change is that a intersection point could disappear when $(\rho_2/\rho_1, S)$ deviates from $(1, 0)$ (see figure 4.5).

There is another significant change to the Kelvin waves with density and surface tension: the top branches and the bottom downward branches, i.e. the first cograde mode and the isolated mode respectively, have a real part ω_0 that disappears at some point $(k_0, m \pm 2)$ on the top or the bottom edge of the plot. Since k_0 is always real, the radial wavenumber $\eta_1 = k_0\sqrt{4/(\omega_0 - m)^2 - 1}$ is real only if $\omega_0 \in (m-2, m+2)$. For the case of $\rho_2/\rho_1 = 1$ and $S = 0$, all the branches lie between $\omega_0 = m - 2$ and $m + 2$, so the Kelvin waves are always neutrally stable. When $\rho_2/\rho_1 < 1$ and $S \neq 0$, the isolated branch

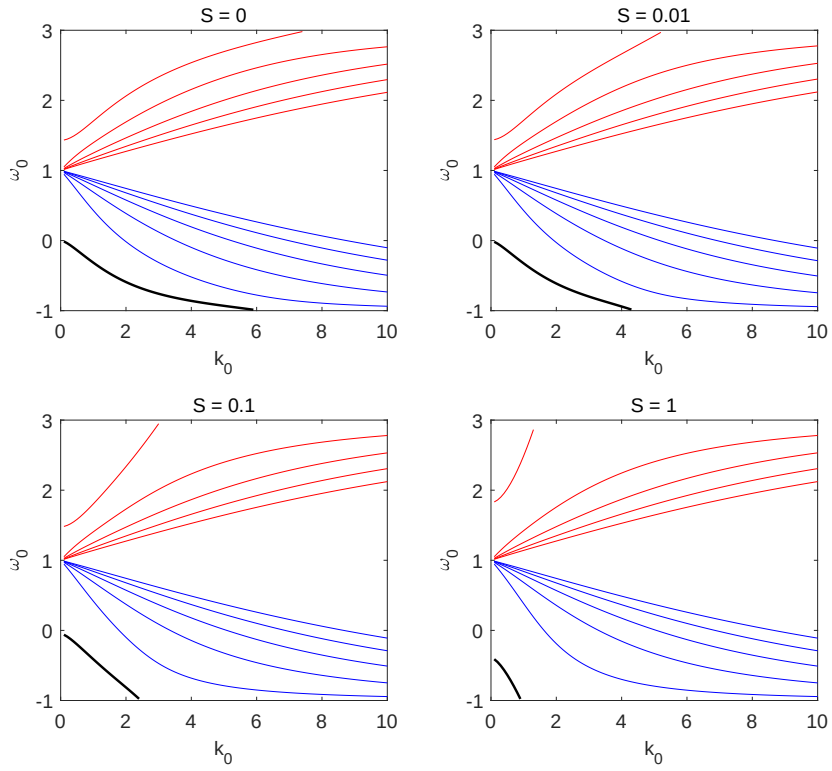

Figure 4.4: Dispersion curves for the Kelvin wave with $m = 1$ as surface tension increases from zero to one. The density ratio is fixed at $\rho_2/\rho_1 = 0.4$; other ratios give qualitatively similar results.

reaches $\omega_0 = m - 2$ on the edge of the plot, for example at $k_0 = 4.2$ in the plot for $S = 0.01$ of figure 4.4. The uppermost cograde branch reaches $\omega_0 = m + 2$ at $k_0 \approx 5.2$. For $|\omega_0 - m| > 2$, the radial wavenumber η_1 becomes pure imaginary. We can replace it by $\mathrm{i}\lambda_1$ where λ_1 is real, then replace the Bessel function of the first kind J_m in (4.41) by $\mathrm{i}^m I_m(\lambda_1)$. The new dispersion relation is real for $|\omega_0 - m| > 2$, and the upward cograde branch and the downward isolated branch extend beyond $\omega_0 = m \pm 2$.

When two Kelvin waves for wavenumber differing by 1 resonate, all their branches result in infinitely many intersection points when they cross through each other. As mentioned in Fukumoto & Hattori (2005), only the intersection points between the cograde modes m and the retrograde modes $m + 1$ are candidates for curvature instability; see figure 4.5(a) for an example. For the convenience of discussion, we follow Fukumoto & Hattori (2005) to define "principal modes". The ith principal mode is referred to as the intersection point of ith cograde and ith retrograde modes, and we indicate the first five principal modes by black dots in figure 4.5. Their growth rates are larger than those of other intersection points when $\rho_2/\rho_1 = 1$ and $S = 0$, so they will be the focus of our curvature instability calculations. Although we will show later that they do not always dominate over other intersection points when $\rho_2/\rho_1 \neq 1$ or $S \neq 0$ (see §4.4). The reader should be aware of that only four dots are shown for $\rho_2/\rho_1 = 0.4$ or below. This is due to the "isolation" of the first cograde branch of m as discussed earlier. Since it is moving away from the other cograde branches, it does not cross the first retrograde branch of $m+1$ anymore. The first principal mode then disappears. The migration of first few principal modes and the disappearance of the first mode are demonstrated in figure 4.5 b.

Note that the "principal modes" refer here to the set of principal modes when $\rho_2/\rho_1 = 1$ and $S = 0$. If we choose an arbitrary value of density ratio and plot its dispersion curve, we will obtain a plot like that for $\rho_2/\rho_1 = 0.4$ in figure 4.5. By looking at that single plot, we would not be able to see that a process of isolation had taken

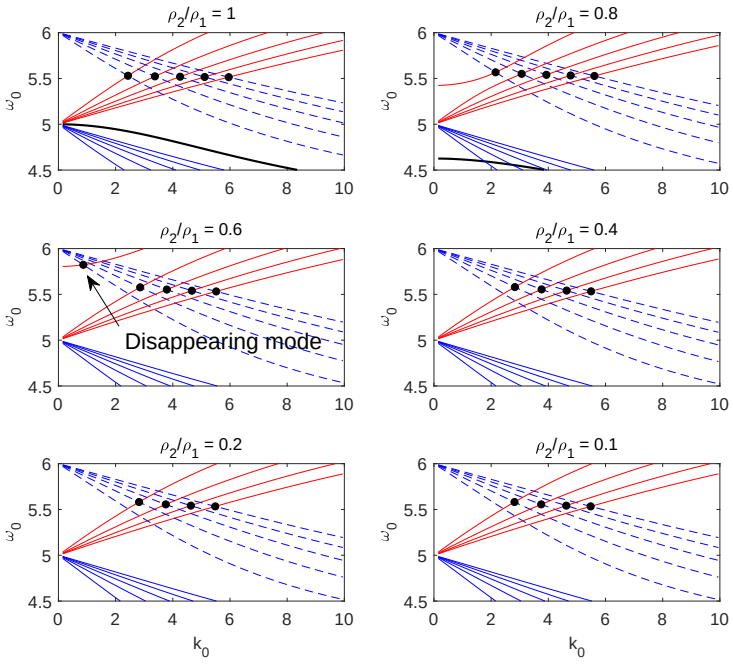

(a)

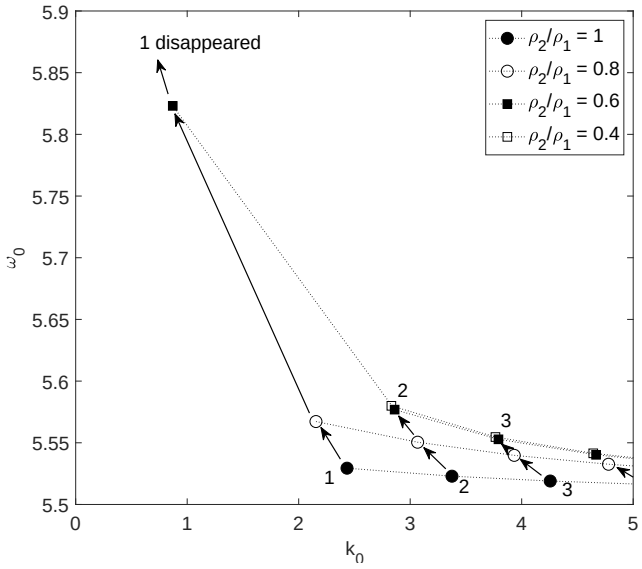

(b)

Figure 4.5: (a) Dispersion curves for a pair of Kelvin waves $m = (5, 6)$ for density ratio varying from one to zero. Solid curves are for $m = 5$ and dotted curves for $m = 6$; red is for cograde branches, blue is for retrograde branches and the black thick curve is the isolated branch. The black dots represent the first five principal modes. One of the back dots disappears when ρ_2/ρ_1 drops to 0.4 or below; (b) the migration of the principal modes as density ratio decreases. There is no mode "1" when $\rho_2/\rho_1 = 0.4$.

place, and another sequence of intersection points (just below the back dots) would have been taken as principal modes by definition. Since our goal is to investigate the effects of density and surface tension, we to keep track of the same sequence of intersection points, the principal modes for $\rho_2/\rho_1 = 1$ and $S = 0$.

4.4 $O(\delta\epsilon)$ solution: curvature as a small perturbation

The solution of the $O(\delta\epsilon)$ disturbances governed by (4.30)–(4.34) is given in appendix C of Fukumoto & Hattori (2005). We do not reproduce it here, given its complexity. The solution contains undetermined coefficients (wave amplitudes) α_1, β_1 which must be non-zero. The boundary conditions in (4.36) and (4.37) are used to obtain the dispersion relation. Note that in order to include surface tension, we need to compute $\tilde{f}_1$ from (4.35) before using the second and the third equations for the dispersion relation. In Fukumoto & Hattori (2005), $\tilde{f}_1$ is not necessary since surface tension is omitted.

The result of substituting the $O(\delta\epsilon)$ solutions for modes m and $m+1$ into (4.36) and (4.37) and the $O(\delta\epsilon)$ boundary disturbance $\tilde{f}_1$ for the two modes is given in appendix B.3. Using these results and requiring the coefficients α_1, β_1 not to vanish leads to the dispersion relation for k_1 and ω_1. The detailed calculation is outlined in appendix B.3. The dispersion relation takes the form given in (B.39). Given the cumbersome algebra which is impractical to carry out manually, we use computer-aided symbolic algebra. We validate the result obtained from symbolic algebra with the formulas for the maximum growth rate σ_{1max} and the instability half-bandwidth Δk_1 given in (2.23) and (2.24) of Fukumoto & Hattori (2005). Unfortunately, the two new parameters, ρ_2/ρ_1 and S, lead to too much complexity to check the formulas algebraically. Hence we compare our results with those of Fukumoto & Hattori (2005) for specific values. Using the formulas returned by the symbolic algebra, we calculate σ_{1max} and Δk_1 for given values of m and (k_0, ω_0). Then we set $\rho_2/\rho_1 = 1$

Table 4.1: For the $m = 0$ and 1 resonances, present results for $\rho_2/\rho_1 = 1$ compared to table 1 of Fukumoto & Hattori (2005).

	k_0	ω_0	σ_{1max}	Δk_1
Fukumoto & Hattori (2005)	0.8134868347	0.5970895378	0.05434123370	0.1022075453
	1.018687659	0.7162537484	0.007063858086	0.01725321243
	1.136862167	0.7794574187	0.008676095366	0.02449637577
	1.214999401	0.8191926924	0.007511646111	0.02329133797
Present work	0.81348683470781	0.59708953778522	0.05434123369922	0.10220754526468
	1.01868765925949	0.71625374841148	0.00706385808588	0.01725321243277
	1.13686216710968	0.77945741870128	0.00867609536636	0.02449263757654
	1.21499940056676	0.81919269238535	0.00751164611082	0.02329133797084

Table 4.2: For the $m = 5$ and 6 resonances, present results for $\rho_2/\rho_1 = 1$ compared to table 2 of Fukumoto & Hattori (2005).

	k_0	ω_0	σ_{1max}	Δk_1
Fukumoto & Hattori (2005)	2.433397462	5.529409164	0.31952046180	1.693646977
	2.794997045	5.600007679	0.05182563467	0.3171404496
	3.052129222	5.648538465	0.02232672268	0.1506487379
Present work	2.43339746175187	5.52940916372963	0.31952046183259	1.69364697715343
	2.79499704501124	5.60000767929704	0.05182563467115	0.31714044960814
	3.05212922225546	5.64853846454917	0.02232672267673	0.15064873789249

and $S = 0$ and compared the numbers with those from Fukumoto & Hattori (2005), as shown in table 4.1 for $m = 0$ and table 4.2 for $m = 5$. Each row in the tables represents a mode of resonance between a $(m, m + 1)$ pair, while the first row corresponds to the first principal mode. The results agree very well with Fukumoto & Hattori (2005) for each of wavenumber m and principal modes.

4.4.1 Effect of density variations

In this section, we set surface tension to 0 and focus on the effect of density differences.

Heavy core: $\rho_2/\rho_1 > 1$

We first set examine $\rho_2/\rho_1 > 1$. In this case, the vortex ring core is denser than the fluid surrounding it (for instance Rayleigh–Taylor instability could create vortex rings when heavier fluid falls through a lighter fluid and rolls up; see e.g. Baker *et al.*, 1980; Joly *et al.*, 2005). The first five principal modes for the resonance between $(0, 1)$ and $(5, 6)$ are shown in figure 4.6(a), (b) respectively. For the $(0, 1)$ resonance pair, the first principal mode (blue) is most unstable. The growth rates of all five modes decrease sharply as ρ_2/ρ_1 increases from 1 to 1.2. The first, second (red) and fifth (green) principal modes then climb up and flat out as ρ_2/ρ_1 further increases to 100. The third (amber) principal mode has a stable region between $\rho_2/\rho_1 = 5.4$ and 9.8, while the fourth (purple) principal modes has a stable points at $\rho_2/\rho_1 = 1.8$.

For the resonance between the higher pair $(m, m+1) = (5, 6)$ shown in figure 4.6(b), the growth rate of all the modes increase between $\rho_2/\rho_1 = 1$ and 1.38, then remain almost constant beyond $\rho_2/\rho_1 = 2$. Hence a dense vortex core is more unstable than one with $\rho_2/\rho_1 = 1$.

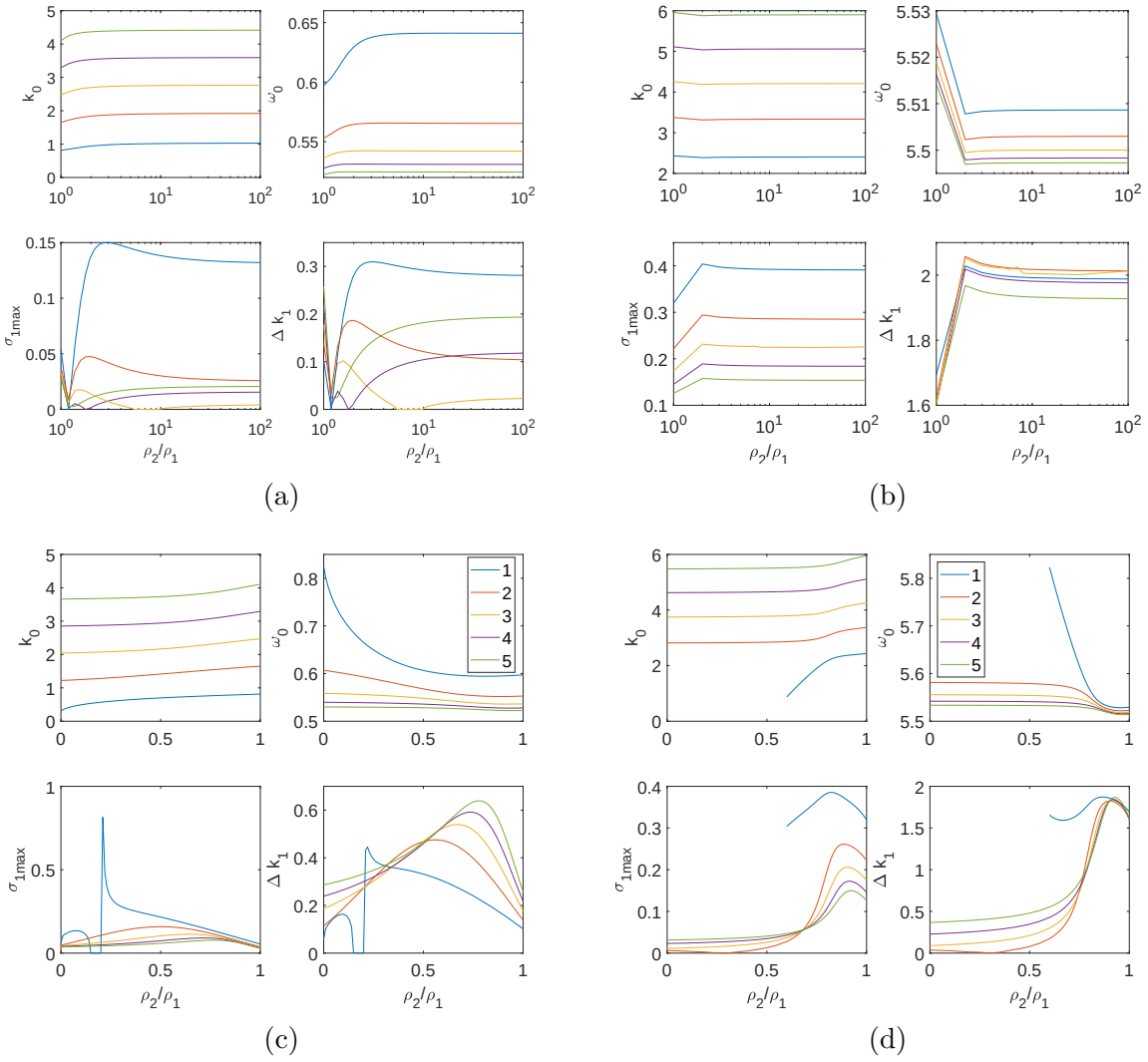

Figure 4.6: First five principal modes (k_0, ω_0) for $(a,\ c)$ $(0,1)$; $(b,\ d)$ $(5,6)$, the maximum growth rate σ_{1max} and the instability half-bandwidth Δk_1 are plotted versus density ratio ρ_2/ρ_1 between $(a,\ b)$ $[1,100]$; $(c,\ d)$ $[0,1]$. The first to fifth principal modes are blue, red, amber, purple and green curves.

Light core: $\rho_2/\rho_1 < 1$

We then set the density ratio ρ_2/ρ_1 between 0 and 1, where zero corresponds to a hollow core and one to for constant-density flow. For resonances between $m = 0$ and 1, we calculate the first five principal modes (see figure 4.6c). The plot shows that instability exists for the whole range of density ratios. The maximum growth rate of each principal mode exhibits a maximum value between $\rho_2/\rho_1 = 0.5$ and 0.8, except for the first principal mode (blue line) which has a maximum at $\rho_2/\rho_1 = 0.2$. The instability disappears for the first principal mode when the density ratio is between 0.15 and 0.2.

The calculation is extended to include more principal modes of the $(0, 1)$ pair with wavenumber k_0 up to 20 in figure 4.7(a). Each cross represents a principal mode and the spectrum is discrete. The dotted line connects the principal modes with the same density ratio. Note that for different curves, the value of k_0 of the same ith principal mode will vary because the position of principal mode shifts from case to case. The first five data points of each curve correspond to the first five principal modes we showed in figure 4.6(c). In general, the maximum growth rate σ_{1max} decreases as k_0 increases for all density ratios, and they all tend to a same value roughly 0.02487 for large k_0. The increase of instability half-bandwidth is almost linear in k_0.

For the higher wavenumber resonance pair for $m = 5$ and 6, the first five principal modes are shown in figure 4.6(d). The first principal mode only exists for a density ratio above 0.6 because the first cograde branch of the mode for $m = 5$ no longer crosses the first retrograde branch of the mode for $m = 6$, as discussed earlier in § 3. We can see that the first five principal modes have maxima of the growth rate near $\rho_2/\rho_1 = 0.8$–0.9. Compared to the the lower-mode resonance, e.g. $(0, 1)$, we see that the most unstable density ratio is closer to one for a higher value of $(m, m + 1)$ pair. The maximum of the growth rate is slightly greater for large m and the unstable half-bandwidth Δk_1 is much wider. We again extended the calculation for principal modes to $k_0 \leq 20$ in figure 4.7(b). The result

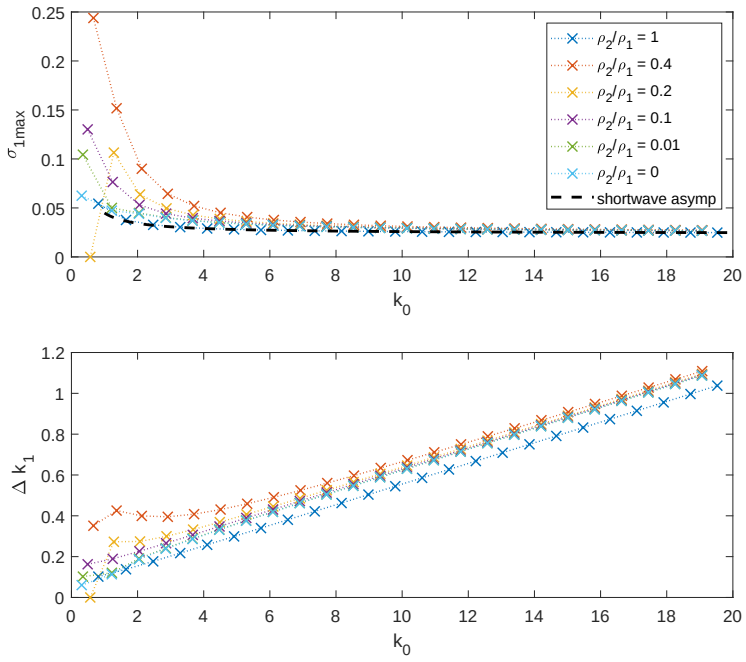

(a)

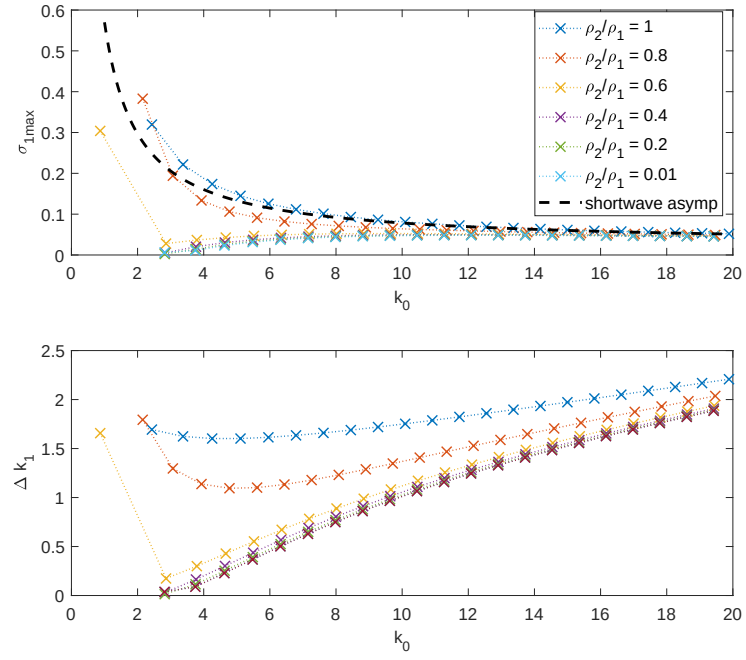

(b)

Figure 4.7: Maximum growth rate σ_{1max} and unstable half-bandwidth Δk_1 of principal modes $k_0 < 20$ for $(m, m+1) = (a)\ (0,1);\ (b)\ (5,6)$. The black dashed line is the short-wavelength asymptote (4.43) for $\rho_2/\rho_1 = 1$.

is very different compared to the $m = 0$ case. The largest maximum growth rate and widest unstable half-bandwidth appear at $\rho_2/\rho_1 = 1$. The first principal mode with the lowest k_0 is most unstable and the growth rate decays for higher principal modes. But for density ratios less than one, the first principal mode has the lowest maximum growth rate. The growth rate increases as k_0 increases and converges to a value of 0.04904 as for the case $\rho_2/\rho_1 = 1$. The unstable half-bandwidth also converge to a value close to that of $\rho_2/\rho_1 = 1$. The short-wavelength asymptote for the growth rate for the case of $\rho_2/\rho_1 = 1$, given in (5.1) of Fukumoto & Hattori (2005) as

$$\sigma_{1max} \approx \frac{15}{64\pi^2} + \frac{\sqrt{15}}{32k_0}\left[\frac{m}{\pi}\left(\frac{21}{8} + \frac{1}{\pi^2}\right) + \frac{1}{2}\left(-\frac{9\sqrt{15}}{64} + \frac{21}{8\pi} + \frac{\sqrt{15}}{16\pi^2} + \frac{1}{\pi^3}\right)\right], \qquad (4.43)$$

is plotted in black dashed line in figures 4.7 and 4.10.

In general, density difference affects the curvature instability of a vortex ring, but the change is only significant for the first few principal modes with smaller k_0. For large k_0, the maximum growth rate and the instability half-bandwidth converge to those for $\rho_2/\rho_1 = 1$. As pointed out by Fukumoto & Hattori (2005), local vortex stretching in the toroidal direction (along s) is the mechanism for short-wavelength instability. The stretching due to the local strain field is a kinematic mechanism so that should not be affected by density. For long waves, the possible reason for increasing instability is that the fore-aft symmetry of the vortex core is broken due to the distorted boundary (p. 87 in Fukumoto & Hattori, 2005). As shown in figure 4.8, the sausage-like distortion and the asymmetric pressure on the vortex boundary could result in a pressure distribution in s, and this nonuniform distribution of force acts to break up the ring. In the case of a vortex core that is lighter than the outside fluid, the acceleration by the exterior pressure is amplified because the same force is acting on a smaller mass (given the same volume of the core), and the vortex becomes more unstable.

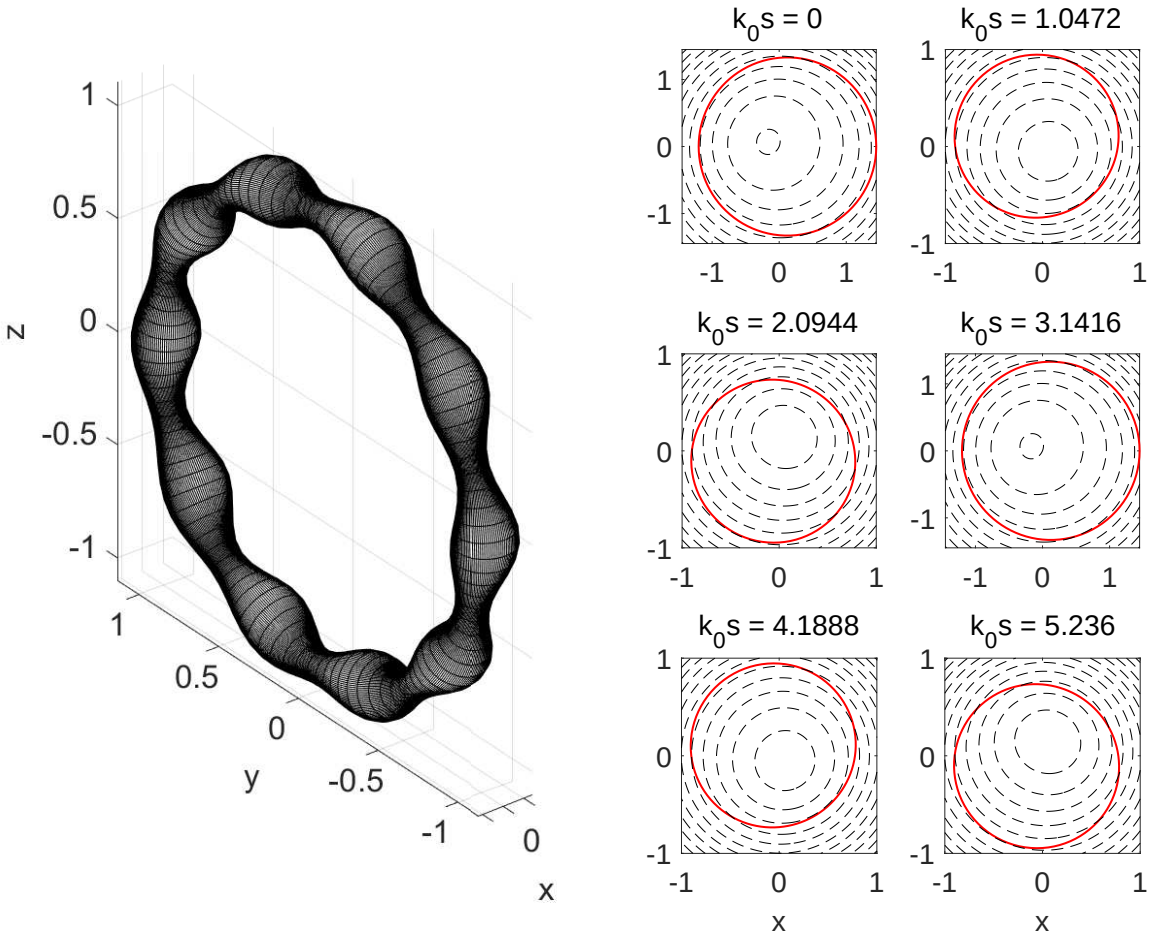

(a) (b)

Figure 4.8: (a) The shape of disturbed boundary for the first principal mode of the $(0,1)$ resonance at $(k_0, \omega_0) = (0.6647548585, 0.6183157195)$ and $\rho_2/\rho_1 = 0.4$; (b) pressure contours at different meridional crosssections $k_0 s$. Red curves are disturbed boundaries.

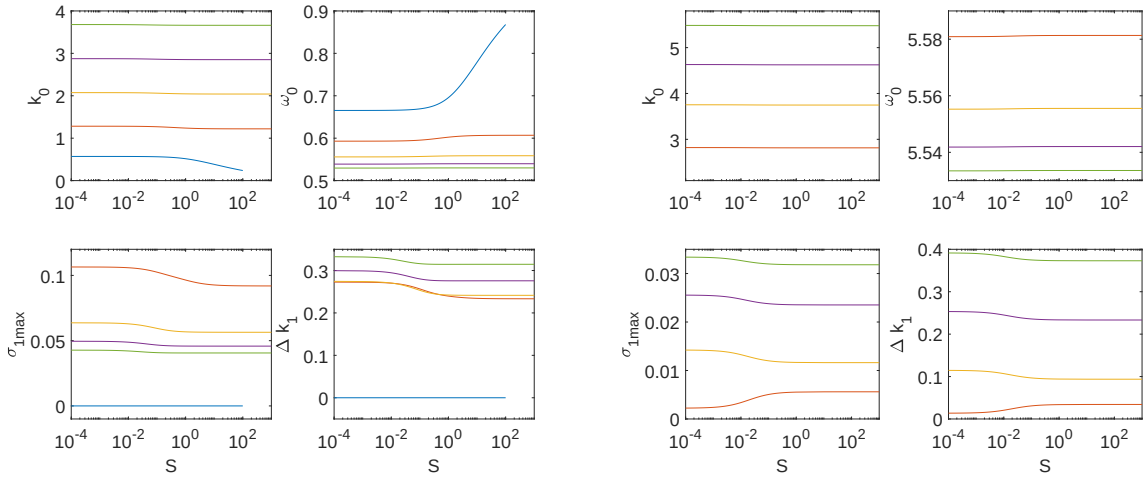

Figure 4.9: First five principal modes (k_0, ω_0) for (a) $(0,1)$; (b) $(5,6)$, the maximum growth rate σ_{1max} and the instability half-bandwidth Δk_1 are plotted versus surface tension S. $\rho_2/\rho_1 = 0.2$. The first to fifth principal modes are blue, red, amber, purple and green curves.

4.4.2 Surface tension

We now include surface tension S in the calculation. Adding surface tension introduces another degree of freedom into the parameter space. Calculations for the first five principal modes are shown in figure 4.9. In the $(0,1)$ case, the first principal mode (blue) is stable, while the growth rates of other four modes gradually decrease between $S = 10^{-2}$ and 1, and the second principal mode is the most unstable. The first principal mode disappears near $S = 100$ due to the isolation of the first cograde mode from the waves for $m = 0$ (cf. § 3). The first principal mode is absent in the $(5,6)$ resonance, again because of isolation. The growth rates of other four principal modes for the $(5,6)$ resonance vary when surface tension is less then 1 but become constant when S is greater than 1. Therefore, we pick two density ratios, $\rho_2/\rho_1 = 0.2$ and 0. Since (4.6) shows that results do not vary for $S > 1$, we now let surface tension varies from zero to one and examine the effect of different density ratios.

The $(0, 1)$ resonant pair with no surface tension is unstable for all density ratios except for the first principal mode of $\rho_2/\rho_1 = 0.2$ (see figure 4.7a). Adding surface tension does not change the growth rate significantly. The growth rate of the first few principal modes decrease slightly, but for $k_0 > 6$, the growth rates are identical with different surface tension. For the density ratio $\rho_2/\rho_1 = 0$, the principal modes with higher k_0 all have the same growth rate. On the other end of the spectrum for smaller k_0, the first principal mode becomes stabilised when $S = 1$, while the second principal mode has the largest growth rate.

A resonant pair of higher wavenumbers $(5, 6)$ is shown in figure 4.11. In both figure 4.11(a) and (b), surface tension barely changes the maximum growth rate and the unstable half-bandwidth.. In the short-wavelength regime, the curves for different values of surface tension collapse.

To summarise briefly from what we have demonstrated numerically: for resonant pairs with small $(m, m + 1)$, long waves with the smallest k_0 are most unstable and the growth rate decays to a constant for large k_0. The largest growth rate occurs approximately at $\rho_2/\rho_1 = 0.2$ for the most unstable mode, and other modes have maximum growth rate between $\rho_2/\rho_1 = 0.5$ and 1. Surface tension has a small influence on the instability. For a larger value of $(m, m+1)$ pairs, e.g. the $(5, 6)$ pair in figure 4.6(b), the instability is divided into two regimes around$\rho_2/\rho_1 = 0.68$: the principal mode with smallest wavenumber k_0 has the largest growth rate when the density ratio is above 0.68, while it has the lowest, but nonzero, growth rate when density ratio drops below 0.68. In both cases, the growth rates converge to the same value for short wavelengths, when the effect of surface tension is minimal.

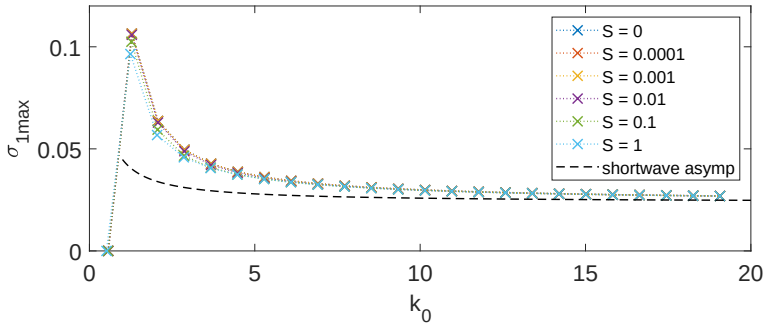

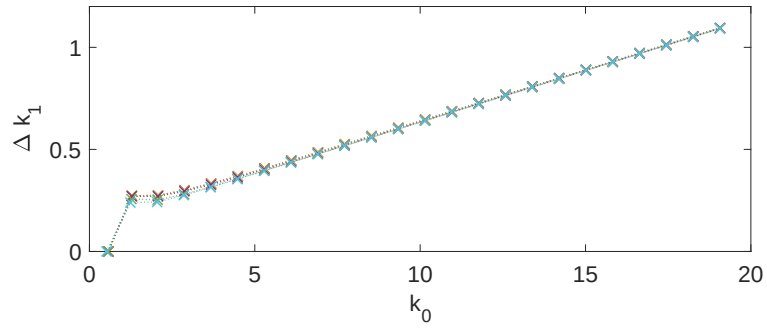

(a)

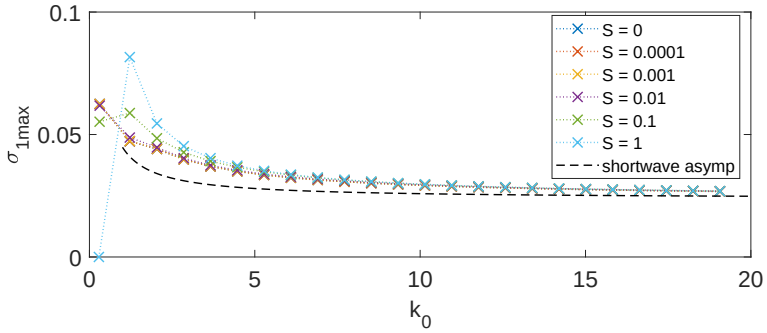

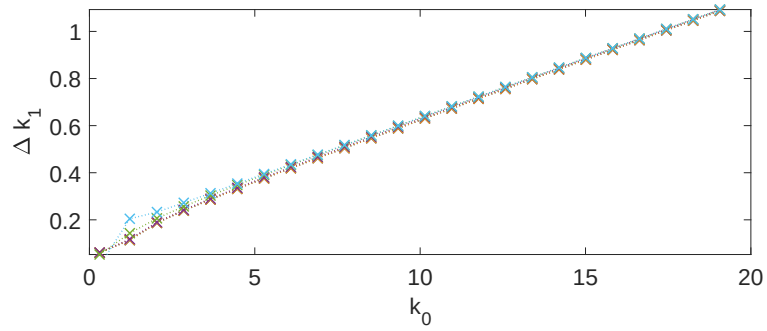

(b)

Figure 4.10: Maximum growth rate σ_{1max} and instability half-bandwidth Δk_1 for the $(0,1)$ resonance, (a) $\rho_2/\rho_1 = 0.2$ and (b) $\rho_2/\rho_1 = 0$. Surface tension, S, increases from 0 to 1. The black dashed line is the short-wavelength asymptote (4.43) for $\rho_2/\rho_1 = 1$ and $S = 0$.

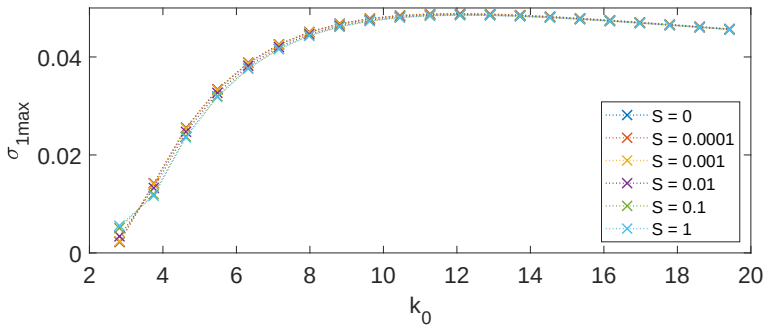

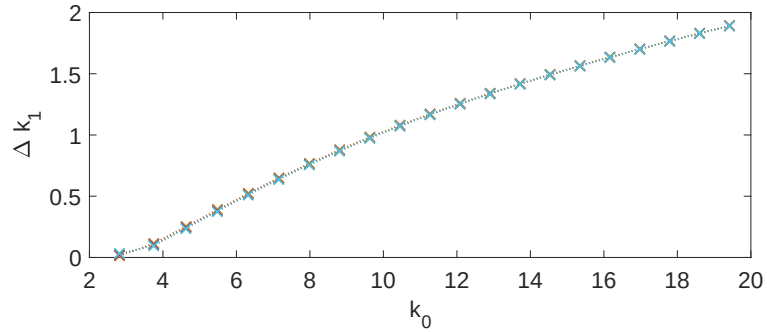

(a)

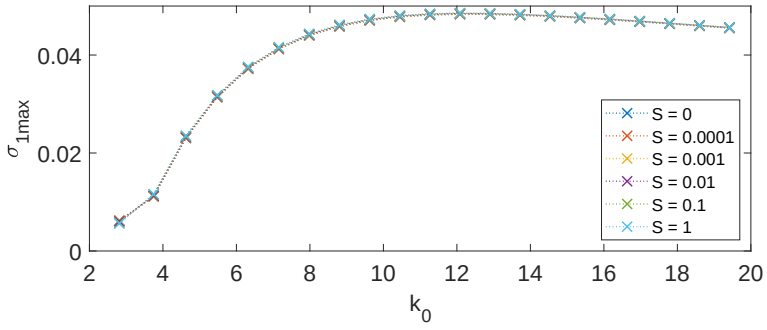

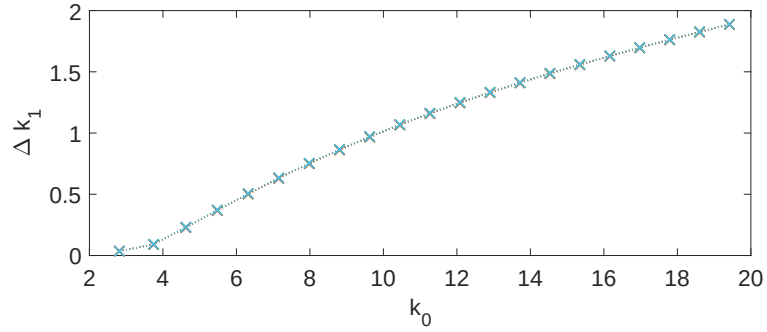

(b)

Figure 4.11: Maximum growth rate σ_{1max} and instability half-bandwidth Δk_1 for the $(5, 6)$ resonance, (a) $\rho_2/\rho_1 = 0.2$ and (b) $\rho_2/\rho_1 = 0$. Surface tension, S, increases from 0 to 1.

4.4.3 Wave energy

We calculate the energy of a resonant pair of Kelvin waves using Krein's theory of parametric resonance (see Krein, 1950; MacKay, 1986). The instability can be predicted by inspecting the energy of Kelvin waves without a calculation using the $O(\delta\epsilon)$ dispersion relation. A formula for the wave energy is given in Cairns (1979) and Fukumoto (2003):

$$E^{(m)} = -\frac{\pi}{2}\omega_0 \frac{\partial D}{\partial \omega_0}\left|f_0^{(m)}\right|^2, \tag{4.44}$$

where D is the dispersion relation obtained from (4.11) written in the form

$$D f_0^{(m)} \mathrm{e}^{\mathrm{i}(m\theta + ks - \omega t)} = 0. \tag{4.45}$$

Here

$$\begin{aligned} D =& (\omega_0 - m)^2 \left[\frac{\rho_2}{\rho_1} \frac{(\eta_1/k_0)^2 J_m(\eta_1)}{m\left(1 - \frac{2}{\omega_0 - m}\right) J_m(\eta_1) - \eta_1 J_{m+1}(\eta_1)} - \frac{K_m}{k_0 K_{m+1} - m K_m}\right] \\ &+ 1 - \frac{\rho_2}{\rho_1} + S(m^2 + k_0^2). \end{aligned} \tag{4.46}$$

This agrees with (7.6) in Fukumoto (2003) when $\rho_2/\rho_1 = 1$ and $S = 0$. (Fukumoto (2003) use the Bessel function of order $m-1$ in their formula while we use $m+1$, but the two are easily verified to be equivalent).

According to Krein's theory, the resonance between modes for m and $m+1$ is unstable if the cograde mode for the m waves and the retrograde mode for $m+1$ waves possess energies of opposite sign, since resonance between a positive-energy and a negative-energy wave is a necessary and sufficient conditions for instability (see Fukumoto & Hattori, 2005, §4.3). Figure 4.12 shows the first three cograde modes (solid red) and the first three retrograde modes (dashed blue) for $m = 5$, 6 and $\rho_2/\rho_1 = 0.1$. All the cograde modes of

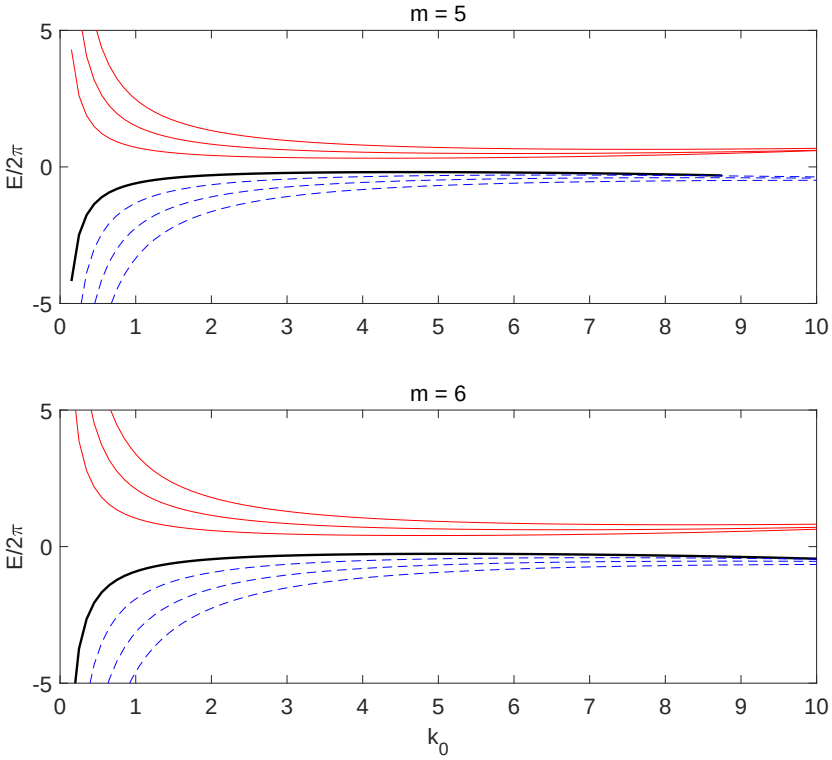

Figure 4.12: The energy of the first three cograde modes (solid) and the first three retrograde modes (dashed) of Kelvin waves for $m = 5$, 6. The solid thick line is the isolated mode.

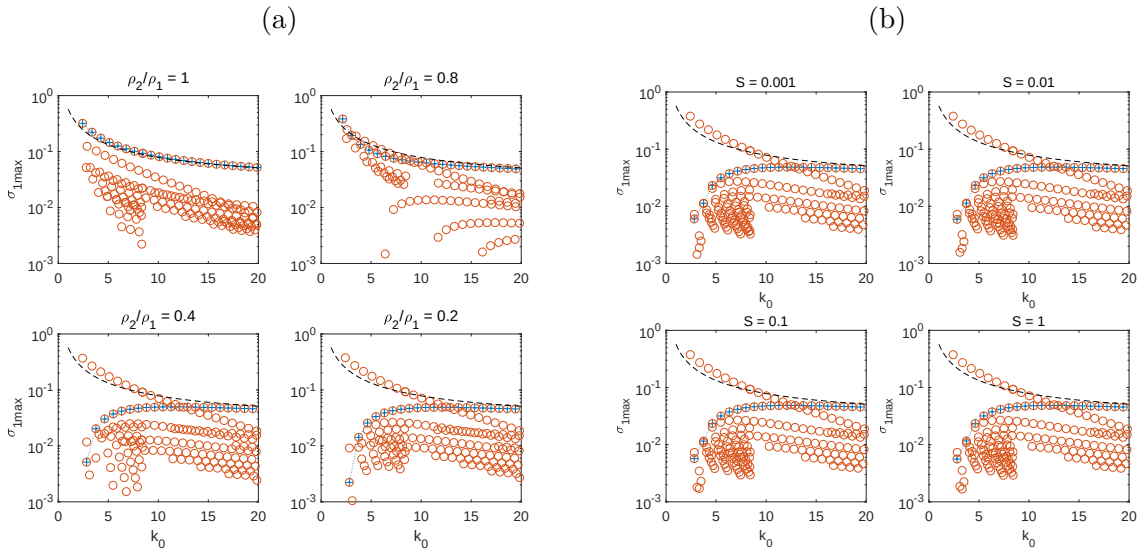

Figure 4.13: Maximum growth rate σ_{1max} for the modes of the $(5, 6)$ resonance with variations of (a) ρ_2/ρ_1; and (b) S. Principal modes are marked by blue crosses while other modes are red circles. The black dashed line is short-wavelength asymptotic (4.43) for $\rho_2/\rho_1 = 1$ and $S = 0$.

$m = 5$ have positive energy while all the retrograde modes of $m = 6$ have negative energy, therefore the first three principal modes created from their intersections are unstable.

4.4.4 Non-principal modes

As discussed in § 3 and demonstrated in figure 4.5, changing the value of $(\rho_2/\rho_1, S)$ from $(1, 0)$ leads to the isolation of the first cograde branch of Kelvin wave for wavenumber m. Once it migrates out of the region of $\omega_0 \in (m, m + 1)$, it no longer intersects the first retrograde branch of $m + 1$. As a result the first principal mode will no longer exist, so that the sequence of principal modes now starts with the second principal mode. Our discussion and calculations so far have been limited to those principal modes.

Growth rates for some non-principal modes are shown in figure 4.13. The nature of the instability changes with the isolation of the first cograde branch of Kelvin waves. The growth rates of principal modes are not always larger than that of non-principal modes for $\rho_2/\rho_1 = 0.8$ (figure 4.13a, top-right) as they were in the case of $\rho_2/\rho_1 = 1$ (top-left), but

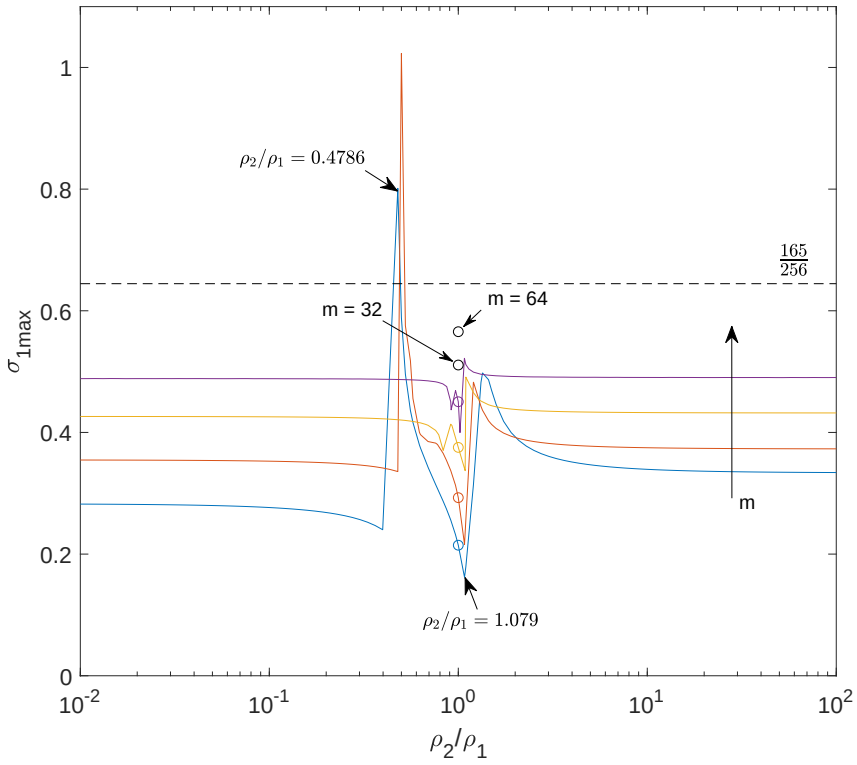

Figure 4.14: Maximum growth rate for modes with $\rho_2/\rho_1 \in [0.01, 100]$. Blue, red, amber and purple curves are for $m = 2$, 4, 8 and 16 respectively. The growth rate for $\rho_2/\rho_1 = 1$ is indicated by a circle. The dashed line is the value 165/256 when $m \to \infty$ from Fukumoto & Hattori (2005).

the first principal mode is still the most unstable. As ρ_2/ρ_1 diminishes further, the first principal mode disappears (figure 4.5) and the rest of principal modes are no longer the most unstable for smaller k_0, while remaining the most unstable in $k_0 \to 20$. The same trend can be seen in figure 4.13(b) for surface tension variation. The most unstable mode is the mode with the smallest value of k_0, no matter whether it belongs to the sequence of principal modes or not. This result indicates that a vortex ring is most unstable for the longest wavelength able to fit inside its circumference when subject to curvature instability given any pair of $(\rho_2/\rho_1, S)$.

The maximum growth rate for all modes is shown in figure 4.14 as functions of density ratio. The growth rate as $m \to \infty$ for $\rho_2/\rho_1 = 1$ from Fukumoto & Hattori (2005)

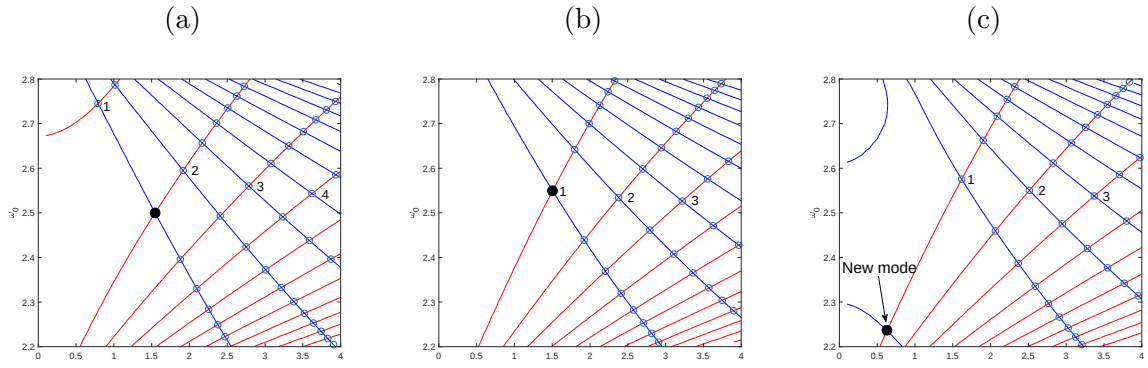

Figure 4.15: Intersection points of pair $(m, m+1) = (2, 3)$. (a) $\rho_2/\rho_1 = 0.4083$; (b) $\rho_2/\rho_1 = 1$ and (c) $\rho_2/\rho_1 = 1.2$. Principal modes are labeled by numbers; otherwise are non-principal modes. The black dot is the mode that has the largest growth rate. The most unstable mode switches from point 1 to the new mode causes the jump at $\rho_2/\rho_1 = 1.079$ in figure 4.14.

is $165/256 = 0.64453125$ (dashed line). In our calculation for $\rho_2/\rho_1 \neq 1$, the growth rate is not always bounded by that value. Taking $m = 2$ for example, a cusp at $\rho_2/\rho_1 = 0.4786$ can be observed in figure 4.14, where $\sigma_{1max} = 0.8013$. This can be related to the isolation of the first cograde mode from the other cograde modes for m (see figure 4.15 a, with the first cograde branch in the top left corner). As discussed in §3, the isolation made the first principal mode, i.e. the intersection point between the first cograde and the first retrograde modes, moves toward $\omega_0 = m + 1$. Once it has moved out of the domain $\omega_0 \in (m, m + 1)$, the first principal mode disappears and a non-principal mode has the largest growth rate. A steep drop of the curve to the left of the cusp in figure 4.14 correspond to this transition of the largest growth rate from a principal mode to a non-principal mode. Another steep elevation of growth rate is observed near $\rho_2/\rho_1 = 1.079$ because of a reversed version of the isolation: when ρ_2/ρ_1 increases beyond 1, the isolated branch for $m + 1$ wave migrates upward to its retrograde branches. In that case the isolated branch intersects with the cograde modes for m wave (see figure 4.15 c, with the isolated branch in the bottom left corner), which creates a new set of non-principal modes including one with the largest growth rate. The principal modes only possess the largest growth rate in the interval

between the two "cliffs" where $\rho_2/\rho_1 \in (0.4786, 1.079)$ in figure 4.14, and non-principal modes have the largest growth rate in the rest of the region.

For other waves with wavenumber $m > 2$, the growth rate as a function of ρ_2/ρ_1 is qualitatively similar. The growth rate for $m = 4$ has peak value 1.023 at $\rho_2/\rho_1 = 0.5$ for $m = 4$. The range of ρ_2/ρ_1 where a principal mode is most unstable becomes narrower as m increases. In the region away from the cusp, i.e. $\rho_2/\rho_1 < 0.1$, $\rho_2/\rho_1 > 10$ and $\rho_2/\rho_1 = 1$, the growth rate is independent of ρ_2/ρ_1 and gradually approaches the value of $165/256$ as m increases. To the right of the plot, where $\rho_2/\rho_1 > 10$, the growth rate is higher then that to the left, where $\rho_2/\rho_1 < 0.1$, e.g. $\sigma_{1max} = 0.3341$ at $\rho_2/\rho_1 = 100$ compared to 0.2822 at $\rho_2/\rho_1 = 0.01$, and they are both higher than 0.2146 at $\rho_2/\rho_1 = 1$ for $m = 2$. That indicates that a heavy core is more unstable than a light core. However, the difference shrinks as m increases: for $m = 8$, it is $\sigma_{1max} = 0.4903$ to 0.4885. The numerics were unable to resolve beyond wavenumber $m = 32$ except for $\rho_2/\rho_1 = 1$.

4.5 Conclusion

We have carried out a linear stability analysis to investigate the density and surface tension effects on a vortex ring, which is a generalisation of Fukumoto & Hattori (2005)'s calculations for $\rho_2/\rho_1 = 1$ and $S = 0$. Curvature instability for the principal modes of resonances between Kelvin waves for wavenumber m and $m + 1$ are calculated. In the long-wavelength regime $k_0 < 10$, the instability is enhanced for the symmetric ($m = 0$) and bending ($m = 1$) modes when $\rho_2/\rho_1 \neq 1$ but is suppressed for $m > 1$. Surface tension mitigates the instability for long waves, but the effect is minor. For the short-wavelength $k_0 > 10$, the effects of density and surface tension are minimal, and the principal modes are asymptotically similar to the case of $\rho_2/\rho_1 = 1$ and $S = 0$. For all the resonances, including principal and non-principal modes, the longest wavelength is the most unstable. The

principal modes are not guaranteed to be the most unstable modes for $(\rho_2/\rho_1, S) \neq (1, 0)$.

We have presented results for a wide range of values of ρ_2/ρ_1 and S. It is now of interest to consider the values of these quantities for real-world situations. These might include bubble rings in water, for which ρ_2/ρ_1 is about 0.001. Surface tension between water and air is 7.2×10^{-3} kg/s^2, and S depends on the strength of circulation Γ and the size of the ring. If we assume a thin bubble ring of diameter 1.5 m and core radius 1 cm that travels roughly at 2 m/s, S is of the order 1.8×10^{-4}. Another possible example is a vortex ring made of hot air or gases, possibly formed as a thermal. The core density depends on temperature: at 950°C, the density ratio is about 0.3. Surface tension is negligible under this circumstance. Our calculations indicate that both of these two cases are linearly unstable. The growth rate for principal modes in the former case is 0.09304, a 70% increase on the value 0.05434 for the $(\rho_2/\rho_1, S) = (1, 0)$ case; while the later example has a growth rate 0.2807, more than five times that of a constant-density ring.

The present work can be seen as a stepping stone to further stability analysis for a buoyant vortex ring which requires gravity in the formulation. In the present framework, we have made the "frozen-state" assumption for the linear stability problem, which is justified by arguing that the Froude number is larger than the order of $(\delta\epsilon)^{-1/2}$. It is well-known that a buoyant vortex propagates in an unsteady fashion (Turner, 1957; Pedley, 1968; Chang & Llewellyn Smith, 2018), so it is challenging to carry out a full analysis with gravity by the usual method of normal modes. We leave this approach to later, however, and continue with the present method to investigate density and surface tension effects on the MSTW instability in the following chapter.

Chapter 4, in full, has been submitted for publication of the material as it may appear in the Journal of Fluid Mechanics, "Density and surface tension effects on vortex ring stability. I Curvature instability" by C. Chang and S. G. Llewellyn Smith, 2020 (Cambridge University Press). The dissertation author was the primary investigator and

author of this material.

Chapter 5

Effects of density and surface tension on the Moore–Saffman–Tsai–Widnall instability of a strained vortex

The Moore–Saffman–Tsai–Widnall (MSTW) instability is a parametric instability that arises in strained vortex columns. The strength of the strain is assumed weak and is perpendicular to the vortex axis, and introduced as a small perturbation. In this chapter of our investigation on vortex instability with effects of density and surface tension, a linear stability analysis for this situation. The instability is caused by resonance between two Kelvin waves with azimuthal wavenumber separated by 2. The density ratio is defined as ρ_1/ρ_2, the ratio of vortex to ambient fluid. The dispersion relations for Kelvin waves and resonant modes are obtained by solving the governin equations. Results show that the stationary resonant waves for $m = \pm 1$ are more unstable when the density ratio approaches zero, while the growth rate is maximised near $\rho_2/\rho_1 = 0.215$ for the resonance $(m, m+2) = (0, 2)$. Surface tension suppresses the instability, but its effect is less significant compared to that of density. As the azimuthal wavenumbers m increases, the MSTW instability

decays in contrast with the curvature instability examined in the previous chapter.

5.1 Introduction

This chapter continues the study on the effects of density and surface tension on vortex stability. A linear stability analysis is carried out and parametric instabilities are investigated. A possible mechanism of instability was proposed by Widnall *et al.* (1974) in their study on vortex ring stability. These authors argued that a basic state solution subject to neutrally stable disturbances $\tilde{u}$ of $O(\delta)$, $\delta \ll 1$, can be unstable with the addition of another physical effect represented by a parameter ϵ. The solution is then expanded as a perturbation series in ϵ, setting the stage for possible resonance between two neutrally stable $O(\delta)$ modes. The resonant instability appears consequently at $O(\delta\epsilon)$ and is called parametric instability.

Two types of parametric instabilities have been discovered for vortices: the Moore–Saffman–Tsai–Widnall instability and the curvature instability. The former, abbreviated to MSTW instability, was first discovered by Moore & Saffman (1975) and Tsai & Widnall (1976), and has since been revisited by Fukumoto (2003) among others. The basic state is a vortex column with uniform vorticity inside the column and zero outside the column. It is hence a Rankine vortex that extends uniformly in the third dimension. Linear analysis shows that the $O(1)$ vortex column is neutrally stable when disturbed by waves of $O(\delta)$. Those $O(\delta)$ disturbances are Kelvin waves. Movivated by the goal of examining vortex ring stability, weak strain, measured by the small parameter γ (rather than ϵ). This situation leads to the MSTW instability, which is the focus of the present work. This is an approximation to the vortex ring case with no basic-state curvature, but with the leading-order strain retained. In the curvature instability studied in the previous chapter, the basic state is expanded in terms of the ratio of the core size of the vortex ring to its

radius of curvature and is curved at $O(\epsilon)$.

Moore & Saffman (1975); Tsai & Widnall (1976) found that when a weak strain field is imposed on the vortex perpendicular to its axis, an instability emerges due to the strain field. The strain field is mathematically a quadrupole, and enables a resonance between two Kelvin waves of azimuthal wavenumber m and $m+2$. The MSTW instability has been studied extensively since then, e.g. Eloy & Le Dizès (2001); Fukumoto (2003). In the short wavelength regime, it has shown to be the elliptic instability of Bayly (1986); Waleffe (1990); Leweke & Williamson (1998). Blanco-Rodriguez & Le Dizès (2016) has theoretically studied the short wave elliptic instability of a Batchelor vortex (a Gaussian core). A recent study of direct numerical simulations (DNS) by Hattori *et al.* (2019) has shown that both type of parametric instabilities exist in the short-wavelength regime, and that the elliptic instability dominates over the curvature instabilities.

The stability of a strained vortex column was also investigated in the context of aircraft trailing vortices. The mutual interaction between long waves causes the Crow instability (Crow, 1970). The Biot–Savart law is used to compute the induced velocity on one of the trailing vortices due to the presence of the other. In a frame fixed to one of the vortices, a weak strain field is created by the other vortex in the thin-core limit providing their seapration is large. Moore & Saffman (1971) obtained a solution represented as a perturbation series in γ, where $\gamma \ll 1$ is the strength of the strain field. The core boundary deforms into elliptic shape at $O(\gamma)$,

$$F = 1 + \frac{1}{2}\gamma \cos 2\theta + O(\gamma^2). \tag{5.1}$$

The stability of the strained vortex was also investigated by Moore & Saffman (1971) for twp-dimensional and three-dimensional long-wave disturbances. Moore & Saffman (1975) and Tsai & Widnall (1976) studied the instability mechanism proposed by Widnall *et al.*

(1974) for short-wave disturbances. Fukumoto (2003) extended the stability calculation for intersection points of Kelvin wave dispersion curves.

Historically, the curvature instability (Hattori & Fukumoto, 2003; Fukumoto & Hattori, 2005) was discovered later than the MSTW instability. We have studied it with the effects of density and surface tension in the previous chapter (see also Chang & Llewellyn Smith, 2020). In the asymptotic analysis by Fukumoto & Hattori (2005), the authors argued that the curvature instability dominates over the MSTW instability provided that $\epsilon \ll 1$. However, in the recent numerical simulations by Hattori *et al.* (2019), the elliptic instability (short-wavelength MSTW) is found to be dominant for a vortex ring with or without swirl, and the curvature instability is only detected when swirl is present.

We follow the formulation in Tsai & Widnall (1976) and Fukumoto (2003) but include density and surface tension. In §,5.2, the mathematical formulation including governing equations, boundary conditions, and the basic state solution are given. Linearised equations at $O(\delta)$ and $O(\delta\epsilon)$ are also derived. The solutions at both orders with density and surface tension are discussed in §,3. We shownthe result for stationary resonance between $(m, m+2) = (-1, 1)$ in §,5.4, followed by resonance for $m \geq 0$ in §,5.5. We conclude in §,5.6.

5.2 Formulation

Two thin parallel vortex tubes are considered, as shown in figure 5.1(a). We assume that $\gamma = a/D \ll 1$, where a is the core size and R the separation between tubes. The outer region and the vortical cores have constant densities ρ_1 and ρ_2 respectively. The circulation of the core is Γ for both vortices but with opposite sign. We nondimensionalise the problem using length scale a, velocity scale $U_c = \Gamma/(2\pi a)$, and time scale $2\pi a^2/\Gamma$, while the pressure scale is taken to be $\rho_2(\Gamma/2\pi a)^2$. The velocity potential describing the

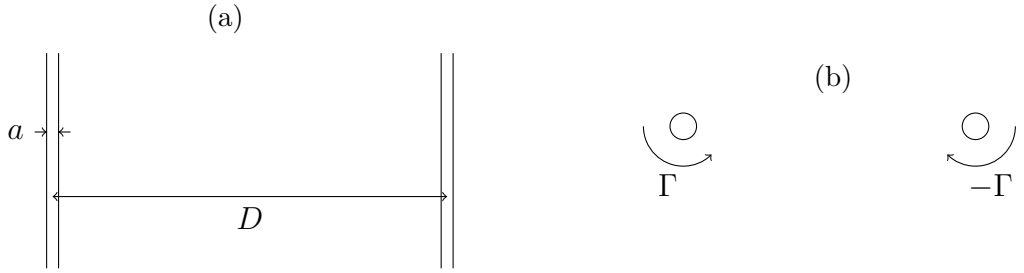

Figure 5.1: (a) Side view of two parallel vortex tubes and (b) top view of the counter-rotating vortices.

outer irrotational flow is scaled by $\Gamma/2\pi$.

Each vortex tube experiences a strain field perpendicular to its centerline. This is due to the induction of the other vortex tube. The strain is a quadrupole field of strength $O(\gamma)$. We focus on the vortex on the left, with cylindrical coordinates (r, θ, z) centered in it (see figure 5.1b). This model can be seen as an approximation for a vortex ring with curvature ϵ, with γ representing the local effect of the curvature of the other half of the vortex ring. We work to $O(\gamma)$ in the following formulation.

5.2.1 Governing equations

We use cylindrical coordinates (r, θ, z), with velocity $\mathbf{u} = (u, v, w)$. The undisturbed core boundary is taken to be $r = 1$. Since the core is rotational, the governing equations are the Euler equations (4.2) inside the vortex core; and the Laplace equation (4.3) for a velocity potential in the irrotational region outside.

In cylindrical coordinates the Euler equations are

$$\frac{\partial u}{\partial t} + \mathbf{u} \cdot \boldsymbol{\nabla} u - \frac{v^2}{r} = -\frac{\partial p}{\partial r}, \tag{5.2}$$

$$\frac{\partial v}{\partial t} + \mathbf{u} \cdot \boldsymbol{\nabla} v + \frac{uv}{r} = -\frac{1}{r}\frac{\partial p}{\partial \theta}, \tag{5.3}$$

$$\frac{\partial w}{\partial t} + \mathbf{u} \cdot \boldsymbol{\nabla} w = -\frac{\partial p}{\partial z}, \tag{5.4}$$

where

$$\mathbf{u}\cdot\boldsymbol{\nabla} = u\frac{\partial}{\partial r} + \frac{v}{r}\frac{\partial}{\partial \theta} + w\frac{\partial}{\partial z}. \tag{5.5}$$

The continuity equation is

$$\frac{1}{r}\frac{\partial}{\partial r}(ru) + \frac{1}{r}\frac{\partial v}{\partial \theta} + \frac{\partial w}{\partial z} = 0. \tag{5.6}$$

Outside the core, Laplace's equation is

$$\frac{1}{r}\frac{\partial}{\partial r}\left(r\frac{\partial \Phi}{\partial r}\right) + \frac{1}{r^2}\frac{\partial^2 \Phi}{\partial \theta^2} + \frac{\partial^2 \Phi}{\partial z^2} = 0. \tag{5.7}$$

The solution for (5.2) and (5.6) is called the inner solution, while the outer solution refers to the solution of (5.7).

5.2.2 Boundary conditions

The boundary of the vortex is taken to be $r = F$, where $F(\theta;\gamma)$ will be obtained as part of the solution. The inner and outer solutions are matched on the core boundary where $r = F$. For inviscid flows, the matching are given by the kinematic and the dynamic conditions. These conditions are given by (4.10) and (4.11) in §, 4.2.2.

5.2.3 The mean flow solution

This solution (written using uppercase letters) can be obtained as a perturbation series in γ:

$$\boldsymbol{U} = \boldsymbol{U}_0 + \gamma\boldsymbol{U}_1 + \cdots, \quad P = P_0 + \gamma P_1 + \cdots, \quad \Phi = \Phi_0 + \gamma\Phi_1 + \cdots, \tag{5.8}$$

where γ is the strength of the strain field.

The leading-order mean flow solution is the Rankine vortex which is given in (4.13)

and (4.14). The strain field leads to the following $O(\gamma)$ solution of the mean flow (cf. the solution in Moore & Saffman, 1971):

$$U_1 = -r\sin 2\theta, \qquad V_1 = -r\cos 2\theta, \qquad P_1 = 0 \tag{5.9}$$

in the inner region, while the outer solution is

$$\Phi_1 = \frac{1}{8}\left[\frac{3}{r^2} - r^2 - \frac{\rho_2}{\rho_1}\left(\frac{1}{r^2} + r^2\right) + 3S\left(\frac{1}{r^2} + r^2\right)\right]\sin 2\theta. \tag{5.10}$$

The shape of the boundary to $O(\gamma)$ is

$$F(\theta;\gamma) = F_0 + \gamma F_1 + \cdots = 1 + \gamma\frac{1}{2}\cos 2\theta + O(\gamma^2). \tag{5.11}$$

See appendix B.1.2 for the detailed calculations leading to (5.9)–(5.11).

5.2.4 Linearised equations and boundary conditions for infinitesimal disturbances

We disturb the mean flow that derived in § 5.2.3,

$$U + \tilde{u}, \quad V + \tilde{v}, \quad W + \tilde{w}, \quad P + \tilde{p}, \quad \Phi + \tilde{\phi}, \tag{5.12}$$

and the disturbed boundary is $r = F + \tilde{f}$. The disturbances are assumed to be of $O(\delta)$ compared to the $O(1)$ basic state with $\delta \ll 1$. The usual stability analysis treats $O(\delta)$ disturbances. Here these are neutrally stable, and it is the $O(\delta\gamma)$ solution that is of interest for parametric instability.The disturbances are decomposed into normal modes in s and t. We use tildes over lowercase letters to represent the disturbances. As with the basic

solution, they are expanded in γ as

$$\tilde{\mathbf{u}} = (\tilde{\mathbf{u}}_0 + \gamma\tilde{\mathbf{u}}_1 + \cdots)\mathrm{e}^{\mathrm{i}(kz-\omega t)}, \tag{5.13}$$

$$\tilde{p} = (\tilde{p}_0 + \gamma\tilde{p}_1 + \cdots)\mathrm{e}^{\mathrm{i}(kz-\omega t)}, \tag{5.14}$$

$$\tilde{\phi} = (\tilde{\phi}_0 + \gamma\tilde{\phi}_1 + \cdots)\mathrm{e}^{\mathrm{i}(kz-\omega t)}. \tag{5.15}$$

The wavenumber and the frequency are also expanded as

$$k = k_0 + \gamma k_1 + \cdots, \qquad \omega = \omega_0 + \gamma\omega_1 + \cdots. \tag{5.16}$$

The core boundary disturbance is

$$\tilde{f} = (\tilde{f}_0 + \gamma\tilde{f}_1 + \cdots)\mathrm{e}^{\mathrm{i}(kz-\omega t)}. \tag{5.17}$$

Since the disturbances $(\tilde{\mathbf{u}}, \tilde{p}, \tilde{\phi})$ are small compared to the basic solution $(\boldsymbol{U}, P, \Phi)$, (5.2)–(5.7) can investigated at $O(\delta)$ and $O(\delta\gamma)$ in what follows.

$O(\delta)$ linearised equations and boundary conditions

The linearised equations for disturbances at $O(\delta)$ are

$$-\mathrm{i}\omega_0\tilde{u}_0 + \frac{V_0}{r}\frac{\partial\tilde{u}_0}{\partial\theta} - \frac{2V_0\tilde{v}_0}{r} = -\frac{\partial\tilde{p}_0}{\partial r}, \tag{5.18}$$

$$-\mathrm{i}\omega_0\tilde{v}_0 + \tilde{u}_0\frac{\partial V_0}{\partial r} + \frac{V_0}{r}\frac{\partial\tilde{v}_0}{\partial\theta} + \frac{V_0\tilde{u}_0}{r} = -\frac{1}{r}\frac{\partial\tilde{p}_0}{\partial\theta}, \tag{5.19}$$

$$-\mathrm{i}\omega_0\tilde{w}_0 + \frac{V_0}{r}\frac{\partial\tilde{w}_0}{\partial\theta} = -\mathrm{i}k_0\tilde{p}_0, \tag{5.20}$$

$$\frac{1}{r}\frac{\partial}{\partial r}(r\tilde{u}_0) + \frac{1}{r}\frac{\partial\tilde{v}_0}{\partial\theta} + \mathrm{i}k_0\tilde{w}_0 = 0 \tag{5.21}$$

for the inside and

$$\frac{1}{r}\frac{\partial}{\partial r}\left(r\frac{\partial\tilde{\phi}_0}{\partial r}\right)+\frac{1}{r^2}\frac{\partial^2\tilde{\phi}_0}{\partial\theta^2}-k_0^2\tilde{\phi}_0=0 \tag{5.22}$$

for the outside. The linearised boundary conditions at $r=1$ are

$$-\mathrm{i}\omega_0\tilde{f}_0+\frac{\partial\tilde{f}_0}{\partial\theta}=\tilde{u}_0, \tag{5.23}$$

$$\tilde{u}_0=\frac{\partial\tilde{\phi}_0}{\partial r}, \tag{5.24}$$

$$\frac{\rho_2}{\rho_1}\tilde{p}_0-\mathrm{i}\omega_0\tilde{\phi}_0+\frac{\partial\tilde{\phi}_0}{\partial\theta}=\left(1-\frac{\rho_2}{\rho_1}\right)\tilde{f}_0-S\left(\frac{\partial^2\tilde{f}_0}{\partial\theta^2}-k_0^2\tilde{f}_0\right). \tag{5.25}$$

The solutions are Kelvin waves given in appendix B.2.

$O(\delta\gamma)$ linearised equations and boundary conditions

We proceed to the next order in the expansion in γ. The equations for disturbances of $O(\delta\gamma)$ are also linearised. The inner solution satisfies

$$\begin{aligned}-\mathrm{i}\omega_0\tilde{u}_1+\frac{\partial\tilde{u}_1}{\partial\theta}-2\tilde{v}_1+\frac{\partial\tilde{p}_1}{\partial r}&=\left(\mathrm{i}\omega_1-\frac{\partial U_1}{\partial r}\right)\tilde{u}_0-U_1\frac{\partial\tilde{u}_0}{\partial r}-\frac{V_1}{r}\frac{\partial\tilde{u}_0}{\partial\theta}\\&\quad-\left(\frac{1}{r}\frac{\partial U_1}{\partial\theta}-\frac{2V_1}{r}\right)\tilde{v}_0,\end{aligned} \tag{5.26}$$

$$\begin{aligned}-\mathrm{i}\omega_0\tilde{v}_1+2\tilde{u}_1+\frac{\partial\tilde{v}_1}{\partial\theta}+\frac{1}{r}\frac{\partial\tilde{p}_1}{\partial\theta}&=\left(\mathrm{i}\omega_1-\frac{1}{r}\frac{\partial V_1}{\partial\theta}-\frac{U_1}{r}\right)\tilde{v}_0-U_1\frac{\partial\tilde{v}_0}{\partial r}-\frac{V_1}{r}\frac{\partial\tilde{v}_0}{\partial\theta}\\&\quad-\left(\frac{\partial V_1}{\partial r}+\frac{V_1}{r}\right)\tilde{u}_0,\end{aligned} \tag{5.27}$$

$$-\mathrm{i}\omega_0\tilde{w}_1+\frac{\partial\tilde{w}_1}{\partial\theta}+\mathrm{i}k_0\tilde{p}_1=-\mathrm{i}k_1\tilde{p}_0+\mathrm{i}\omega_1\tilde{w}_0-U_1\frac{\partial\tilde{w}_0}{\partial r}-\frac{V_1}{r}\frac{\partial\tilde{w}_0}{\partial\theta} \tag{5.28}$$

with the continuity equation

$$\frac{\partial\tilde{u}_1}{\partial r}+\frac{\tilde{u}_1}{r}+\frac{1}{r}\frac{\partial\tilde{v}_1}{\partial\theta}+\mathrm{i}k_0\tilde{w}_1=-\mathrm{i}k_1\tilde{w}_0. \tag{5.29}$$

The velocity potential outside satisfies

$$\frac{\partial^2\tilde{\phi}_1}{\partial r^2}+\frac{1}{r}\frac{\partial\tilde{\phi}_1}{\partial r}+\frac{1}{r^2}\frac{\partial^2\tilde{\phi}_1}{\partial\theta^2}-k_0^2\tilde{\phi}_1=2k_0k_1\tilde{\phi}_0. \tag{5.30}$$

The linearised kinematic boundary conditions at $r=1$ are

$$-\mathrm{i}\omega_0\tilde{f}_1+\frac{\partial\tilde{f}_1}{\partial\theta}-\tilde{u}_1=\mathrm{i}\omega_1\tilde{f}_0-V_1\frac{\partial\tilde{f}_0}{\partial\theta}-\frac{\mathrm{d}F_1}{\mathrm{d}\theta}\tilde{v}_0+\frac{\partial U_1}{\partial r}\tilde{f}_0+F_1\frac{\partial\tilde{u}_0}{\partial r}, \tag{5.31}$$

$$\begin{aligned}\tilde{u}_1-\frac{\partial\tilde{\phi}_1}{\partial r}=&\left(-\frac{\partial\Phi_1}{\partial\theta}+V_1\right)\frac{\partial\tilde{f}_0}{\partial\theta}+\left(2\frac{\mathrm{d}F_1}{\mathrm{d}\theta}+\frac{\partial^2\Phi_1}{\partial r^2}-\frac{\partial U_1}{\partial r}\right)\tilde{f}_0\\&+\frac{\mathrm{d}F_1}{\mathrm{d}\theta}\left(\tilde{v}_0-\frac{\partial\tilde{\phi}_0}{\partial\theta}\right)+F_1\left(2\frac{\partial\tilde{f}_0}{\partial\theta}+\frac{\partial^2\tilde{\phi}_0}{\partial r^2}-\frac{\partial\tilde{u}_0}{\partial r}\right),\end{aligned} \tag{5.32}$$

The linearised dynamic condition at $r=1$ is

$$\begin{aligned}\frac{\rho_2}{\rho_1}\tilde{p}_1-\mathrm{i}\omega_0\tilde{\phi}_1+\frac{\partial\tilde{\phi}_1}{\partial\theta}=&\mathrm{i}\omega_1\tilde{\phi}_0-\frac{\partial\Phi_1}{\partial r}\frac{\partial\tilde{\phi}_0}{\partial r}-\frac{\partial\Phi_1}{\partial\theta}\frac{\partial\tilde{\phi}_0}{\partial\theta}+\left(1-\frac{\rho_2}{\rho_1}\right)\tilde{f}_1\\&+\left(2\frac{\partial\Phi_1}{\partial\theta}-\frac{\partial^2\Phi_1}{\partial r\partial\theta}\right)\tilde{f}_0-F_1\left[\frac{\rho_2}{\rho_1}\frac{\partial\tilde{p}_0}{\partial r}-\mathrm{i}\omega_0\frac{\partial\tilde{\phi}_0}{\partial r}+\frac{\partial^2\tilde{\phi}_0}{\partial r\partial\theta}-2\frac{\partial\tilde{\phi}_0}{\partial\theta}\right]\\&-F_1\left[\frac{\rho_2}{\rho_1}\frac{\partial^2P_0}{\partial r^2}+3\left(\frac{\partial\Phi_0}{\partial\theta}\right)^2\right]\tilde{f}_0\\&-S\left(\frac{\partial^2\tilde{f}_1}{\partial\theta^2}-k_0^2\tilde{f}_1-2k_0k_1\tilde{f}_0-2F_1\frac{\partial^2\tilde{f}_0}{\partial\theta^2}\right).\end{aligned} \tag{5.33}$$

Solutions for the disturbance waves at $O(\delta)$ and $O(\delta\gamma)$ are given in the next section. The dispersion relation is obtained by matching the boundary conditions.

5.3 Solutions

Solutions for both $O(\delta)$ and $O(\delta\gamma)$ disturbance waves are written as

$$\tilde{\mathbf{u}}(r,\theta) = \mathbf{u}^{(m)}(r)\mathrm{e}^{\mathrm{i}m\theta}, \quad \tilde{p}(r,\theta) = p^{(m)}(r)\mathrm{e}^{\mathrm{i}m\theta}, \quad \tilde{\phi}(r,\theta) = \phi^{(m)}(r)\mathrm{e}^{\mathrm{i}m\theta}, \tag{5.34}$$

where m is the azimuthal wavenumber. The resonance condition is when two Kelvin waves of azimuthal wavenumber differing by 2 are coupled by the quadrupole at $O(\delta)$. The solutions at $O(\delta)$ and $O(\delta\gamma)$ are written as m and $m+2$ waves.

5.3.1 Kelvin waves at $O(\delta)$

The solution at $O(\delta)$ is a Kelvin wave, which is described in appendix B.2. The Kelvin waves are coupled with the quadrupole field (5.9) through the right-hand sides of (5.26)–(5.28). When two Kelvin waves with wavenumber m and $m+2$ appear in the forcing terms on the right-hand side of (5.26)–(5.28), the solution at the $O(\delta\gamma)$ will possess modes for $m-2$, m, $m+2$ and $m+4$. The resonances are between pairs of two adjacent modes separated by 2. We focus on the resonance between a pair of Kelvin waves $(m, m+2)$ in this study, since the cases for $(m-2, m)$, $(m+2, m+4)$ can be inferred by using different value of m.

The solution (B.16) and (B.18) contains coefficients (Kelvin wave amplitudes) α_0 and β_0 that are determined using the boundary conditions. The boundary conditions for wavenumber m become

$$-\mathrm{i}(\omega_0 - m)f_0^{(m)} = u_0^{(m)} = \frac{\mathrm{d}\phi_0{}^{(m)}}{\mathrm{d}r}, \tag{5.35}$$

$$\frac{\rho_2}{\rho_1}p_0^{(m)} - \mathrm{i}(\omega_0 - m)\phi_0^{(m)} = \left(1 - \frac{\rho_2}{\rho_1}\right) f_0^{(m)} + S(m^2 + k_0^2)f_0^{(m)}. \tag{5.36}$$

Substituting $p_0^{(m)}$, $u_0^{(m)}$, $\phi_0^{(m)}$ and $f_0^{(m)}$ (see appendix B.2) into the equations above, we

obtain a set of homogeneous linear equations for $\alpha_0^{(m)}$ and $\beta_0^{(m)}$. For non-trivial $\alpha_0^{(m)}$ and $\beta_0^{(m)}$, the determinant must be zero, which gives the dispersion relation for mode m in (4.41) (see §, 4.3). For the second set of Kelvin waves, the wavenumber is $m+2$ in the MSTW instability instead of $m+1$ in the curvature calculation. The boundary conditions are the same formulas as in (5.36) except that m is replaced by $m+2$, and similarly for the solution in appendix B.2. Using the boundary conditions and the solution for the $m+2$-mode, we obtain the dispersion relation

$$\left[1-\frac{E_2}{(\omega_0-m-2)^2}\left(m+2+k_0\frac{K_{m+1}(k_0)}{K_{m+2}(k_0)}\right)\right]J_{m+1}(\eta_2)=\left\{-(m+2)\frac{\omega_0-m-2}{\omega_0-m-4}\right.$$
$$\left.+\left[\frac{\rho_2}{\rho_1}+E_2\frac{m+2}{(\omega_0-m-2)(\omega_0-m-4)}\right]\left(m+2+k_0\frac{K_{m+1}(k_0)}{K_{m+2}(k_0)}\right)\right\}\frac{\eta_2}{k_0^2}\,J_{m+2}(\eta_2), \quad (5.37)$$

where $E_2=1-\rho_2/\rho_1+S[k_0^2+(m+2)^2]$ and η_2 is the radial wavenumber for $m+2$.

The intersection points between the two sets of Kelvin waves give possible candidates for parametric instability. The actual modes can be found by finding the roots for (4.41) and (5.37) with $\omega_0\in[m,m+2]$. For Kelvin waves with wavenumber m, there are cograde branches going upward where $\omega_0>m$ and retrograde branches going downward where $\omega_0<m$ (see figure 5.2 for $m=2$). The cograde branches are labeled from top as the 1st, 2nd, ... cograde modes, while the retrograde branches are labeled from the bottom. The cograde branches of the m waves and the retrograde branches of the $m+2$ waves cross in $\omega_0\in[m,m+2]$ setting up possible modes for resonance. We follow the definition in Fukumoto (2003) for the case of $(\rho_2/\rho_1,S)=(1,0)$. The principal modes are the intersection point of the first cograde branch for m and the isolated branch for $m+2$, and also the intersection points of the $i+1$-th cograde branches for m and the i-th retrograde branches for $m+2$. This definition is slightly different from that in § 4.3 for the curvature instability, where the cograde branches for m never cross the isolated branch for $m+1$ when $(\rho_2/\rho_1,S)=(1,0)$.

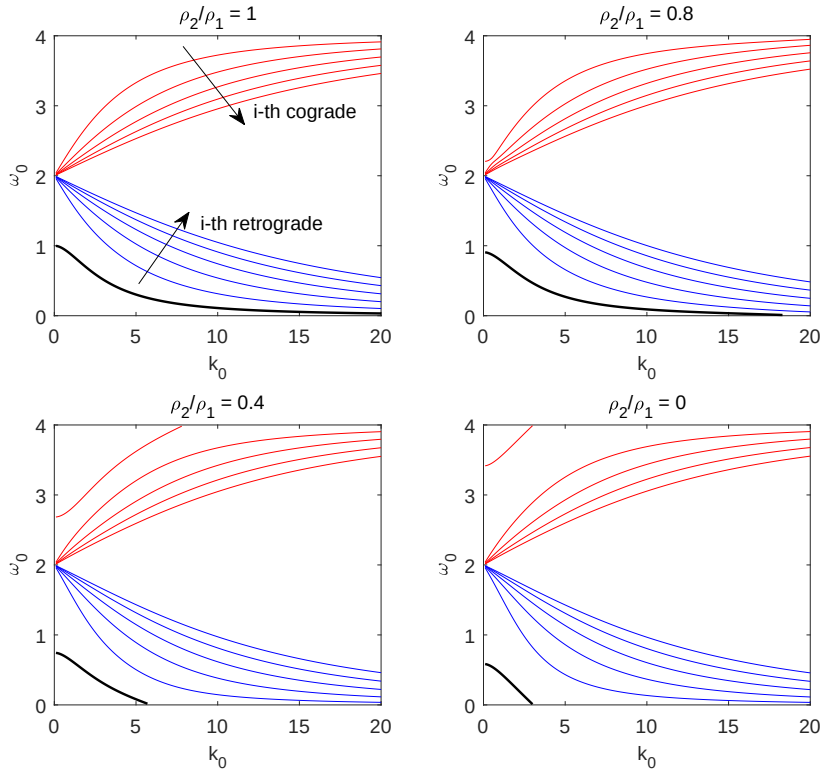

Figure 5.2: Dispersion curves for the Kelvin wave with $m = 2$ for density ratios from one to zero. Red curves are cograde branches and blue curves are retrograde branches. Only the first five branches of each are plotted. An isolated branch (thick black curve) can be seen below the retrograde branches. Surface tension is zero for all plots.

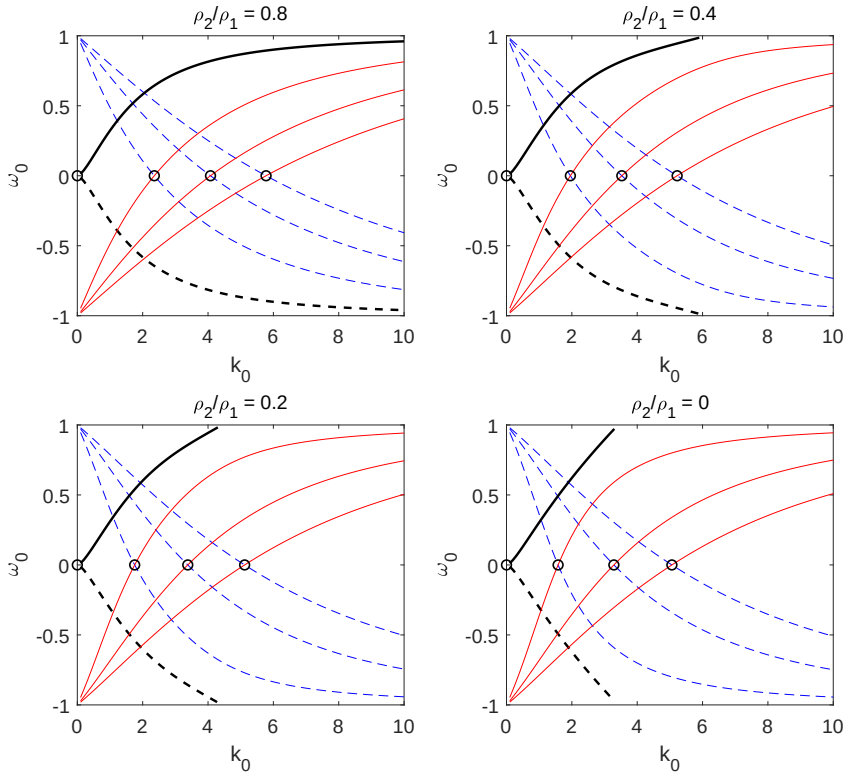

Figure 5.3: The first three cograde modes of the Kelvin wave for $m = -1$ (red) and the first three retrograde modes of the Kelvin wave for $m = 1$ (blue dashed); their isolated branches (thick solid and dashed) can be seen emanating from $(k_0, \omega_0) = (0, 0)$. Circles are the first four principal modes with $\omega_0 = 0$.

As discussed in §,4.3, density and surface tension act to "isolate" the first cograde mode when $(\rho_2/\rho_1, S) \neq (1, 0)$. In figure 5.2, the first cograde mode (the uppermost red curve with the largest value of $|\omega_0 - 2|$) departs from the other cograde modes and shifts upward as the density ratio decreases. The isolated branch (thick black line) also shifts downward from its initial position when $\rho_2/\rho_1 = 1$, and the short wavelength part (large k_0) of the isolated branch drops below $\omega_0 = m - 2$. On the other hand, when the density ratio increases above 1, the situation reverses: the first cograde mode and the isolated mode move closer toward other cograde and retrograde modes. A special scenario is two counter-winding helical waves with wavenumber $m = -1$ and 1 whose dispersion curves are symmetric about the k_0-axis (figure 5.3). In this case, the principal modes are always on the k_0-axis, and $\omega_0 = 0$.

5.3.2 Resonance at $O(\delta\gamma)$

The solution of the $O(\delta\gamma)$ disturbances governed by (5.26)–(5.30) is given in appendix A of Fukumoto (2003). We do not reproduce it here, given its complexity. The solution contains undetermined coefficients α_1, β_1 which must be non-zero. The boundary conditions in (5.32) and (5.33) are used to obtain the dispersion relation. Note that in order to include surface tension, we need to compute f_1 from (5.31) before using the dynamic condition for the dispersion relation. In Moore & Saffman (1975); Tsai & Widnall (1976) and Fukumoto (2003), $\tilde{f}_1$ is not necessary since $\rho_2/\rho_1 = 1$ and surface tension is omitted.

Substituting the basic solution (5.9)–(5.11) into the boundary conditions (5.32) and (5.33) gives

$$\tilde{u}_1 - \frac{\partial\tilde{\phi}_1}{\partial r} = \sin 2\theta \left[\frac{\partial\tilde{\phi}_0}{\partial\theta} - \tilde{v}_0 + \left(1 - \frac{\rho_2}{\rho_1} + 3S\right) \tilde{f}_0 \right]$$

$$+\frac{1}{2}\cos 2\theta\left[-\left(1-\frac{\rho_2}{\rho_1}+3S\right)\frac{\partial\tilde{f}_0}{\partial\theta}+\frac{\partial^2\tilde{\phi}_0}{\partial r^2}-\frac{\partial\tilde{u}_0}{\partial r}\right]; \tag{5.38}$$

$$\begin{aligned}\frac{\rho_2}{\rho_1}\tilde{p}_1-\mathrm{i}\omega_0\tilde{\phi}_1+\frac{\partial\tilde{\phi}_1}{\partial\theta}=&\mathrm{i}\omega_1\tilde{\phi}_0+\sin 2\theta\frac{\partial\tilde{\phi}_0}{\partial r}+\left(1-\frac{\rho_2}{\rho_1}\right)\tilde{f}_1\\&-\frac{1}{2}\left(-1-\frac{\rho_2}{\rho_1}+3S\right)\cos 2\theta\frac{\partial\tilde{\phi}_0}{\partial\theta}+\frac{3}{2}\left(1-\frac{\rho_2}{\rho_1}+2S\right)\cos 2\theta\tilde{f}_0\\&-\frac{1}{2}\cos 2\theta\left[\frac{\rho_2}{\rho_1}\frac{\partial\tilde{p}_0}{\partial r}-\mathrm{i}\omega_0\frac{\partial\tilde{\phi}_0}{\partial r}+\frac{\partial^2\tilde{\phi}_0}{\partial r\partial\theta}\right]\\&-S\left(\frac{\partial^2\tilde{f}_1}{\partial\theta^2}-k_0^2\tilde{f}_1-2k_0k_1\tilde{f}_0-\cos 2\theta\,\frac{\partial^2\tilde{f}_0}{\partial\theta^2}\right).\end{aligned} \tag{5.39}$$

Using the above equations, we write two set of equations for m and $m+2$ in (B.26) to (B.29). They can be written as two inhomogeneous linear systems (B.32) and (B.33) for α_1 and β_1. The dispersion relation (B.39) is given by requiring that α_1 and β_1 are non-trivial (see details in appendix B.3). A dispersion relation for (k_1,ω_1) determines the stability, and the flow is unstable for $\mathrm{Im}\{\omega_1\}>0$. The maximum growth rate σ_{1max} is given by the maximum imaginary part of ω_1 at $k_1=0$; and the half bandwidth of instability, Δk_1, by the range over which the imaginary part of ω_1 vanishes. The expressions for all formulae are too cumbersome to handle manually, and so computer symbolic algebra is utilised to obtain the dispersion relation (B.39) and ω_1 and Δk_1. A description of procedure is given in detailed in appendix B.3, and the symbolic algebra files are provided in the supplementary material. We will show numerical results for $m=-1$ and 1 in the next section followed by the case for $m\geq 0$ in § 5.5.

5.4 Resonance between waves $m=-1$ and 1

We first discuss the special case of the resonance pair $(-1,1)$ in this section. When $m=-1$, the resonance is between the right- and left-handed helical waves. Fukumoto (2003) gives a detailed discussion of this resonance pair. Widnall *et al.* (1974) and Moore

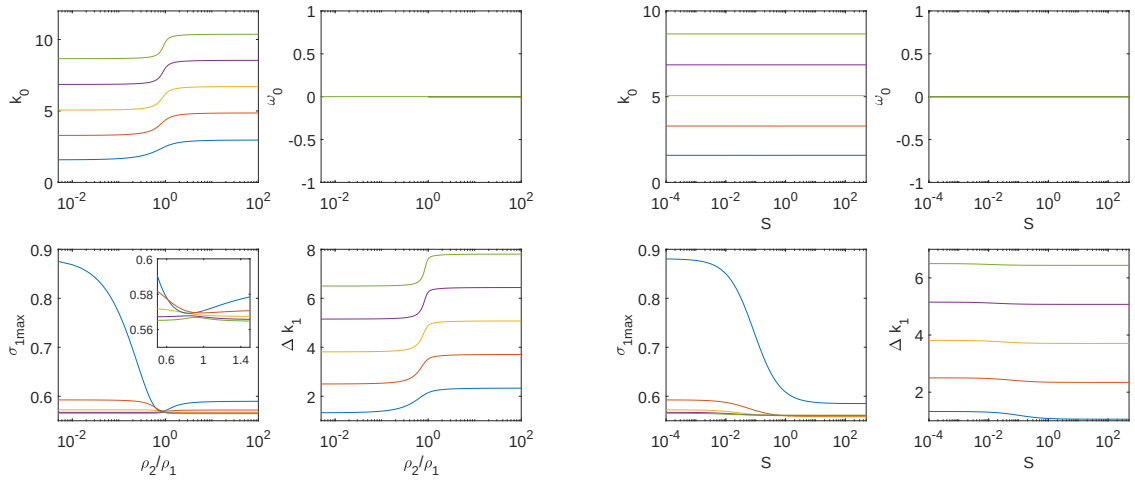

Figure 5.4: Principal modes $(k_0, 0)$ for $(m, m+2) = (-1, 1)$, the maximum growth rate σ_{1max} and the instability half-bandwidth Δk_1 plotted versus (a) density ratio $\rho_2/\rho_1 \in [0.005, 100]$; (b) surface tension $S \in [0, 500]$. The second to sixth principal modes are the blue, red, amber, purple and green curves.

& Saffman (1975) imply that the stationary mode is most unstable. The two dispersion curves are mirrored about $\omega_0 = 0$ (see figure 5.3), and therefore their principal modes are exactly on the k_0-axis.

5.4.1 Principal modes ($\omega_0 = 0$)

We substitute $m = -1$ and $\omega_0 = 0$ for the principal modes of stationary waves (circles in figure 5.3). The maximum growth rate σ_{1max} and half the instability bandwidth Δk_1 are then calculated using computer symbolic algebra. To verify the result of the symbolic calculation, results for $(\rho_2/\rho_1, S) = (1, 0)$ are compared to those in Fukumoto (2003) in table 5.1. The present study has σ_{1max} accurate to ten significant figures and Δk_1 up to five significant figures. As seen in figure 5.3, the first principal mode at $(k_0, \omega_0) = (0, 0)$ is independent of ρ_2/ρ_1 and S, so we will not include it in the comparison here.

The principal modes' maximum growth rates and instability half-bandwidths are plotted as functions of ρ_2/ρ_1 in figure 5.4(a). The second principal mode (blue curve) is the

Table 5.1: For the $m = -1$ and 1 resonances, present results for $\rho_2/\rho_1 = 1$ compared to table 1 of Fukumoto (2003). Each row represents a principal mode with $k_0 = 0$.

	k_0	σ_{1max}	Δk_1
Fukumoto (2003)	2.504982369	0.5707533917	2.145502816
	4.349076726	0.5694562098	3.518286549
	6.174012330	0.5681222780	4.883945142
	7.993536550	0.5671646287	6.247280752
	9.810807288	0.5664714116	7.609553122
Present work	2.50498236892631	0.570753391682824	2.14548262220342
	4.34907672483174	0.569456209750883	3.51827586739091
	6.17401232939918	0.568122278011138	4.88395077269524
	7.99353654972030	0.567164628732371	6.24727962008910
	9.81080728697861	0.566471411560612	7.60954536410281

most unstable mode. The largest growth rate is at $\rho_2/\rho_1 = 0$ with a value of $\sigma_{1max} = 0.882$. The least unstable density ratio is 0.915 where the second and third principal modes have a growth rate of 0.5696. The instability half bandwidth Δk_1 is strongly correlated with the wavenumber k_0, and the principal mode with higher k_0 has wider instability bandwidth. Figure 5.4(b) shows the effect of surface tension when $\rho_2/\rho_1 = 0.001$. The density ratio 0.001 is picked because it is close to the typical ratio between air and water. Surface tension merely changes the locations of principal modes. The second principal mode dominates the instability. The growth rate is 0.8803 at $S = 10^{-4}$ and drops to 0.585 when $S = 500$.

The growth rate and the instability half-bandwidth are calculated for large k_0 in figure 5.5 with different values of $\rho_2/\rho_1 \in [0, 1]$ and $S \in [0, 100]$. For the growth rate σ_{1max}, density only has an effect for those principal modes with $k_0 < 10$. The growth rates for different values of ρ_2/ρ_1 and S all converge to a fixed value 0.5625 as $k_0 \to \infty$. The short-wavelength limit given in (5.13) of Fukumoto (2003) for $(\rho_2/\rho_1, S) = (1, 0)$ as

$$\sigma_{1max} \approx \frac{9}{16}\left(1 + \frac{1}{12k_0} - \frac{7}{48k_0^2} + \frac{5}{64k_0^3}\right), \tag{5.40}$$

is plotted as the dashed line in figure 5.5.

5.4.2 Non-principal modes

For stationary waves $m = \pm 1$, non-principal modes are intersection points where $\omega_0 \neq 0$. In the case $\rho_2/\rho_1 = 1$ and $S = 0$, the growth rates of non-principal modes are at least two order smaller than that of the principal modes (see figure 5.6a). As the density ratio decreases to zero, the maximum growth rates of non-principal modes grow and become one order of magnitude smaller than those of the principal modes. The trend reverses for increasing surface tension. The maximum growth rate of non-principal modes is one order of magnitude less than that of the principal modes and that difference widens

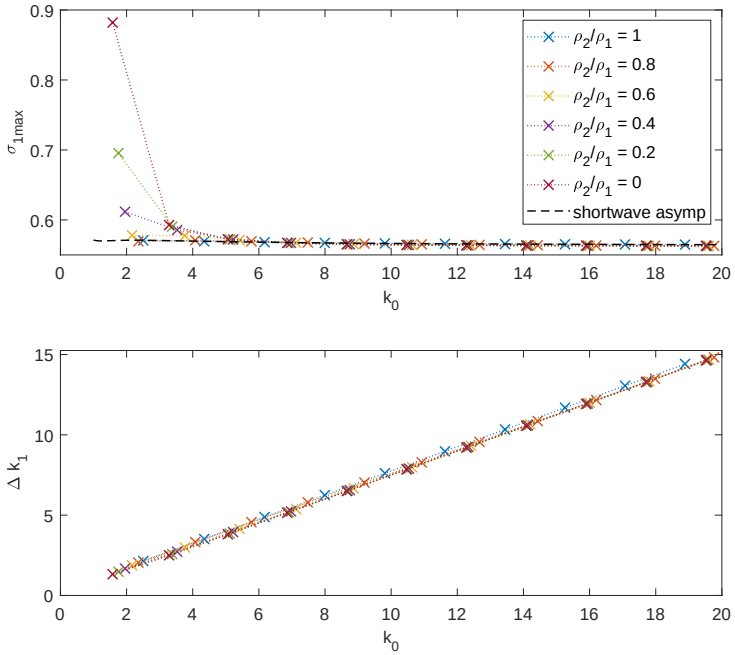

(a)

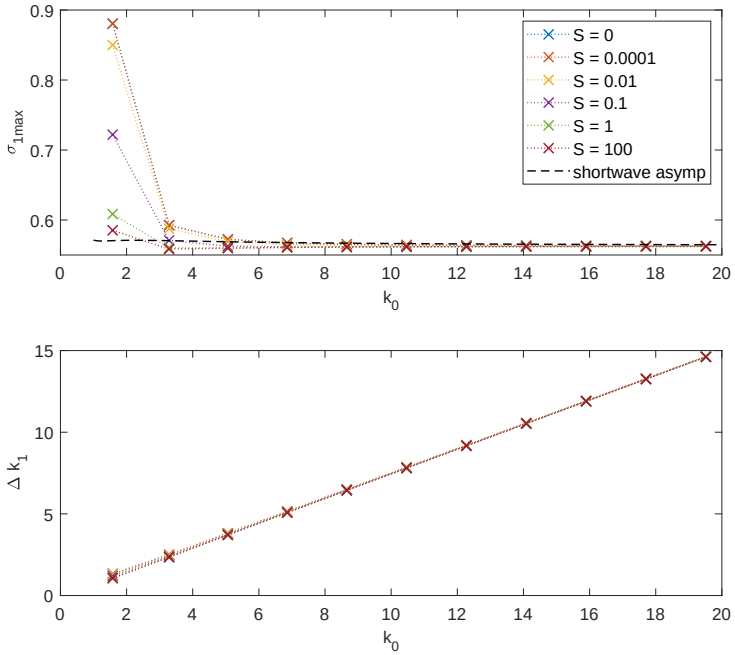

(b)

Figure 5.5: Maximum growth rate σ_{1max} and unstable half-bandwidth Δk_1 of principal modes $k_0 < 20$ for helical waves $(m, m+2) = (-1, 1)$; (a) different ρ_2/ρ_1 with $S = 0$; (b) different S with $\rho_2/\rho_1 = 0.001$. The dashed line is the short-wavelength asymptotic result for $\rho_2/\rho_1 = 1$.

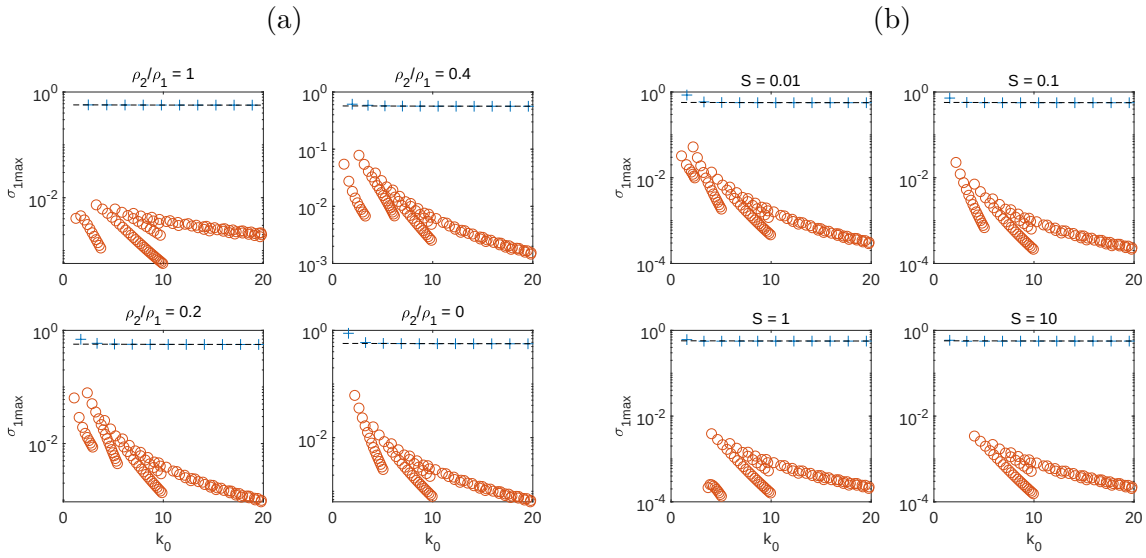

Figure 5.6: Maximum growth rate σ_{1max} for the modes of the $(-1, 1)$ resonance with variations of (a) ρ_2/ρ_1; and (b) S. Principal modes are marked by blue crosses while other modes are red circles. The black dashed line is the short-wavelength asymptotic result (5.40) for $\rho_2/\rho_1 = 1$ and $S = 0$.

to more than two orders of magnitude for $S = 10$ in figure 5.6(b). With variations in either density or surface tension, the instability of the principal modes always dominates over non-principal modes.

5.5 Resonance between waves m and $m + 2$ $(m \geq 0)$

We continue to explore resonant pairs of $(m, m + 2)$ other than $(-1, 1)$. Among those pairs, the case of $(0, 2)$ is particular interesting. As Fukumoto (2003) states, this is due to its resistance to viscous dissipation when the Reynolds number is not sufficiently large (Eloy & Le Dizès, 2001). We first discuss the $(0, 2)$ resonant pair, followed by other helical waves.

5.5.1 The case $m = 0$

We calculate the growth rate σ_{1max} and half the unstable bandwidth Δk_1 for the first five principal modes. The definition of principal modes is the same as in Eloy & Le Dizès (2001) and Fukumoto (2003): the first principal mode is the intersection between the first cograde mode for $m = 0$ and the isolated mode for $m = 2$; the second principal mode is the second cograde mode for $m = 0$ intersected by the first retrograde mode for $m = 2$; and so on. The location (k_0, ω_0) of the principal modes in figure 5.7(a) shows that k_0 shifts to lower wavelengths as the density ratio ρ_2/ρ_1 drops below one. The first principal mode's growth rate has a cusp at $\rho_2/\rho_1 = 0.215$ with $\sigma_{1max} \approx 4.32$. The mode is then stabilised below $\rho_2/\rho_1 < 0.215$ and disappears near $\rho_2/\rho_1 \approx 0.09$. The third principal mode is the most unstable with $\sigma_{1max} = 0.5668647793$ for $\rho_2/\rho_1 = 1$ in the calculation of Fukumoto (2003). In our calculation with density variations, the second principal mode is the most unstable mode as $\rho_2/\rho_1 \to 0$ with $\sigma_{1max} = 0.6028$. while the first principal mode is the most unstable for $\rho_2/\rho_1 \to 100$ with $\sigma_{1max} = 0.6167$. The trend of Δk_1 is very similar to that of k_0: as the density ratio decreases the unstable bandwidth decreases. We also extend our calculation to other principal modes with higher wavenumber k_0 in figure 5.8. The growth rate is asymptotically close to that of (5.40) in the short-wavelength regime for $\rho_2/\rho_1 = 1$. For large k_0 Δk_1 increases linearly with k_0 and the slopes are identical except for $k_0 < 4$.

The dependence on surface tension S is shown in figure 5.7(b) for $\rho_2/\rho_1 = 0.2$. The first principal mode disappears as surface tension increases to $S \approx 0.14$ and is always unstable until it disappears. The effect on the other four principal modes is not significant. The second principal mode (red curve) has the biggest drop in σ_{1max} from a value of 0.6049 to 0.5482 at $S = 100$.

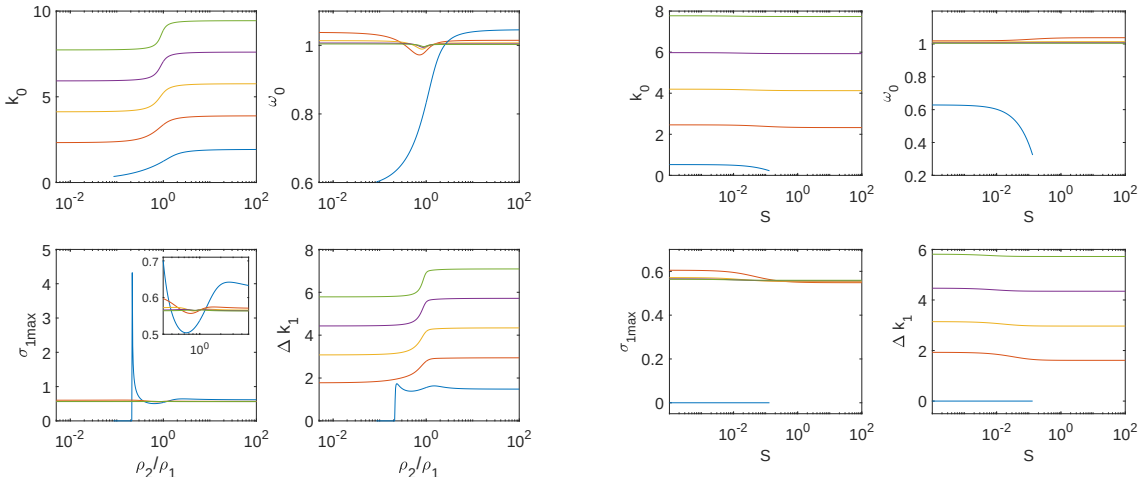

Figure 5.7: Principal modes for $(m, m+2) = (0, 2)$, maximum growth rate σ_{1max} and the instability half-bandwidth Δk_1 plotted versus (a) density ratio $\rho_2/\rho_1 \in [0.005, 100]$; (b) surface tension $S \in [0, 500]$ at $\rho_2/\rho_1 = 0.2$. The first to fifth principal modes are the blue, red, amber, purple and green curves.

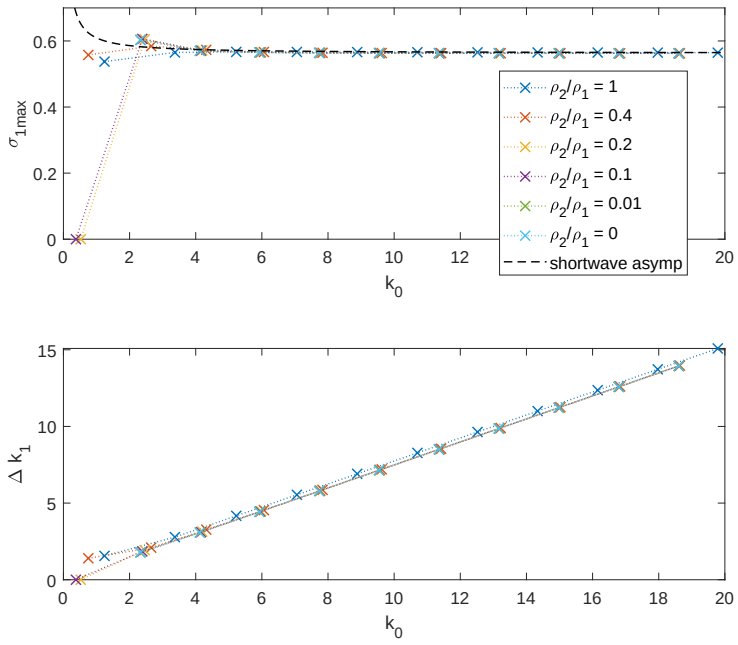

Figure 5.8: Maximum growth rate σ_{1max} and unstable half-bandwidth Δk_1 of principal modes $k_0 < 20$ for $(m, m+2) = (0, 2)$ with different ρ_2/ρ_1 with $S = 0$. The dashed line is the short-wavelength asymptotic result (5.40) for $\rho_2/\rho_1 = 1$.

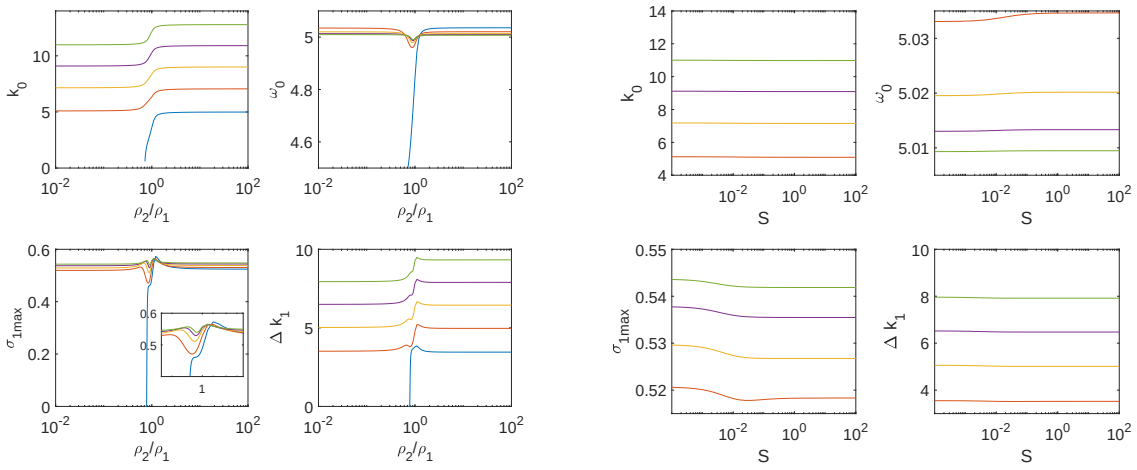

Figure 5.9: Principal modes for $(m, m+2) = (4, 6)$, the maximum growth rate σ_{1max} and the instability half-bandwidth Δk_1 are plotted versus (a) density ratio $\rho_2/\rho_1 \in [0.01, 100]$; (b) surface tension $S \in [0, 100]$ at $\rho_2/\rho_1 = 0.2$. The first to fifth principal modes are the blue, red, amber, purple and green curves.

5.5.2 Other pairs of $(m, m+2)$

Moving on to higher resonance pairs, e.g. $(m, m+2) = (4, 6)$, we found the change in the positions (k_0, ω_0) of principal modes (see figure 5.9a) to be qualitatively similar to that for the $(0, 2)$ pair. The first principal mode (in blue in figure 5.9) disappears near a larger density ratio at the value of $\rho_2/\rho_1 = 0.72$. The most significant difference is how the growth rate behaves before the first principal mode disappears. The growth rate of the first principal mode increases drastically and then drops to zero before the first principal mode vanishes in the $(0, 2)$ resonance (figure 5.7a), while σ_{1max} plunges to zero for $(4, 6)$ in figure 5.9(a) and never exceeds 0.6. The dependence on surface tension S is shown in figure 5.9(b). The growth rate σ_{1max} decreases only slightly, and is almost independent of surface tension for $S \gtrsim 1$.

Resonance pairs with higher azimuthal wavenumber m have smaller growth rate σ_{1max} for the MSTW instability, while the curvature instability is more unstable for larger

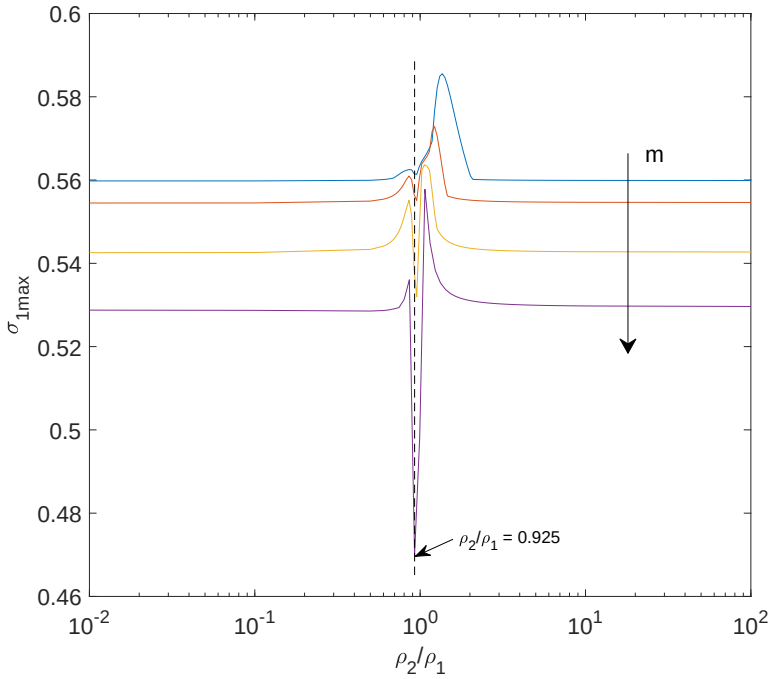

Figure 5.10: Maximum growth rate for modes for $\rho_2/\rho_1 \in [0.01, 100]$. Blue, red, amber and purple curves are for resonance pairs $(m, m+2)$, $m = 2$, 4, 8 and 16 respectively. The vertical dashed line is the value $\rho_2/\rho_1 = 0.925$ where the growth rate has a dip.

m (see Chang & Llewellyn Smith, 2020). In figure 5.10 we plot the maximum growth rate among intersection points (resonant modes) that include the principal modes and few non-principal modes for axial wavenumber $k_0 \leq 20$, as a function of density ratio ρ_2/ρ_1. The maximum growth rate decreases as m increases. This is due to the strain field, which kills the small-scale disturbances on the boundary. For a fixed value of m the growth rate is constant to the two ends of the plot, i.e. as $\rho_2/\rho_1 \to \pm\infty$, and the curve has a dip in the middle at $\rho_2/\rho_1 = 0.925$. That is where the most unstable mode (the one with the largest growth rate) jumps from one intersection point of Kelvin waves to another. As shown in figure 5.11, the most unstable mode represented by a black dot switches from the seventh principal mode to the fourth principal mode as density ratio increases from 0.925 to 1.069. The sharp discontinuities in the curves in figure 5.10 may seem strange at first glance, but are actually appropriate.

Given that the whole calculation is based on those discrete intersection points of Kelvin waves, the largest growth rate among all modes can have a discontinuity while it switches from one intersection point to another. That happens when the previous most unstable mode decayed or disappeared and another mode took over. The instability of a resonance mode is a function of its location (k_0, ω_0) and the location is a function of density ratio and surface tension. The migrations of the first cograde mode and the isolated mode discussed in § 3 also have a huge influence on the location of intersection points.

5.6 Conclusion

The parametric instability of a vortex column subjected to a weak strain field has been investigated for various density ratio and surface tension. The instability, the Moore–Saffman–Tsai–Widnall instability, is the result of the resonance between two Kelvin waves of azimuthal wavenumber m and $m + 2$. The resonance is fed by a quadrupole field which

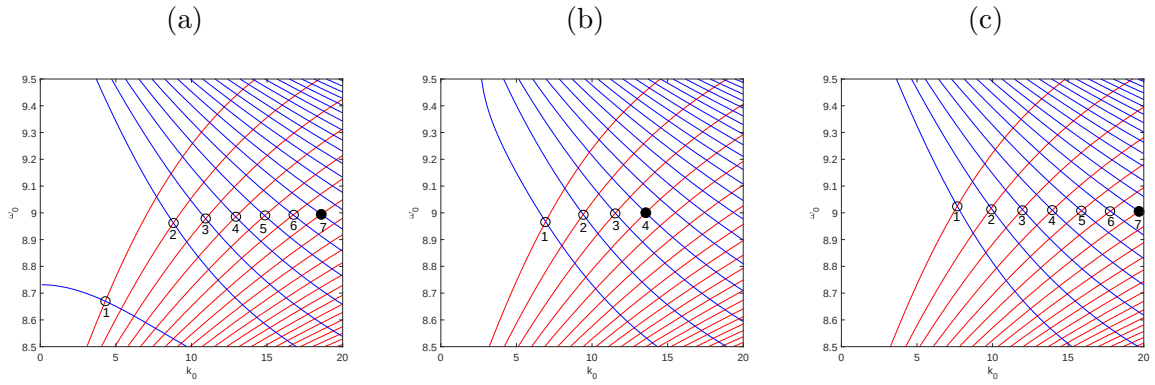

Figure 5.11: Intersection points of the pair $(m, m+1) = (8, 10)$; (a) $\rho_2/\rho_1 = 0.925$; (b) $\rho_2/\rho_1 = 1.069$ and (c) $\rho_2/\rho_1 = 10$. Principal modes are labeled by numbered circles; the black dot is the mode with largest growth rate. The most unstable mode switches from the seventh principal mode to the fourth principal mode, then back to the seventh, causing the discontinuity in σ_{1max}.

comes from the correction to the basic state at $O(\gamma)$. We have extended the calculation by Fukumoto (2003) to a parameter space $(\rho_2/\rho_1, S)$, where $(\rho_2/\rho_1, S) = (1, 0)$ is the previous result.

Two distinguished types of resonances are examined. The first corresponds to stationary helical waves with wavenumber $m = \pm 1$. The strained vortex is most unstable when the density ratio is very small $(\rho_2/\rho_1 \to 0)$: the maximum growth rate is $\sigma_{1max} \approx 0.88$ compared to a minimum of 0.57 near $\rho_2/\rho_1 = 1$. Surface tension mitigates the instability of the vortex for $S > 0.01$, and the maximum growth rate drops from 0.88 to 0.58 as $S \to \infty$. We have also shown that the most unstable modes are dominated by the principal modes in the resonances for $m = \pm 1$ stationary waves. The second type of resonances is for wavenumber $m \geq 0$, and $m = 0$ is a particular case of bulging modes. For the $(0, 2)$ resonance, the maximum growth rate from the first principal mode maximizes near $\rho_2/\rho_1 = 0.215$ with a very large value, and that mode vanishes as $\rho_2/\rho_1 \to 0$ while the second principal mode takes over to become most unstable. We have also shown that the maximum growth rate decreases as the azimuthal wavenumber m increases, which is in contrast to the curvature instability.

In the recent study by Hattori *et al.* (2019) using direct numerical simulations, the short-wavelength MSTW instability (the elliptic instability) is shown to be more unstable than the curvature instability for a vortex ring of Gaussian core structure. This result demonstrates the correctness of the theoretical prediction in Blanco-Rodriguez & Le Dizès (2016) on the elliptic instability for the Batchelor vortex (a vortex with a Gaussian core). Furthermore, the analytical result of curvature instability for a Gaussian core (Blanco-Rodriguez & Le Dizès, 2017) has also been confirmed in Hattori *et al.* (2019). This is the first numerical evidence for the curvature instability after its discovery in Hattori & Fukumoto (2003) and Fukumoto & Hattori (2005) for vortex rings. The present study considers uniform cores with a jump in density across the boundary. It would be of interest to extend this result to continuous vorticity and density distributions. It will be more complicated to carry out a full numerical simulation for this kind of problem with large density jumps at the boundary of the vortices. . Direct numerical simulations to detect the curvature and MSTW instabilities of vortices with density differences hence remain unfinished tasks for the future.

Chapter 5, in full, has been submitted for publication of the material as it may appear in the Journal of Fluid Mechanics, "Density and surface tension effects on vortex ring stability. II Moore–Saffman–Tsai–Widnall instability" by C. Chang and S. G. Llewellyn Smith, 2020 (Cambridge University Press). The dissertation author was the primary investigator and author of this material.

Chapter 6

Conclusions

Fluid flows are complex systems that manifest interesting physics. Vortex dynamics provides an effective way to understand the underlying physics of incompressible Euler flows, and is a relevant tool for many applications such as aerodynamics and fluid-solid interactions. While the classic models mostly deal with forces such as inertia and pressure, there are additional physical effects that can be added into the formulations for various flow problems. The most common example is using vortex sheet to model free-surface flow and Rayleigh–Taylor instability, where there is a density jump across the sheet. The present work has calculated the motion and stability of vortices using an extended vortex dynamics formulation. The density of vortex is different form the density of the fluid that surrounds it, and gravity and surface tension are also added into the calculations.

In Chapter 2, we derived a new mathematical model for buoyant vortex filaments using force balance. Our model shows that buoyancy acts to decrease the local curvature of the filament, which confirms the analytic result from previous works that a buoyant vortex thin ring will expand as it elevates. An equation for the axial flow inside filament core is obtained showing that the interior lighter fluid flows against gravity.

In Chapter 3, we formulated a set of coupled integro-differential equations in contour

dynamics that calculates the motion of a buoyant vortex ring. Vorticity is generated by baroclinic torque that turns the interface into a vortex sheet enclosed a vortex patch. The evolution equation for the vortex sheet strength is derived and numerical solutions are attempted. The time of numerical calculation is limited by the blowu, but the result shows a complex dynamic of vortex sheet that includes the curvature singularity of sheet evolution, a nonlinearity from the quadratic term, and a dynamical coupling with the Lagrangian velocity that leads to a Fredholm integral equation.

We have also calculated the stability of vortices with the effects of density and surface tension in this dissertation work. The basic state solution is given as a perturbation series and normal modes analysis are used to study two type of parametric instabilities: curvature instability and Moore–Saffman–Tsai–Widnall instability, with the aid of symbolic computer algebra. In Chapter 4, our calculation for curvature instability showed that a density variation makes a vortex ring more unstable while the vortex core is lighter or heavier than its ambient. The vortex is more unstable for small k_0 and large m when subjected to curvature instability. Chapter 5 dealt with the MSTW instability, the strained vortex is most unstable for small k_0, but instability decays as m increases. Surface tension stabilized both instabilities very marginally.

6.1 Applications

In the present dissertation, we have extended two classic models for vortex motions: vortex filaments and contour dynamics for vortex patches. The effects of density variation, buoyancy, and surface tension have been added to the mathematical formulations to include the appropriate physics. These new models have the potential to be utilized in a number of engineering applications:

Aero/hydrodynamics surfaces with high angle of attack

Aircrafts or maritime vessels rely on control surfaces to adjust their attitude and motion for them to maneuver in air/water. When these control surfaces are in action, they usually create a high angle of attack with the oncoming stream and a force perpendicular to the surface, i.e. lift, is generated. The flow separates from the leading edge of the surface and a leading-edge vortex will emerge. If a CFD scheme, e.g. LES or RANS, is used to simulate the flow field, the computational grids and operations require large computer efforts. Vortex sheets or series of point vortices can be used to approximate the flow field, and the computational cost can be significantly reduced. If one needs a quick and reliable calculation of lift, vortex models provide a very good estimate compared with CFD (see Eldredge & Jones, 2019). The low CPU time can provide a possible real-time estimate in, e.g. closed-loop control, applications. An extension to three-dimensional models using vortex filaments and sheets is also an intriguing research topic. In hydrodynamics applications, the separation of leading-edge vortex can create cavitation bubbles filled with gas taken out of solution. The analysis for cavitation bubbles should then use the model we developed in Chapter 3.

Helical wake vortices from rotary machinery

Rotary machinery like wind turbines or vessel propellers generate vorticial flow structures from its tips due to the pressure difference on both sides. These wing-tip vortices spiral downstream to form a wake. The efficiency of the machinery and the load on the structure are impacted by the helical wake. Helical vortex filaments are frequently used to model this kind of flow field. The new model in Chapter 2 adds buoyancy and surface tension to vortex filaments and make it an appropriate tool for the cavitation problem of ship propulsion or energy harvest like marine hydro generator. The problem could use a numerical scheme for wake (Winckelmans *et al.*, 2005) with a modification for

buoyancy and a possible combination with CFD to obtain a Lagrangian-Eulerian hybrid scheme.

6.2 Future work

Other than density, buoyancy, and surface tension, there are several other physical effects that can also be included in vortex dynamics. For example, magnetic force or magnetic field is added to study magnetohydrodynamics. A model for vortex-current filaments is given in Yatsuyanagi *et al.* (1996), which is based on the momentum balance (Moore & Saffman, 1972) for a filament. A combination of the present buoyant model with this vortex-current filaments is interesting and has implications in astrophysical fluid dynamics. Beside filament models, contour dynamics has also been coupled with a toroidal magnetic field in Hattori & Moffatt (2006), Llewellyn Smith & Hattori (2012). Like buoyancy does to the contour dynamics, magnetic field results a vortex sheet on contour, and the two effects can be coupled together (see Llewellyn Smith *et al.*, 2018). Adding compressibility is also a possible extension, and theoretical or numerical calculations for these vortices still remain open tasks.

In our stability calculations, Rankine vortex gives the vorticity profile as a Heaviside step function. It would be interesting to do calculations for a continuous profile, e.g. a Gaussian function, which is a more realistic situation. The importance of gravity is assumed negligible and we freeze the vortex ring in a steady state in the present study. To study the stability of buoyant vortices without this constraint, we may need to perform numerical simulations combining with modal analysis tools. The present linear analysis is a stepping stone to studies of nonlinear evolution using direct numerical simulations.

There are also several vortex problems that deal with single density flows could be investigated in the future. Kida (1981) gives steady solutions for vortex filaments under

the local induction approximation, but the stability of these steady solutions are not fully understood yet. A furthermore question would be if there is any steady solution that satisfies the Biot-Savart law (Oberti & Ricca, 2019). Vortex sheets have been used for the study of shear layer and interfacial dynamics. A possible new model in dipole sheet or vortex-dipole sheet, which are an asymptotic limit of two vortex sheets of opposite sign collapsed together, is also an intriguing question.

Appendix A

Supplementary formulae for axisymmetric contour dynamics

A.1 Calculation of $\boldsymbol{t}\cdot\mathrm{d}\mathbf{u}/\mathrm{d}t$

Taking the material derivative $\mathrm{d}/\mathrm{d}t$ of (3.11) yields

$$\begin{aligned}\frac{\mathrm{d}u_{p,r}}{\mathrm{d}t} =& -\frac{\Omega}{R^2}u_r\oint R'\cos\theta' G\mathrm{d}s' \\ &+\frac{\Omega}{R}\oint\left(u_r'\cos\theta' G - R'\sin\theta'\frac{\mathrm{d}\theta'}{\mathrm{d}t}G + R'\cos\theta'\frac{\mathrm{d}G}{\mathrm{d}t}\right)\mathrm{d}s',\end{aligned} \tag{A.1}$$

$$\begin{aligned}\frac{\mathrm{d}u_{p,z}}{\mathrm{d}t} =&\Omega\oint\left[(u_z'-u_z)\cos\theta' H - (Z'-Z)\sin\theta'\frac{\mathrm{d}\theta'}{\mathrm{d}t}H + (Z'-Z)\cos\theta'\frac{\mathrm{d}H}{\mathrm{d}t}\right]\mathrm{d}s' \\ &-\Omega\oint\left(\cos\theta'\frac{\mathrm{d}\theta'}{\mathrm{d}t}G + \sin\theta'\frac{\mathrm{d}G}{\mathrm{d}t}\right)\mathrm{d}s'.\end{aligned} \tag{A.2}$$

The primes indicate dummy variables in the integrals and (R, Z) is the location of Lagrangian point. The first subscript represent the contribution from the vortex patch or vortex sheet, while the second subscript indicates the velocity components. We do the

same for (3.13) for the sheet:

$$\frac{\mathrm{d}u_{s,r}}{\mathrm{d}t} = -\frac{1}{R}\oint \frac{\mathrm{d}\gamma}{\mathrm{d}t}\frac{\partial G}{\partial Z}\mathrm{d}\xi' + \frac{1}{R^2}u_r \oint \gamma\frac{\partial G}{\partial Z}\mathrm{d}\xi' - \frac{1}{R}\oint \gamma\frac{\mathrm{d}}{\mathrm{d}t}\left(\frac{\partial G}{\partial Z}\right)\mathrm{d}\xi', \tag{A.3}$$

$$\frac{\mathrm{d}u_{s,z}}{\mathrm{d}t} = \frac{1}{R}\oint \frac{\mathrm{d}\gamma}{\mathrm{d}t}\frac{\partial G}{\partial R}\mathrm{d}\xi' - \frac{1}{R^2}u_r \oint \gamma\frac{\partial G}{\partial R}\mathrm{d}\xi' + \frac{1}{R}\oint \gamma\frac{\mathrm{d}}{\mathrm{d}t}\left(\frac{\partial G}{\partial R}\right)\mathrm{d}\xi'. \tag{A.4}$$

Taking the dot product of $\mathrm{d}\mathbf{u}/\mathrm{d}t$ with the tangent $\boldsymbol{t} = L^{-1}(\partial R/\partial\xi, \partial Z/\partial\xi)$ yields (3.29) with

$$\begin{aligned} f(R,Z,\gamma,\mathbf{u}) =& \frac{1}{L}\frac{\partial R}{\partial \xi}\left[\frac{\Omega}{R}\oint\left(u_r'\cos\theta' G - R'\sin\theta'\frac{\mathrm{d}\theta'}{\mathrm{d}t}G + R'\cos\theta'\frac{\mathrm{d}G}{\mathrm{d}t}\right)\mathrm{d}s'\right. \\ & \left. -\frac{\Omega}{R^2}u_r\oint R'\cos\theta' G\mathrm{d}s' - \frac{1}{R^2}u_r\oint\gamma\frac{\partial G}{\partial Z}\mathrm{d}\xi' - \frac{1}{R}\oint\gamma\frac{\mathrm{d}}{\mathrm{d}t}\left(\frac{\partial G}{\partial Z}\right)\mathrm{d}\xi'\right] \\ & + \frac{1}{L}\frac{\partial Z}{\partial\xi}\left\{-\Omega\oint\left(\cos\theta'\frac{\mathrm{d}\theta'}{\mathrm{d}t}G + \sin\theta'\frac{\mathrm{d}G}{\mathrm{d}t}\right)\mathrm{d}s'\right. \\ & + \Omega\oint\left[(u_z'-u_z)\cos\theta' H - (Z'-Z)\sin\theta'\frac{\mathrm{d}\theta'}{\mathrm{d}t}H + (Z'-Z)\cos\theta'\right. \\ & \left.\left.\times\frac{\mathrm{d}H}{\mathrm{d}t}\right]\mathrm{d}s' + \frac{1}{R^2}u_r\oint\gamma\frac{\partial G}{\partial R}\mathrm{d}\xi' + \frac{1}{R}\oint\gamma\frac{\mathrm{d}}{\mathrm{d}t}\left(\frac{\partial G}{\partial R}\right)\mathrm{d}\xi'\right\}. \end{aligned} \tag{A.5}$$

A.2 Expressions for the kinetic and potential energies

Using (3.11.4) in Saffman (1992), the kinetic energy in a volume V is given by

$$T = \frac{1}{2}\rho\int_V |\mathbf{u}|^2\,\mathrm{d}V = \frac{1}{2}\rho\left[\int_V \mathbf{A}\cdot\boldsymbol{\omega}\,\mathrm{d}V - \int_S(\mathbf{u}\times\mathbf{A})\cdot\boldsymbol{n}\,\mathrm{d}S\right], \tag{A.6}$$

where the unit normal vector $\boldsymbol{n}$ points out from the volume V enclosed by the surface S, and the vector potential gives $\mathbf{u} = \nabla\times\mathbf{A}$. For axisymmetric flows in (r,ϕ,z),

$$\boldsymbol{\omega} = \omega_\phi\hat{\boldsymbol{\phi}},\ \mathbf{A} = \frac{\psi}{r}\hat{\boldsymbol{\phi}}$$

and

$$\mathrm{d}V = r\mathrm{d}r\,\mathrm{d}\phi\,\mathrm{d}z, \quad \mathrm{d}S = r\,\mathrm{d}\phi\,\mathrm{d}s,$$

where the surface S is a torus and s is the arc length of a contour on the rz plane. Integrating over ϕ gives

$$T = \pi\rho\left[\iint \omega_\phi\psi\,\mathrm{d}r\,\mathrm{d}z - \oint(\mathbf{u}\times\mathbf{A})\cdot\boldsymbol{n}r\,\mathrm{d}s\right]. \tag{A.7}$$

For the setting shown in figure 3.1, the kinetic energies outside and inside the vortex are

$$T_1 = -\pi\rho_1\oint(\mathbf{u}_1\times\mathbf{A})\cdot(-\boldsymbol{n})r\,\mathrm{d}s, \tag{A.8}$$

and

$$T_2 = \pi\rho_2\left[\iint \omega_\phi\psi\,\mathrm{d}r\,\mathrm{d}z - \oint(\mathbf{u}_2\times\mathbf{A})\cdot\boldsymbol{n}\;r\mathrm{d}s\right], \tag{A.9}$$

respectively. The total kinetic energy is $T = T_1 + T_2$. The double integral in T_2 corresponds to the vortex patch,

$$T_p = \pi\rho_2\iint\omega_\phi\psi\,\mathrm{d}r\,\mathrm{d}z = \pi\rho_2\Omega\iint\psi r\mathrm{d}r\,\mathrm{d}z, \tag{A.10}$$

and can be calculated using (A3) in Pozrikidis (1986) as a contour integral. The remaining integrals in T are related to the vortex sheet:

$$T_s = \pi\rho_1\oint(\mathbf{u}_1\times\mathbf{A})\cdot\boldsymbol{n}\;r\,\mathrm{d}s - \pi\rho_2\oint(\mathbf{u}_2\times\mathbf{A})\cdot\boldsymbol{n}r\,\mathrm{d}s. \tag{A.11}$$

By using $\mathbf{u}_i = u_i\hat{\mathbf{r}} + v_i\hat{\mathbf{z}}$ and $\mathrm{d}s = L\,\mathrm{d}\xi$, we obtain

$$(\mathbf{u}_i\times\mathbf{A})\cdot\boldsymbol{n} = \frac{\psi}{r}\left(u_i\frac{\partial R}{\partial\xi} + v_i\frac{\partial Z}{\partial\xi}\right)\frac{1}{L} = \frac{\psi}{r}\mathbf{u}_i\cdot\boldsymbol{t}. \tag{A.12}$$

Then (A.11) becomes

$$T_s = \pi\rho_1 \oint \psi \mathbf{u}_1 \cdot \boldsymbol{t} \mathrm{d}s - \pi\rho_2 \oint \psi \mathbf{u}_2 \cdot \boldsymbol{t} \mathrm{d}s, \tag{A.13}$$

$$= (\rho_1 - \rho_2)\,\pi \oint \psi \mathbf{u} \cdot \boldsymbol{t}\ L\mathrm{d}\xi + (\rho_1 + \rho_2)\,\frac{\pi}{2} \oint \psi\gamma \mathrm{d}\xi. \tag{A.14}$$

If $\rho_1 = \rho_2 = \rho$,

$$T_s = \pi\rho \oint \psi(\mathbf{u}_1 - \mathbf{u}_2) \cdot \boldsymbol{t} L\mathrm{d}\xi, = \pi\rho \oint \psi\gamma\, \mathrm{d}\xi, \tag{A.15}$$

where $\gamma = L(\mathbf{u}_1 - \mathbf{u}_2) \cdot \boldsymbol{t}$. Taking $\rho = 1$, this is identical to (2.36) in Hattori & Moffatt (2006). Finally, the potential energy is calculated from

$$U = 2\pi(\rho_2 - \rho_1)g \iint rz\mathrm{d}r\mathrm{d}z = \pi(\rho_2 - \rho_1)g \oint RZ^2 \frac{\partial R}{\partial \xi}\mathrm{d}\xi. \tag{A.16}$$

Appendix B

Linear stability calculation

B.1 The basic state solution

The basic solution is obtained as a perturbation series as shown in (4.12) or (5.8). The leading-order solution is the Rankine vortex and the boundary is circular. Pressure is obtained from

$$-\frac{V_0^2}{r} = -\frac{\partial P_0}{\partial r} \tag{B.1}$$

inside and from the Bernoulli equation outside. The dynamic boundary condition for pressure on $r = 1$ gives

$$\frac{\rho_2}{\rho_1} P_0 + \frac{1}{2}\left(\frac{\partial \Phi_0}{\partial \theta}\right)^2 = S. \tag{B.2}$$

B.1.1 With a small curvature ϵ

The solution in (4.12) at $O(\epsilon)$, the governing equations lead to

$$\frac{\partial U_1}{\partial \theta} - 2V_1 = -\frac{\partial P_1}{\partial r}, \tag{B.3}$$

$$2U_1 + \frac{\partial V_1}{\partial \theta} = -\frac{1}{r}\frac{\partial P_1}{\partial \theta}, \tag{B.4}$$

$$\frac{\partial U_1}{\partial r} + \frac{U_1}{r} + \frac{1}{r}\frac{\partial V_1}{\partial \theta} = -r\cos\theta \tag{B.5}$$

in the core and

$$\frac{\partial^2 \Phi_1}{\partial r^2} + \frac{1}{r}\frac{\partial \Phi_1}{\partial r} + \frac{1}{r^2}\frac{\partial^2 \Phi_1}{\partial \theta^2} = -\frac{\cos\theta}{r} \tag{B.6}$$

outside the core. The matching conditions (4.10)–(4.11) give

$$U_1 = \frac{\partial F_1}{\partial \theta} = \frac{\partial \Phi_1}{\partial r}, \tag{B.7}$$

$$\frac{\rho_2}{\rho_1}P_1 + \frac{\partial \Phi_1}{\partial \theta} + F_1\left(\frac{\rho_2}{\rho_1} - 1\right) = -S\left(-\sin\theta + F_1 + \frac{\partial^2 F_1}{\partial \theta^2}\right) \tag{B.8}$$

at $r = 1$. Solving the above system with the condition $F_1 = 0$ leads to the solution in (4.15) and (4.16).

B.1.2 With a weak strain field γ

The solution in (5.8) at $O(\gamma)$, the linearized governing equations give

$$\frac{\partial U_1}{\partial \theta} - 2V_1 = -\frac{\partial P_1}{\partial r}, \tag{B.9}$$

$$2U_1 + \frac{\partial V_1}{\partial \theta} = -\frac{1}{r}\frac{\partial P_1}{\partial \theta}, \tag{B.10}$$

$$\frac{\partial U_1}{\partial r} + \frac{U_1}{r} + \frac{1}{r}\frac{\partial V_1}{\partial \theta} = 0 \tag{B.11}$$

for $r < 1 + \gamma F_1$, and

$$\frac{\partial^2 \Phi_1}{\partial r^2} + \frac{1}{r}\frac{\partial \Phi_1}{\partial r} + \frac{1}{r^2}\frac{\partial^2 \Phi_1}{\partial \theta^2} = 0 \tag{B.12}$$

for $r > 1 + \gamma F_1$. The matching condition from (4.10)–(4.11), linearised on $r = 1$, is

$$U_1 - \frac{\mathrm{d}F_1}{\mathrm{d}\theta} = 0, \tag{B.13}$$

$$\frac{\partial \Phi_1}{\partial r} - \frac{\mathrm{d}F_1}{\mathrm{d}\theta} = 0, \tag{B.14}$$

$$\frac{\rho_2}{\rho_1}P_1 + \frac{\partial \Phi_1}{\partial \theta} + F_1\left(\frac{\rho_2}{\rho_1} - 1\right) = -S\left(F_1 + \frac{\partial^2 F_1}{\partial \theta^2}\right). \tag{B.15}$$

The solution is given in (5.9) to (5.10) and (5.11).

B.2 The solution for Kelvin waves

Solutions to (4.23)–(4.27) with the basic state given by (4.13) and (4.14), independent of s with wavenumber m in θ and k_0 in s, are known as Kelvin waves. They take the form

$$\begin{aligned}
p_0^{(m)} &= J_m(\eta_1 r)\beta_0^{(m)}, \\
u_0^{(m)} &= \frac{\mathrm{i}}{\omega_0 - m + 2}\left[-\frac{m}{r}J_m(\eta_1 r) + \frac{\omega_0 - m}{\omega_0 - m - 2}\eta_1 J_{m+1}(\eta_1 r)\right]\beta_0^{(m)}, \\
v_0^{(m)} &= \frac{1}{\omega_0 - m + 2}\left[\frac{m}{r}J_m(\eta_1 r) + \frac{2}{\omega_0 - m - 2}\eta_1 J_{m+1}(\eta_1 r)\right]\beta_0^{(m)}, \\
w_0^{(m)} &= \frac{k_0}{\omega_0 - m}J_m(\eta_1 r)\beta_0^{(m)}
\end{aligned} \tag{B.16}$$

for $r < 1 + \tilde{f}_0$. The radial wavenumber is

$$\eta_1^2 = \left[\frac{4}{(\omega_0 - m)^2} - 1\right]k_0^2. \tag{B.17}$$

For $r > 1 + \tilde{f}_0$,

$$\phi_0^{(m)} = K_m(k_0 r)\alpha_0^{(m)}. \tag{B.18}$$

α_0, β_0 are the amplitudes of Kelvin waves. The $m+1$ waves for curvature instability and the $m+2$ waves for MSTW instability are obtained by replacing m in the formulas by $m+1$ and $m+2$. Recurrence relations are used to reduce the order of the Bessel functions.

The kinematic boundary condition (4.28) leads to

$$f_0^{(m)} = \frac{\mathrm{i}}{(\omega_0 - m)} u_0^{(m)}. \tag{B.19}$$

The dispersion relation is obtained by enforcing the dynamic boundary condition, which includes both surface tension and the density ratio.

B.3 Calculation for parametric instability

B.3.1 Boundary conditions for the curvature instability

Substituting the $O(\delta\epsilon)$ solutions for modes m and $m+1$ into (4.36) and (4.37) gives

$$u_1^{(m)} = \left.\frac{\mathrm{d}\phi_1}{\mathrm{d}r}\right^{(m)}, \tag{B.20}$$

$$\begin{aligned}\frac{\rho_2}{\rho_1} p_1^{(m)} - \mathrm{i}(\omega_0 - m)\phi_1^{(m)} = {} & \mathrm{i}\omega_1 \phi_0^{(m)} + \frac{m+1}{8}\left(\frac{\rho_2}{\rho_1} + 4S\right)\phi_0^{(m+1)} \\ & + \left[1 - \frac{\rho_2}{\rho_1} + S(k_0^2 + m^2)\right] f_1^{(m)} \\ & + 2Sk_0k_1 f_0^{(m)} - S\left(\frac{m+1}{2} + k_0^2 - 1\right)\mathrm{i} f_0^{(m+1)}\end{aligned} \tag{B.21}$$

and

$$u_1^{(m+1)} = \left.\frac{\mathrm{d}\phi_1}{\mathrm{d}r}\right^{(m+1)}, \tag{B.22}$$

$$\begin{aligned}\frac{\rho_2}{\rho_1} p_1^{(m+1)} - \mathrm{i}(\omega_0 - m - 1)\phi_1^{(m+1)} = {} & \mathrm{i}\omega_1 \phi_0^{(m+1)} - \frac{m}{8}\left(\frac{\rho_2}{\rho_1} + 4S\right)\phi_0^{(m)} \\ & + \left[1 - \frac{\rho_2}{\rho_1} + S(k_0^2 + (m+1)^2)\right] f_1^{(m+1)} \\ & + 2Sk_0k_1 f_0^{(m+1)} - S\left(\frac{m}{2} - k_0^2 + 1\right)\mathrm{i} f_0^{(m)}\end{aligned} \tag{B.23}$$

respectively. The $O(\delta\epsilon)$ boundary disturbance f_1 for the two modes is obtained from (4.35) as

$$f_1^{(m)} = \frac{1}{\mathrm{i}(\omega_0 - m)}\left[-u_1^{(m)} - \mathrm{i}\omega_1 f_0^{(m)} - \frac{m+1}{8} f_0^{(m+1)} - \frac{5}{8} f_0^{(m+1)}\right], \tag{B.24}$$

$$f_1^{(m+1)} = \frac{1}{\mathrm{i}(\omega_0 - m - 1)}\left[-u_1^{(m+1)} - \mathrm{i}\omega_1 f_0^{(m+1)} + \frac{m}{8} f_0^{(m)} - \frac{5}{8} f_0^{(m)}\right]. \tag{B.25}$$

B.3.2 Boundary conditions for the MSTW instability

Writing the boundary conditions (5.32) and (5.33) for the $O(\delta\gamma)$ solutions gives

$$\begin{aligned} u_1^{(m)} - \frac{\mathrm{d}\phi_1}{\mathrm{d}r}^{(m)} =& -\frac{m+2}{2}\phi_0^{(m+2)} - \frac{\mathrm{i}}{2} v_0^{(m+2)} + \frac{1}{4}\left[\frac{\mathrm{d}^2\phi_0}{\mathrm{d}r^2}^{(m+2)} - \frac{\mathrm{d}u_0}{\mathrm{d}r}^{(m+2)}\right] \\ &+ \frac{\mathrm{i}}{2}\left(1 - \frac{\rho_2}{\rho_1} + 3S\right) f_0^{(m+2)} - \frac{\mathrm{i}(m+2)}{4}\left(1 - \frac{\rho_2}{\rho_1} + 3S\right) f_0^{(m+2)}, \end{aligned} \tag{B.26}$$

$$\begin{aligned} \frac{\rho_2}{\rho_1} p_1^{(m)} - \mathrm{i}(\omega_0 - m)\phi_1^{(m)} =& \mathrm{i}\omega_1\phi_0^{(m)} - \frac{1}{4}\left[\frac{\rho_2}{\rho_1}\frac{\mathrm{d}p_0}{\mathrm{d}r}^{(m+2)} - \mathrm{i}(\omega_0 - m)\frac{\mathrm{d}\phi_0}{\mathrm{d}r}^{(m+2)}\right] \\ &- \frac{\mathrm{i}(m+2)}{4}\left(-1 - \frac{\rho_2}{\rho_1} + 3S\right)\phi_0^{(m+2)} \\ &+ \frac{3}{4}\left(1 - \frac{\rho_2}{\rho_1} + 2S\right) f_0^{(m+2)} + \left[1 - \frac{\rho_2}{\rho_1} + S(m^2 + k_0^2)\right] f_1^{(m)} \\ &+ S\left[2k_0 k_1 f_0^{(m)} - \frac{(m+2)^2}{2} f_0^{(m+2)}\right] \end{aligned} \tag{B.27}$$

for wave m, and

$$\begin{aligned} u_1^{(m+2)} - \frac{\mathrm{d}\phi_1}{\mathrm{d}r}^{(m+2)} =& \frac{m}{2}\phi_0^{(m)} + \frac{\mathrm{i}}{2} v_0^{(m)} + \frac{1}{4}\left[\frac{\mathrm{d}^2\phi_0}{\mathrm{d}r^2}^{(m)} - \frac{\mathrm{d}u_0}{\mathrm{d}r}^{(m)}\right] \\ &- \frac{\mathrm{i}}{2}\left(1 - \frac{\rho_2}{\rho_1} + 3S\right) f_0^{(m)} - \frac{\mathrm{i}m}{4}\left(1 - \frac{\rho_2}{\rho_1} + 3S\right) f_0^{(m)}, \end{aligned} \tag{B.28}$$

$$\frac{\rho_2}{\rho_1}p_1^{(m+2)} - \mathrm{i}(\omega_0 - m - 2)\phi_1^{(m+2)} = \mathrm{i}\omega_1\phi_0^{(m+2)} - \frac{1}{4}\left[\frac{\rho_2}{\rho_1}\frac{\mathrm{d}p_0}{\mathrm{d}r}^{(m)} - \mathrm{i}(\omega_0 - m - 2)\frac{\mathrm{d}\phi_0}{\mathrm{d}r}^{(m)}\right] - \frac{\mathrm{i}m}{4}\left(-1 - \frac{\rho_2}{\rho_1} + 3S\right)\phi_0^{(m)} + \frac{3}{4}\left(1 - \frac{\rho_2}{\rho_1} + 2S\right) \times f_0^{(m)} + \left\{1 - \frac{\rho_2}{\rho_1} + S[(m+2)^2 + k_0^2]\right\} f_1^{(m+2)} + S\left[2k_0k_1f_0^{(m+2)} - \frac{m^2}{2}f_0^{(m)}\right]. \tag{B.29}$$

for wave $m+2$ (cf. (4.8) and (4.9) in Fukumoto, 2003, for $\rho_2/\rho_1 = 1$, $S = 0$). Unlike the case of Tsai & Widnall (1976) and Fukumoto (2003), f_1 needs to be obtained from the above equations in order to calculate the dispersion relation. Using (5.31), we have

$$f_1^{(m)} = \frac{-1}{\mathrm{i}(\omega_0 - m)}\left[u_1^{(m)} + \mathrm{i}\omega_1 f_0^{(m)} + \frac{\mathrm{i}}{2}v_0^{(m+2)} + \frac{\mathrm{i}(m+1)}{2}f_0^{(m+2)} + \frac{1}{4}\frac{\mathrm{d}u_0}{\mathrm{d}r}^{(m+2)}\right], \tag{B.30}$$

$$f_1^{(m+2)} = \frac{-1}{\mathrm{i}(\omega_0 - m - 2)}\left[u_1^{(m+2)} + \mathrm{i}\omega_1 f_0^{(m+2)} - \frac{\mathrm{i}}{2}v_0^{(m)} + \frac{\mathrm{i}(m+1)}{2}f_0^{(m)} + \frac{1}{4}\frac{\mathrm{d}u_0}{\mathrm{d}r}^{(m)}\right]. \tag{B.31}$$

B.3.3 Solvability conditions and dispersion relation

The dispersion relation relating k_1 and ω_1 for disturbances at $O(\delta\epsilon)$ or $O(\delta\gamma)$ is determined as follows. The disturbance satisfies (4.30)–(4.34) or (5.26)–(5.30) with undetermined coefficients α_1, β_1 in the solution, which need to be determined using the boundary conditions at the same order. The boundary conditions for the first mode for m (represented by a superscript '(1)') lead to an inhomogeneous linear system of the form

$$\begin{bmatrix} M_{11} & M_{12} \\ M_{21} & M_{22} \end{bmatrix}\begin{bmatrix} \alpha_1^{(1)} \\ \beta_1^{(1)} \end{bmatrix} = \begin{bmatrix} F_1 \\ F_2 \end{bmatrix}, \tag{B.32}$$

while the second mode for $m+1$ or $m+2$ (represented by a superscript '(2)') become

$$\begin{bmatrix} N_{11} & N_{12} \\ N_{21} & N_{22} \end{bmatrix} \begin{bmatrix} \alpha_1^{(2)} \\ \beta_1^{(2)} \end{bmatrix} = \begin{bmatrix} G_1 \\ G_2 \end{bmatrix}. \tag{B.33}$$

The vectors $\boldsymbol{F}$ and $\boldsymbol{G}$ consist of the solution for Kelvin waves which has undetermined coefficients α_0 and β_0. They also depend on known quantities, m, k_0, ω_0, ρ_2/ρ_1, S, and on the unknowns k_1 and ω_1.

The matrices $\mathbf{M}$ and $\mathbf{N}$ on the left-hand side of (B.32) and (B.33) depend on m, ω_0, k_0, ρ_2/ρ_1, S. The two linear systems are singular, i.e. their determinants are zero. The solvability condition requires that the vectors $\boldsymbol{F}$ and $\boldsymbol{G}$ lie in the image space of $\mathbf{M}$ and $\mathbf{N}$, i.e.

$$\begin{cases} M_{11}F_2 - M_{21}F_1 = 0, \\ N_{11}G_2 - N_{21}G_1 = 0. \end{cases} \tag{B.34}$$

Using the relations

$$\alpha_0^{(1)} = -\frac{\mathrm{i}J_m(\eta_1)}{(\omega_0 - m)K_m(k_0)}\beta_0^{(1)}, \quad \alpha_0^{(2)} = -\frac{\mathrm{i}J_{m+1}(\eta_2)}{(\omega_0 - m - 1)K_{m+1}(k_0)}\beta_0^{(2)} \tag{B.35}$$

to replace $\alpha_0^{(1)}$ and $\alpha_0^{(2)}$, (B.34) can be converted to a homogeneous linear system

$$\begin{bmatrix} D_{11} & D_{12} \\ D_{21} & D_{22} \end{bmatrix} \begin{bmatrix} \beta_0^{(1)} \\ \beta_0^{(2)} \end{bmatrix} = \mathbf{0}. \tag{B.36}$$

For nontrivial $\beta_0^{(1)}$ and $\beta_0^{(2)}$, the resulting determinant equation

$$D_{11}D_{22} - D_{12}D_{21} = 0 \tag{B.37}$$

leads to the dispersion relation for (k_1, ω_1). This is a quadratic equation for ω_1, where ω_1

is obtained from D_{11} and D_{22} as

$$D_{11} = \mu_1\omega_1 + \mu_2, \qquad D_{22} = \mu_3\omega_1 + \mu_4. \tag{B.38}$$

The dispersion relation is hence

$$\mu_1\mu_3\ \omega_1^2 + (\mu_1\mu_4 + \mu_2\mu_3)\ \omega_1 + \mu_2\mu_4 - D_{12}D_{21} = 0; \tag{B.39}$$

Expressions for μ_i and D_{12}, D_{21} are obtained using a symbolic algebra computer code.

These quantities are functions of k_1 with m, ω_0, k_0, ρ_2/ρ_1 and S all given. The growth rate $\sigma_1 = |\mathrm{Im}(\omega_1)|$ has a maximum when $k_1 = 0$ where $\mu_2 = \mu_4 = 0$, giving

$$\sigma_{1max} = \sqrt{-\frac{D_{12}D_{21}}{\mu_1\mu_3}}. \tag{B.40}$$

One half of the unstable bandwidth Δk_1 is calculated by finding the root k_1 of

$$(\mu_1\mu_4 + \mu_2\mu_3)^2 - 4\mu_1\mu_3(\mu_2\mu_4 - D_{12}D_{21}) = 0. \tag{B.41}$$

References

Baker, G.R., Meiron, D.I. & Orszag, S.A. 1980 Vortex simulations of the Rayleigh–Taylor instability. *Phys. Fluids* **23**, 1485–1490.

Baker, G. R., Caflisch, R. & Siegel, M. 1993 Singularity formation during Rayleigh–Taylor instability. *J. Fluid Mech.* **252**, 51–78.

Baker, G. R., Meiron, D. I. & Orszag, S. A. 1982 Generalized vortex methods for free-surface flow problems. *J. Fluid Mech.* **123**, 477–501.

Baker, G. R. & Moore, D. W. 1989 The rise and distortion of a two-dimensional gas bubble in an inviscid liquid. *Phys. Fluids* A **1**, 1451–1459.

Baker, G. R. & Nachbin, A. 1998 Stable methods for vortex sheet motion in the presence of surface tension. *SIAM J. Sci. Comput.* **19**, 1737–1766.

Baker, G. R. & Xie, C. 2011 Singularities in the complex physical plane for deep water waves. *J. Fluid Mech.* **685**, 83–116.

Baumann, N., Joseph, D. D. & Mohr, P. 1992 Vortex rings of one fluid in another in free fall. *Phys. Fluids* A **4**, 567–580.

Bayly, B. J. 1986 Three-dimensional instability of elliptical flow. *Phys. Rev. Lett.* **57**, 2160–2163.

Blanco-Rodriguez, F. J. & Le Dizès, S. 2016 Elliptic instability of a curved Batchelor vortex. *J. Fluid Mech.* **804**, 224–247.

Blanco-Rodriguez, F. J. & Le Dizès, S. 2017 Curvature instability of a curved Batchelor vortex. *J. Fluid Mech.* **814**, 397–415.

Blyth, M., Rodriguez-Rodriguez, J. & Salman, H. 2014 Buoyant Norbury's vortex rings. In *Bulletin of the American Physical Society*, *Div. Fluid Dyn.*, vol. 59.

Boyd, John P. 2001 *Chebyshev and Fourier Spectral Methods*. Dover Publications.

Cairns, R. A. 1979 The role of negative energy waves in some instabilities of parallel flows. *J. Fluid Mech.* **92**, 1–14.

Callegari, A. J. & Ting, L. 1978 Motion of a curved vortex filament with decaying vortical core and axial velocity. *SIAM J. Appl. Math.* **35**, 148–174.

Chang, C. & Llewellyn Smith, S. G. 2018 The motion of a buoyant vortex filament. *J. Fluid Mech.* **857**, R1.

Chang, C. & Llewellyn Smith, S. G. 2020 Axisymmetric contour dynamics for buoyant vortex rings. *J. Fluid Mech.* **887**, A28.

Chen, L., Garimella, S. V., Reizes, J. A. & Leonardi, E. 1999 The development of a bubble rising in a viscous liquid. *J. Fluid Mech.* **387**, 61–96.

Cheng, M., Lou, J. & Lim, T. T. 2013 Motion of a bubble ring in a viscous fluid. *Phys. Fluids* **25**, 067104.

Cowley, S. J., Baker, G. R. & Tanveer, S. 1999 On the formation of Moore curvature singularities in vortex sheets. *J. Fluid Mech.* **378**, 233–267.

Crow, S. C. 1970 Stability theory for a pair of trailing vortices. *AIAA J.* **8**, 2172–2179.

Dritschel, D. G. 1989 Contour dynamics and contour surgery: Numerical algorithms for extended, high-resolution modelling of vortex dynamics in two-dimensional, inviscid, incompressible flows. *Comput. Phys. Rep.* **10**, 77–146.

Eldredge, J. D. & Jones, A. R. 2019 Leading-edge vortices: mechanics and modeling. *Annu. Rev. Fluid Mech.* **51**, 75–104.

Eloy, C. & Le Dizès, S. 2001 Stability of the Rankine vortex in a multipolar strain field. *Phys. Fluids* **13**, 660–676.

Fraenkel, L. E. 1972 Examples of steady vortex rings of small cross-section in an ideal fluid. *J. Fluid Mech.* **51**, 119–135.

Fukumoto, Y. 2003 The three-dimensional instability of a strained vortex tube revisited. *J. Fluid Mech.* **493**, 287–318.

Fukumoto, Y. & Hattori, Y. 2005 Curvature instability of a vortex ring. *J. Fluid Mech.* **526**, 77–115.

Hattori, Y., Blanco-Rodriguez, F. J. & Dizès, S. Le 2019 Numerical stability analysis of a vortex ring with swirl. *J. Fluid Mech.* **878**, 5–36.

Hattori, Y. & Fukumoto, Y. 2003 Short-wavelength stability analysis of thin vortex rings. *Phys. Fluids* **15**, 3151–3163.

Hattori, Y. & Moffatt, H. K. 2006 Evolution of toroidal magnetic eddies in an ideal fluid. *J. Fluid Mech.* **558**, 253–279.

Hicks, W. M. 1884 On the steady motion and small vibrations of a hollow vortex. *Phil. Trans. R. Soc. Lond.* A **175**, 161–195.

Hou, T. Y., Lowengrub, J. S. & Shelley, M. J. 1994 Removing the stiffness from interfacial flows with surface tension. *J. Comput. Phys.* **114**, 312–338.

Iserles, A. 2009 *A First Course in the Numerical Analysis of Differential Equations*. Cambridge University Press.

Joly, L., Fontane, J. & Chassaing, P. 2005 The Rayleigh–Taylor instability of two-dimensional high-density vortices. *J. Fluid Mech.* **537**, 415–432.

Kida, Shigeo 1981 A vortex filament moving without change of form. *J. Fluid Mech.* **112**, 397–409.

Krasny, R. 1986*a* Desingularization of periodic vortex sheet roll-up. *J. Comput. Phys.* **65**, 292–313.

Krasny, R. 1986*b* A study of singularity formation in a vortex sheet by the point-vortex approximation. *J. Fluid Mech.* **167**, 65–93.

Krein, M. G. 1950 A generalization of several investigations of A. M. Liapunov on linear differential equations with periodic coefficients. *Dokl. Akad. Nauk. SSSR* **73**, 445–448.

Leonard, A. 2010 On the motion of thin vortex tube. *Theor. Comput. Fluid Dyn.* **24**, 369–375.

Leweke, T. & Williamson, C. H. K. 1998 Cooperative elliptic instability of a vortex pair. *J. Fluid Mech.* **360**, 85–119.

Llewellyn Smith, S. G., Chang, C., Chu, T., Blyth, M., Hattori, Y. & Salman, H. 2018 Generalized contour dynamics: A review. *Reg. Chaotic Dyn.* **23**, 507–518.

Llewellyn Smith, S. G. & Hattori, Y. 2012 Axisymmetric magnetic vortices with swirl. *Commun. Nonlinear Sci. Numer. Simulat.* **17**, 2101–2107.

Lundgren, T. S. & Mansour, N. N. 1991 Vortex ring bubbles. *J. Fluid Mech.* **224**, 177–196.

MacKay, R. S. 1986 Stability of equilibria of Hamiltonian systems. In *Nonlinear Phenomena and Chaos* (ed. S. Sarkar), pp. 254–270. Adam Hilger.

Marten, K., Shariff, K., Psarakos, S. & White, D. J. 1996 Ring bubbles of dolphins. *Sci. Am.* **275**, 82–87.

Maxworthy, T. 1972 The structure and stability of vortex rings. *J. Fluid Mech.* **51**, 15–32.

Maxworthy, T. 1977 Some experimental studies of vortex rings. *J. Fluid Mech.* **81**, 465–495.

Meiron, D. I., Baker, G. R. & Orszag, S. A. 1982 Analytic structure of vortex sheet dynamics. Part 1. Kelvin–Helmholtz instability. *J. Fluid Mech.* **114**, 283–298.

Moore, D.W. & Saffman, P.G. 1971 Structure of a line vortex in an imposed strain. In *Aircraft Wake Turbulence and its Detection* (ed. J. H. Olsen, A. Goldburg & M. Rogers), pp. 339–354. Plenum.

Moore, D. W. 1972 Finite amplitude waves on aircraft trailing vortices. *Aero. Quarterly* **23**, 307–314.

Moore, D. W. 1979 The spontaneous appearance of a singularity in the shape of an evolving vortex sheet. *Proc. R. Soc. Lond.* A **365**, 105–119.

Moore, D. W. & Saffman, P. G. 1972 The motion of a vortex filament with axial flow. *Phil. Trans. R. Soc. Lond.* A **272**, 403–429.

Moore, D. W. & Saffman, P. G. 1975 The instability of a straight vortex filament in a strain field. *Proc. R. Soc. Lond.* A **346**, 413–425.

Nitsche, M. 2001 Singularity formation in a cylindrical and a spherical vortex sheet. *J. Comout. Phys.* **173**, 208–230.

Nitsche, M. & Krasny, R. 1994 A numerical study of vortex ring formation at the edge of a circular tube. *J. Fluid Mech.* **276**, 139–161.

Norbury, J. 1972 A steady vortex ring close to Hill's spherical vortex. *Proc. Camb. Phil. Soc.* **72**, 253–284.

Norbury, J. 1973 A family of steady vortex rings. *J. Fluid Mech.* **57**, 417–431.

Oberti, C. & Ricca, R. L. 2019 Influence of winding number on vortex knots dynamics. *Sci. Rep.* **9**, 17284.

Pedley, T. J. 1968 The toroidal bubble. *J. Fluid Mech.* **32**, 97–112.

Pope, S. B. 2000 *Turbulent Flows*. Cambridge University Press.

Pozrikidis, C. 1986 The nonlinear instability of Hill's vortex. *J. Fluid Mech.* **168**, 337–367.

Pullin, D. I. 1982 Numerical studies of surface-tension effects in nonlinear Kelvin–Helmholtz and Rayleigh–Taylor instability. *J. Fluid Mech.* **119**, 507–532.

Pullin, D. I. 1992 Contour dynamics methods. *Annu. Rev. Fluid Mech.* **24**, 89–115.

Pullin, D. I. & Saffman, P. G. 1998 Vortex dynamics in turbulence. *Annu. Rev. Fluid Mech.* **30**, 31–51.

Riley, N. 1998 The fascination of vortex rings. *Appl. Sci. Res.* **59**, 169–189.

Rosenhead, L. 1930 The spread of vorticity in the wake behind a cylinder. *Proc. Roy. Soc.* A **127**, 590–612.

Saffman, P. G. 1978 The number of waves on unstable vortex rings. *J. Fluid Mech.* **84**, 625–639.

Saffman, P. G. 1992 *Vortex Dynamics*. Cambridge University Press.

Schwarz, K. W. 1985 Three-dimensional vortex dynamics in superfluid He: Line-line and line-boundary interactions. *Phys. Rev.* B **31**, 5782–5804.

Shariff, K. & Leonard, A. 1992 Vortex rings. *Annu. Rev. Fluid Mech.* **24**, 235–279.

Shariff, K., Leonard, A. & Ferziger, J. 1989 Dynamics of a class of vortex rings. *Tech. Rep.* 102257. NASA.

Shariff, K., Leonard, A. & Ferziger, J. 2008 A contour dynamics algorithm for axisymmetric flow. *J. Comput. Phys.* **227**, 9044–9062.

Shin, S., Sohn, S.-I. & Hwang, W. 2014 Simple and efficient numerical methods for vortex sheet motion with surface tension. *Int. J. Numer. Meth. Fl.* **74**, 422–438.

Shin, S., Sohn, S.-I. & Hwang, W. 2018 Vortex simulations of the Kelvin–Helmholtz instability with surface tension in density-stratified flows. *Eur. J. Mech.* B *Fluids* **67**, 168–177.

Sohn, S.-I. 2015 Stability and capillary dynamics of circular vortex sheets. *Theor. Comput. Fluid Dyn.* **29**, 291–310.

Sohn, S.-I. & Hwang, W. 2005 Numerical simulations of vortex sheet evolution in stratified shear flow. *J. Phys. Soc. Jpn.* **74**, 1472–1478.

Stock, M. J., Dahm, W. J. A. & Tryggvason, G. 2008 Impact of a vortex ring on a density interface using a regularized inviscid vortex sheet method. *J. Comput. Phys.* **227**, 9021–9043.

Tait, P. G. 1867 On the integrals of the hydrodynamical equations, which express vortex-motion. *Phil. Mag.* **33**, 485–512, a translation of von Helmholtz (1858).

Thomson, W. (Lord Kelvin) 1867*a* On vortex atoms. *Proc. Roy. Soc. Edin.* **6**, 94–105.

Thomson, W. (Lord Kelvin) 1867*b* The translatory velocity of a circular vortex ring. *Phil. Mag.* **33**, 511–512.

Thomson, W. (Lord Kelvin) 1869 On vortex motion. *Trans. Roy. Soc. Edin.* **25**, 217–260.

Thomson, W. (Lord Kelvin) 1875 Vortex statics. *Proc. R. Soc. Edinburgh* **9**, 59–73.

Trefethen, L. N. & Weideman, J. A. C. 2014 The exponentially convergent trapezoidal rule. *SIAM Review* **56**, 385–458.

Tryggvason, G. 1988 Numerical simulations of the Rayleigh–Taylor instability. *J. Comput. Phys.* **75**, 253–282.

Tsai, C. Y. & Widnall, S. E. 1976 The stability of short waves on a straight vortex filament in a weak externally imposed strain field. *J. Fluid Mech.* **73**, 721–733.

Turner, J. S. 1957 Buoyant vortex rings. *Proc. R. Soc. Lond* A **239**, 61–75.

Turner, J. S. 1973 *Buoyancy effects in fluids*. Cambridge University Press.

Vasel-Be-Hagh, A. R., Carriveau, R. & Ting, D. S.-K. 2015*a* A ballon bursting underwater. *J. Fluid Mech.* **769**, 522–540.

Vasel-Be-Hagh, A. R., Carriveau, R., Ting, D. S.-K. & Turner, J. S. 2015*b* Drag of buoyant vortex rings. *Phys. Rev.* A **92**, 043024.

Velasco Fuentes, O. 2014 Early observations and experiments on ring vortices. *Eur. J. Mech.* B *Fluids* **43**, 166–171.

von Helmholtz, H. 1858 ´Uber Integrale der hydrodynamischen Gleichungen, welche der Wirbelbewegung entsprechen. *J.´ fur die reine und angewandte Mathematik* **55**, 25–55.

Waleffe, F. 1990 On the three-dimensional instability of strained vortices. *Phys. Fluids* A **2**, 76–80.

Widnall, S. E. 1972 The stability of a helical vortex filament. *J. Fluid Mech.* **54**, 641–663.

Widnall, S. E. & Bliss, D. B. 1971 Slender-body analysis of the motion and stability of a vortex filament containing an axial flow. *J. Fluid Mech.* **50**, 335–353.

Widnall, S. E., Bliss, D. B. & Tsai, C. Y. 1974 The instability of short waves on a vortex ring. *J. Fluid Mech.* **66**, 35–47.

Widnall, S. E. & Sullivan, J. P. 1973 On the instability of thin vortex rings. *Proc. R. Soc. Lond.* A **332**, 335–353.

Widnall, S. E. & Tsai, C. Y. 1977 The instability of the thin vortex ring of constant vorticity. *Phil. Trans. R. Soc. Lond.* A **287**, 273–305.

Winckelmans, G., Cocle, R., Dufresne, L. & Capart, R. 2005 Vortex methods and their application to trailing wake vortex simulations. *C. R. Physique* **6**, 467–486.

Winckelmans, G. S. 2004 Vortex methods. In *Encyclopedia of Computational Mechanics* (ed. E. Stein, R. Borst & T. J. R. Hughes), pp. 129–153. Wiley.

Yatsuyanagi, Y., Hattori, T. & Kato, T. 1996 The equations of motion of vortex-current filaments. *J. Phys. Soc. Jpn.* **65**, 745–759.

Zabusky, N. J., Hughes, M. H. & Roberts, K. V. 1979 Contour dynamics for the euler equations in two dimensions. *J. Comput. Phys.* **30**, 96–106.